IN THE UNITED STATES PATENT AND TRADEMARK OFFICE

In re application of: Ronald D. BLUM, ET AL.	Confirmation No. 9812
	Examiner: Boeckmann, Jason
Application No.: 09/994,860	Technology Center/Art Unit: 3752
Filed: November 28, 2001	
For: METHOD AND APPARATUS FOR REDUCING THE INTENSITY OF HURRICANES AT SEA BY DEEP-WATER UPWELLING	
Customer No.: 20350	

Mail Stop AF
Commissioner for Patents
P.O. Box 1450
Alexandria, VA 22313-1450

DECLARATION UNDER 37 C.F.R. § 1.132

I, Vickie Lien Singleton, declare the following:

1.   I hold a Bachelor of Science degree in Mechanical Engineering from West Virginia University, a Master of Science in Civil Engineering, specializing in airlift aerator modelling, from Virginia Polytechnic Institute and State University, and am currently a fourth year Ph.D. candidate at Virginia Polytechnic Institute and State University studying bubble plume dynamics and water quality modelling. A copy of my resume is attached as Exhibit A.

2.   I have read and am familiar with the above-referenced application. I have also read and am familiar with the Office Action mailed May 4, 2007 ("Office Action") pertaining to this application.

3. I have been retained by the assignee of the above-identified application to assist in responding to the Office Action. I have no financial interest in the assignee or the outcome of this patent application, including whether it issues as a patent or not. I am being compensated for the time spent on this matter at the rate of $200/hr, plus reasonable expenses.

4. It is my understanding that the claims currently under examination, which relate to, inter alia, methodologies for reducing the intensity of a hurricane, were rejected as allegedly being wholly inoperative, lacking credible utility, and not enabled. Specifically, the Examiner asserts:

> ...applicant admits in his arguments, "submersibles of the kind required for this application do not presently exist." It seems that applicant wishes that someone will come along and develop the technology required to make the required submersibles, thereby enabling the present invention. Therefore, it is impossible for one of ordinary skill in the art at his time to make and or use this invention. Office Action at page 6.

5. This Declaration provides support for an initial order-of-magnitude estimate of the gas flow rate and the quantity of gas required to induce an adequate upwelling flow rate to lower the temperature of the upper sea surface, using the amount of direction provided for in the specification in combination with the knowledge of one skilled in the art at the time of filing the application, such as the use of two existing bubble-plume models, without any undue or unreasonable experimentation. In particular, the specification is replete with the detailed description of various gas sources (see, e.g., para 0029), submersible designs (see, e.g., para 0034), inception strategies (see, e.g., 0026-27, 49-64), and the exemplary calculation for upwelling volume required for successful surface layer water cooling (see, e.g., 0049-64).

6. The specification is directed to reducing the intensity of hurricanes at sea by upwelling deep-water in the ocean. To obtain an initial order-of-magnitude estimate of the gas flow rate required to induce an adequate upwelling flow rate, two existing bubble-plume models were

applied. Each model is based on the discrete-bubble method developed by Wüest, A. ET AL., WATER RESOUR. RES. 1992, 28, 3235-3250, and accounts for ambient density stratification and mass transfer between bubbles and water. The circular bubble-plume model was published in 1992 and is for a circular or round gas diffuser. The linear bubble-plume model was first presented in 2001 (McGinnis, D. ET AL., Asian Waterqual 2001: First IWA Asia-Pacific Regional Conference: Fukuoka, Japan, 12-15 Sept. 2001) and was later refined and validated in 2007 (Singleton, V. ET AL., WATER RESOUR. RES. 2007, 43, W02405). This model is for a long and narrow diffuser. Both diffuser configurations were modeled to compare the effects of geometry on upwelled or induced water flow rate. Based on the design example in the patent application, it was assumed that the diffusers would be located at about 300 m depth when bubbling. The patent application states that carbon dioxide is the preferred gas, so model calculations focus on this compound. Because they are used for lake oxygenation studies, the solubility (Weiss, R. ET AL., Mar. Chem. 1974, 2, 203-215) and mass transfer coefficients (Clift, R., ET AL., BUBBLE, DROPS, AND PARTICLES New York, NY, 1978) of the bubble-plume models were modified for carbon dioxide, and the effect of dissolved carbon dioxide on water density was included (Weiss ET AL, *supra*). The Wüest reference is attached as Exhibit B, the McGinnis reference is attached as Exhibit C, the Singleton reference is attached as Exhibit D, the Weiss reference is attached as Exhibit E, and the Clift reference is attached as Exhibit F.
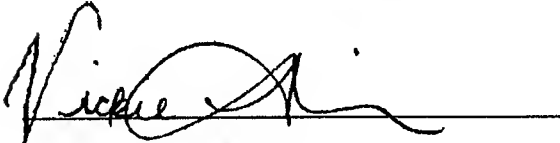
7.   To apply the models, boundary condition profiles of temperature and salinity are needed. In an attempt to closely represent the design example of the application, profile data collected off the eastern coast of Florida (26.17N,-78.80W) on September 19, 2007 were used (www.aoml.noaa.gov/phod/triananes/tmp/dxbt1190840242.dat). The depth of the 26° C isotherm in this recent profile is approximately 81 m, which is slightly more conservative than the 70 m depth of the patent application design example. The models also require the dimensions of the diffusers and the initial bubble size. The initial bubble size was assumed to be 10 mm. As a starting point, the length of the linear diffuser was assumed to be proportional to the length of an SSBN-726 Ohio-Class submarine, which is about 170 m. Using a linear diffuser

length and width of 150 m and 13 m, respectively, produces a diffuser area of 1,950 m^2. An equivalent diameter for the circular diffuser for this cross-sectional area is approximately 50 m.

8.   Using these initial and boundary conditions, each model was run over a range of applied gas flow rates (2,000–20,000 Nm^3/s) to a single diffuser system or unit. Because the intent of the apparatus is to cool surface waters, the lowest gas flow rate that upwelled water to and detrained at the surface was selected. The gas flow rates that induced plumes to the surface were 10,500 and 12,500 Nm^3/s for the linear and circular diffusers, respectively. The depth of the 26°C isotherm, the temperature below which hurricane development is hampered, was 81 m. Therefore, only plume induced flow rates from 300 to 81 m depth are considered as effective upwelling flow rates. For the previously stated gas flow rates, the plume water flow rates at the depth of 26°C isotherm are 51,900 and 51,300 m^3/s for a single linear and circular diffuser, respectively. These flow rates represent the upwelling flow rate from deeper water into the effective epilimnion or surface layer. Even though the plume continues to rise through the epilimnion and entrain ambient water, plume induced flow that occurs within the effective epilimnion does not contribute to the upwelling into this volume. It would be expected that the artificial upwelling of the deep, cold seawater to the sea surface layer by the bubble-driven plume would create an upper ocean layer region of sufficiently lower temperature.

9.   Referring to the patent application, the maneuver before upwelling submersible mobilization strategy is estimated to require a total upwelled water flow rate of at least 12.1 million m^3/s. Using the estimated water flow rate values of 51,900 and 51,300 m^3/s for a single linear and circular diffuser unit, respectively, a total of 233 linear or 236 circular diffusers may be needed. This corresponds to total gas flow rates of 2.45 and 2.95 million Nm^3/s for the linear and circular diffusers, respectively. Per the patent application, the maneuver before upwelling strategy requires a total gas volume of 5.29 x 10^{10} Nm^3 for the linear diffusers and 6.37 x 10^{10} Nm^3 for the circular diffusers. Assuming that 476 Nm^3 of gas would be liberated per cubic meter of liquid, the amount of liquid CO_2 required for linear diffusers would be about 1 x 10^8 m^3 and about 1.3 x 10^8 m^3 for circular diffusers.

10.　　All statements made herein of my own knowledge are true and that all statements made on information and belief are believed to be true; and further, that the statements were made with the knowledge that willful false statements and the like so made are punishable by fine or imprisonment, or both, under section 1001 of Title 18 of the United States Code, and such willful false statements may jeopardize the validity of the application or any patents issuing thereon.

Vickie Lien Singleton

Date 11-1-07

Exhibit A

10. Education and Experience:

January 2003 to Present
- Enrolled in Ph.D. program at Virginia Polytechnic Institute and State University
- Current GPA: 4.0

June 2000 to January 2003
- Employed as Design Engineer at Black & Veatch Corporation, Louisville, KY
- Responsible for coordination of air permitting requirements for a $70 million design-build project for wastewater solids processing. Coordinated training for plant staff. Performed field review for development of as-built drawings.
- Detailed design of influent pumping station and associated yard work. Coordinated design support groups. Developed hydraulic profile of new and future treatment facilities. Responsible for obtaining required permits and approvals.
- Assisted with determination of future treatment costs for a 20-year facility plan for a 130-mgd water utility. Reviewed client's specifications for distribution system projects. Determined storage and feed capacity of chemical equipment.
- Drafted preliminary engineering report for $15 million water distribution system expansion. Researched permits required for construction of project.

May 1998 to June 2000
- Employed as Staff Engineer at Black & Veatch Corporation, Greenville, SC
- Responsible for shop-drawing review and maintenance of construction correspondence databases for a $25 million wastewater plant expansion to 7.5 mgd.
- Preparation of scope of work, specifications, and cost estimate to provide assistance to achieve improved NPDES permit compliance for in-plant sewer overflows.
- Served as project engineer for comprehensive facility plan of a 60-mgd plant that evaluated unit process operation and expansion to 90 mgd. Responsible for hydraulic evaluation of plant, drafting of technical memoranda, and coordination of personnel.

August 1995 to May 1998
- Attended Virginia Polytechnic Institute and State University
- Received M.S. in Environmental Engineering
- Final GPA: 4.0 (Summa Cum Laude)

August 1991 to May 1995
- Attended West Virginia University
- Received B.S. in Mechanical Engineering
- Final GPA: 3.6 (Magna Cum Laude)

11. Publications: [including under maiden name of Vickie Lien Burris]

Burris, V. L. and Little, J. C. (1998). Bubble dynamics and oxygen transfer in a hypolimnetic aerator, *Water Science & Technology*, **37** (2) 293-300.
Burris, V. L., McGinnis, D. F. and Little, J. C. (2002). Predicting oxygen transfer and water flow rate in airlift aerators. *Water Research*, **36**, 4605-4615.

Singleton, V.L. and Little, J.C. (2006). Designing hypolimnetic aeration and oxygenation systems – A review, *Environmental Science and Technology*, **40**, 7512-7520.

Singleton, V.L., Gantzer, P. and Little, J.C. (2007). Linear bubble plume model for hypolimnetic oxygenation – Full-scale validation and sensitivity analysis, *Water Resources Research*, **43**, W02405.

12. Other projects

December 2004 to January 2005
- Drafted responses to Virginia Department of Environmental Quality questions regarding dissolved oxygen criteria for lakes and reservoirs

March to May 2005
- Lake oxygenation modeling expert for oxygenation pre-pilot design investigation for Onondaga Lake, NY

July 2005
- Co-author author for technical report "Development of Building Blocks to Prescribe Ecological Flows for the Rivanna River Watershed"

December 2006
- Second author for technical report "Review of Oxygenation Technologies with Special Reference to Application in the Upper Swan Estuary"

February 2004 to present
- Critical peer review of nine manuscripts submitted by other researchers for journal publication

Exhibit B

Bubble Plume Modeling for Lake Restoration

Alfred Wüest

Environmental Physics, Institute for Aquatic Sciences and Water Pollution Control
Eidgenössische Technische Hochschule, Zurich, Switzerland

Norman H. Brooks

W. M. Keck Laboratory of Hydraulics and Water Resources, California Institute of Technology, Pasadena

Dieter M. Imboden

Environmental Physics, Institute for Aquatic Sciences and Water Pollution Control
Eidgenössische Technische Hochschule, Zurich, Switzerland

A steady bubble plume model is developed to describe a weak air (or oxygen) bubble injection system used for the restoration of deep stratified lakes. Since the model is designed for two modes of operation, i.e., oxygenation and artificial mixing, gas exchange between water and bubbles has to be included. The integral model is based on the entrainment hypothesis and a variable buoyancy flux determined by the local plume properties and the ambient water column. Fluxes of eight properties are described by nonlinear differential equations which can be numerically integrated. In addition, five equations of state are used. The model leaves open two initial conditions, plume radius and plume velocity. Model calculations with real lake water profiles demonstrate the range of applicability for both modes of operation. The model agrees reasonably well with field data and with laboratory experiments conducted by various investigators.

1. Introduction

In spite of enormous efforts made to fight lake eutrophication, in many lakes concentrations of phosphorus and other planktonic nutrients are still far above critical values [*Rast and Lee*, 1983]. As a consequence of high primary productivity values, oxygen concentrations in the hypolimnion of eutrophic lakes drop to low values or even to zero. So-called internal lake restoration measures have been designed to improve the hypolimnic oxygen levels and to limit the recycling of phosphorus from the sediments into the lake water [*Imboden*, 1985]. Two restoration techniques which can be used separately or in combination are (1) artificial mixing of the water column during the cold season and (2) input of oxygen into the hypolimnion during summer in such a way as to preserve the stratification.

Artificial mixing is technically simpler and also cheaper and is thus usually the first method to be evaluated. It is designed to add extra mixing energy to the lake at the time when the density stratification is weakest in order to allow water exchange down to the very bottom, or, if mixing occurs naturally, to prolong the period of mixing. Complete mixing maximizes the uptake of oxygen by natural gas exchange at the water surface. In fact, incomplete mixing may not only result from low wind exposure but may also be a consequence of lake eutrophication: Mineralization of biomass in the hypolimnion often leads to the steady accumulation of dissolved substances in the deep waters and thus to a chemically induced permanent stratification [*Joller*, 1985]. In some lakes, the hypolimnic oxygen reserves may not be large enough to prevent the hypolimnion from becoming anoxic during the summer, even if complete saturation had been achieved during the winter. In such situations, oxygen can be artificially introduced into the hypolimnion during the summer. This is commonly combined with artificial mixing during the winter.

Artificial mixing is achieved, in most cases, by injecting compressed air into the deepest part of the lake. However, different technical systems have been designed for the injection of oxygen into a stratified lake. One frequently used system is the Atlas-Copco "Limno" device [*Bucksteeg and Hollfelder*, 1978]. This system consists of two concentric tubes placed vertically in the water column. Air is pumped into the lower end of the inner tube, in which the water rises, then sinks back through the outer tube and leaves the system through outlets placed at the appropriate depth.

In this article a different approach is described. The system "Tanytarsus," designed by the two Swiss engineers, E. Jungo and U. Schaffner, is presently in operation in several deep Swiss lakes [*Imboden*, 1985; *Stadelmann*, 1988; *Stöckli and Schmid*, 1987]. The system uses the same lake installation for both the injection of compressed air for artificial mixing in winter and the injection of pure oxygen into the hypolimnion in summer (Figures 1a and 1b). Pure oxygen is used for hypolimnic oxygenation to prevent the accumulation of molecular nitrogen which can be toxic to fish [*Fast and Hulquist*, 1982].

Both modes of operation are physically similar. The main difference between them consists in the choice of the initial bubble radius and the selection of either natural air or pure oxygen. During the winter the air bubbles have to be large enough to guarantee that the buoyancy force acts up to the lake surface. In contrast, for efficient oxygenation, the oxygen bubbles have to be small enough to dissolve completely in the oxygen-poor hypolimnion before entering the
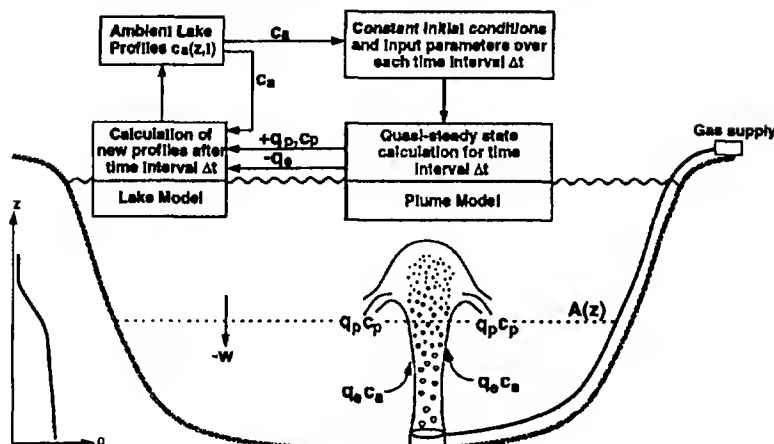
Fig. 1a. Schematic diagrams of the application of the bubble injection system (below) and of the coupling of the plume model with a water quality lake model (above). The two models should run independently of one another, alternating over a short time interval (steady input) to supply one another with their respective required input variables. Labeled quantities are those appearing in (24) and (25).

oxygen-rich surface waters. In addition, the bubble plume should be weak enough so that the induced water circulation is restricted to the hypolimnion. Otherwise, the induced flux of nutrients from the hypolimnion into the epilimnion could further stimulate primary production in the lake.

Diffusors for both modes of operation have been successfully designed and employed in several medium-sized Swiss lakes (Baldeggersee, Sempachersee, Hallwilersee). In order to optimize design and operation of the installations with respect to oxygen input and energy consumption it is important to gain a better understanding of the behavior of the bubble plume in a stratified environment. In this article, classical plume theory is extended to include gas-water exchange of oxygen and nitrogen as well as bubble expansion due to decreasing pressure during bubble rise. The mathematical plume model is presented in sections 2.1–2.6; then the relationship of the plume model to an overall lake model is discussed briefly in section 2.7. In section 3 the model is applied to the two standard cases of operation, oxygenation and artificial mixing, respectively, and compared with a field experiment. Results and questions remain-

Fig. 1b. Top view of one diffusor unit, consisting of 54 tubes (courtesy of Ingenierbüro Jungo, Zürich, Switzerland).

ing open are discussed in section 4, and conclusions are given in section 5.

2. Development of the Bubble Plume Model in Stratified Water

2.1. Previous Work

Air bubble plumes, induced by the steady release of air into water, have been widely studied both experimentally and theoretically. Previous work, which has been mainly concentrated on plumes in homogeneous water, has revealed various characteristics of the flow: the Gaussian radial distribution of plume velocity and bubbles, the similarity of the radial profiles at different distances from the source, and the entrainment of the surrounding water. Measurements have been carried out over a wide range of water depths from centimeters [Durst et al., 1986] to meters [Kobus, 1973; Ditmars and Cederwall, 1974; Goossens, 1979; Fannelop and Sjoen, 1980; Milgram and Van Houten, 1982] and up to tens of meters [Topham, 1975; Milgram, 1983] with airflow rates from $4 \times 10^{-7} N$ m^3 s^{-1} (weak plume [Leitch and Baines, 1989]) to 0.66 N m^3 s^{-1} (strong plume [Topham, 1975]).

Theoretical investigations followed the early work of Ditmars and Cederwall [1974], who applied the integral theory of a single-phase plume [Morton et al., 1956] to the two-phase bubble plume. The theory is based on the horizontally integrated equations of conservation of mass, momentum and buoyancy and on the entrainment hypothesis, which states that the volume of entrained water per unit height is proportional to both the local plume velocity and the plume circumference. Compressibility of the air and bubble slipping, i.e., the differential velocity between rising bubbles and the plume water, are two features which are usually also included in bubble plume models. The effect of turbulent transport within the plume was taken into account by Milgram [1983] who introduced the momentum amplification factor γ (ratio of total momentum flux to the momentum flux carried by the mean flow).
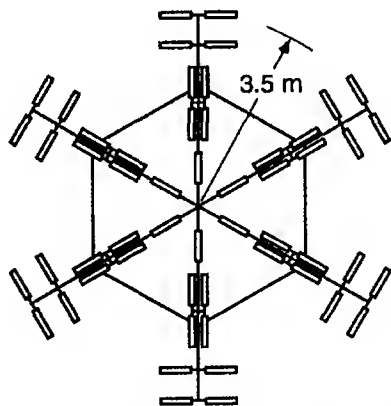
Far less work has been done on stratified water bodies.

McDougall [1978] generalized the integral model for a stratified ambient fluid. Experiments, carried out in strongly stratified [*McDougall*, 1978] and weakly stratified [*Hussian and Narang*, 1983] water revealed a double plume structure in which the bubbles remain in the center part, whereas the pure liquid outer part of the plume can spread out at certain levels.

If bubble plumes are applied to destratify lakes and reservoirs it is important to optimize the airflow rates required to overcome a given stratification. A concept of maximum efficiency was demonstrated experimentally for linear stratification by *Asaeda and Imberger* [1988]. *Patterson and Imberger* [1989] combined *McDougall*'s [1978] bubble plume model with the one-dimensional dynamic lake model DYRESM to evaluate destratification in response to air bubble plumes and weather. With a similar goal in mind, *Zic and Stefan* [1990] have even developed models to simulate the entire flow field induced by a bubble plume in a lake.

In this section, the integral plume theory will be extended to include not only bubble expansion [*Ditmars and Cederwall*, 1974], but also gas exchange (dissolution and stripping) for the dynamics of a buoyant plume. Previous investigators have not included the latter feature, which is important in deep lakes and for weak plumes. The bubble model will also include the effects of density stratification due to gradients of both vertical temperature and dissolved solids. The model can cope with arbitrary ambient profiles of dissolved oxygen and nitrogen.

2.2. Model Features and Assumptions

Previous investigators have presented the basic equations for bubble plumes, and discussed the problem of estimating suitable parameters such as the entrainment coefficient, α, and the spreading ratio of bubbles to fluid flow, λ. The new features of the proposed model for lake use are (1) finite source diameter; (2) induced vertical water velocity at the level of the diffusor as an initial condition; (3) exchange of gases (oxygen and nitrogen primarily) between bubbles and liquid in the plume; (4) conservation equations for specific gases in both dissolved and gas phases; (5) variable gas composition of bubbles during rise; and (6) arbitrary ambient profiles for temperature, salinity (mass of dissolved solids per mass of solution), and dissolved oxygen and nitrogen. Other features included in the plume model are variable bubble radius due to expansion and dissolution; bubble slip velocity and gas mass transfer coefficient as a function of bubble radius, and solubility constants for oxygen and nitrogen as a function of temperature.

The principal assumptions used in developing the model for a steady rising bubble plume in uniform or stratified environment are as follows:

1. The variation of the effective mass density, $\Delta\rho$, is important only in the gravity terms and not for mass or momentum fluxes (Boussinesq assumption, as in all plume theories). This is also equivalent to assuming relative gas volume concentration $V_g \ll 1$.

2. The mass density of gas is neglected compared to that of water in the momentum equation.

3. Uniform distributions ("top hat") across the plume are assumed for water velocity, temperature, dissolved solids, dissolved gases and bubble velocity and concentra-
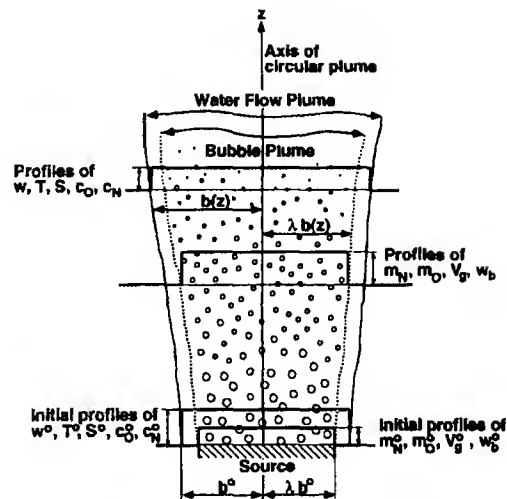
Fig. 2. Diagram defining the bubble plume geometry, showing circular "top hat" distributions. The top hat radius of the bubble core, λb, is smaller than the plume radius b. The latter is assumed to apply for all properties of dissolved species, including temperature (T) and plume velocity (w). Variables are defined in Tables 1, 3a and 3b.

tion (as well as for individual gases) (Figure 2). This is simpler than trying to use Gaussian profiles, and will yield all the correct scaling relationships; also for large sources whose size is a significant fraction of the depth, we avoid the need for special treatment of a zone of flow establishment, during which top hat profiles at the source would have to change to Gaussian profiles. *Morton* [1959] and *Fannelop and Sjoen* [1980] have shown that the top hat distribution captures the main flow features, and that only the constants need to be adjusted.

4. The plume radius b for dissolved species (dissolved solids and dissolved nitrogen and oxygen) and temperature is assumed to be equal to the radius of the top hat plume velocity, whereas that for the bubbles is only λb, where $\lambda \leq 1$. (Although it is expected that dissolved substances will actually spread slightly faster than momentum, such a distinction is an unnecessary complication in this case where the bubbles are the major source of buoyancy.)

5. Ambient currents (other than the plume entrainment velocity) are assumed to be zero.

6. The plume is fully turbulent.

7. The turbulent transport of momentum and scalar quantities (heat, salinity, gases) is neglected compared to advective transport calculated from the mean flow. This is equivalent to taking *Milgram*'s [1983] momentum amplification factor equal to 1.0, which appears reasonable from his experiments.

8. The bubble source is assumed to produce bubbles at a constant rate uniformly distributed over the circular source area of radius λb°.

9. Bubble coalescence is neglected, or else the rate of change of the number of bubbles is prespecified. In this model, the number flux of bubbles, N, is kept constant with height and equal to the number flux at the source.

10. The bubbles are all of uniform size (or are adequately represented by a suspension of equal bubbles). If instead a bubble size spectrum were prespecified, it would be possible

TABLE 1. List of the Eight Basic Plume Variables

Variable	Symbol	Units
Vertical velocity of the plume water	w	m s^{-1}
Plume radius for velocity and dissolved species	b	m
Temperature of plume water and bubbles	T	°C
Total dissolved solids in plume water*	$S\rho_w$	kg m^{-3}
Concentration of dissolved O_2	c_O	mol m^{-3}
Concentration of dissolved N_2	c_N	mol m^{-3}
Concentration of gaseous O_2†	m_O	mol m^{-3}
Concentration of gaseous N_2†	m_N	mol m^{-3}

Variables with index a, i.e., T_a, S_a, c_{Oa}, c_{Na}, describe "ambient" (i.e., lake water) properties.
*S denotes salinity (mass of salt per mass of solution).
†Amount of gas per unit bulk volume of the bubble-water mixture within the bubble plume of radius λb.

to replace the number flux of bubbles N by an array $N(r_1, \cdots, r_n)$ and to calculate the fate of the individually sized bubbles independently.

11. Water properties of the initial plume are those of lake water at that depth (where the diffusor is installed).

12. Gas exchange between water and bubbles for gases other than oxygen and nitrogen (e.g., argon, carbon dioxide, methane) is neglected. However, other gases could easily be included in the model by adding the relevant conservation equations.

2.3. Conservation Equations

There are eight basic plume variables (Table 1) to be calculated by simultaneous integration of eight differential equations describing the plume dynamics based on the conservation laws for mass, momentum, and heat (Table 2). Several additional parameters are introduced into the model which can be calculated either from the corresponding equations of state (Table 3a) or from empirical approximations taken from the literature (Table 3b). In the following the reader is referred to Tables 1–3 for the definition of variables and parameters.

Continuity for plume water flow. The rate of change of the volume flow is given by the entrainment of ambient water into the plume:

$$\frac{d}{dz} [\pi b^2 w(1 - \lambda^2 V_g)] = 2\alpha \pi b w \quad (\text{m}^2 \text{ s}^{-1}) \quad (1)$$

where z is the vertical coordinate (positive upward) and α, the entrainment coefficient for the top hat plume, is $\sqrt{2}$ times the corresponding value used for a Gaussian plume model, α_g, i.e.,

$$\alpha = \sqrt{2} \, \alpha_g \quad (\text{dimensionless}) \quad (2)$$

as explained by *Morton* [1959]. Furthermore, the top hat radius is

$$b = \sqrt{2} \, b_g \quad (\text{m}) \quad (3)$$

where b_g is the plume width in the Gaussian model ($w = w_m \exp (-r^2/b_g^2)$). The term $\lambda^2 V_g$ is a correction for the volume occupied by the gas bubbles. Since $V_g < 10^{-2}$ for bubble plumes of interest for lake restoration, and following the Boussinesq assumption, we may rewrite the equation without the V_g term:

$$\frac{d}{dz} (\pi b^2 w) = 2\alpha \pi b w \quad (\text{m}^2 \text{ s}^{-1}) \quad (4)$$

Momentum flux. We may again neglect the gas volume and gas momentum in calculating the momentum flux $M = \pi b^2 w^2$ of the plume. The rate of change of M with height z is equal to the buoyant force per unit height of the plume:

$$\frac{d}{dz} (\pi b^2 w^2) = \frac{\rho_a - \rho_p}{\rho_p} g \pi b^2 \lambda^2$$

$$+ \frac{\rho_a - \rho_w}{\rho_p} g \pi b^2 (1 - \lambda^2) \quad (\text{m}^3 \text{ s}^{-2}) \quad (5)$$

(ρ_a and ρ_w are densities of ambient and plume water, respectively, and ρ_p is the density of the plume bubble-water mixture). On the right-hand side the first term gives the buoyant force for the area of the bubble distribution top hat, $\pi \lambda^2 b^2$. The second term is the (negative) buoyancy for the fluid inside the annulus (Figure 2) between the bubble top hat (radius λb) and the plume velocity top hat (radius b). When there is no ambient fluid stratification ($\rho_a = \rho_w$) or when $\lambda \approx 1$, the second term vanishes.

Heat or temperature flux. Assuming that the coefficient

TABLE 2. Definition of the Eight Integrated Flux Variables

Variable	Formula	Units
Volume flux of plume water	$\mu = \pi b^2 w$	m^3 s^{-1}
Momentum flux	$M = \pi b^2 w^2$	m^4 s^{-2}
Temperature flux (relative to $T = 0$°C)	$F_T = \mu T$	°C m^3 s^{-1}
Flux of total dissolved solids	$F_S = \mu S \rho_w$	kg s^{-1}
Flux of dissolved O_2, N_2	$D_i = \mu c_i$; $i = O$, N	mol s^{-1}
Flux of gaseous O_2, N_2	$G_i = \pi b^2 \lambda^2 (w + w_b) m_i$, $i = O$, N	mol s^{-1}

TABLE 3a. Equations of State

Parameter	Equation	Comments
Partial pressures within bubble at depth z	$p_i = [m_i/(m_O + m_N)]p = [G_i/(G_O + G_N)]p$ for $i = O, N$ (bar)	Total pressure p is given by the hydrostatic approximation
Total pressure	$p = p_s + a \int_z^{z_s} \bar{\rho}_a g\, dz = p_s + a\,\bar{\rho}_a\, g(z_s - z)$ (bar)	p_s is atmospheric pressure at lake surface (bar); z is vertical distance above diffusor (m); z_s is height of lake surface above diffusor (m); g is acceleration of gravity, equal to 9.81 m s^{-2}; $\bar{\rho}_a$ is mean density of ambient water; and a is a pressure conversion factor (pascals to bars), equal to 10^{-5} bar kg^{-1} m s^2.
Water density at atmospheric pressure	$\rho_a = f_T(T_a) + f_s(S_a)$ for ambient lake water, $\rho_w = f_T(T) + f_s(S)$ for plume water	$f_T(T) = 999.868$ kg m^{-3} + 10^{-3} $[a_1 T + a_2 T^2 + a_3 T^3]$; $a_1 = 65.185$ kg m^{-3} °C^{-1}; $a_2 = -8.4878$ kg m^{-3} °C^{-2}; $a_3 = 0.05607$ kg m^{-3} °C^{-3}; $f_s(S) = \gamma S$, where either $\gamma = 0.802$ kg m^{-3} (‰)$^{-1}$ if S is salinity expressed as dissolved salt content in per mil or $\gamma = 0.705 \times 10^{-3}$ kg m^{-3} (μS/cm)$^{-1}$ if S is expressed in terms of the electrical conductivity measured at 20°C (modified after Bührer and Ambühl [1975]).
Density of bubble-water mixture in plume	$\rho_p = (1 - V_g)\,\rho_w$	
Gas volume* Ideal gas law	$V_g = [(m_O + m_N)/p]R\hat{T}$	$R = 8.314$ J mol^{-1} K^{-1} (gas constant) and $\hat{T}$ is absolute temperature of plume water (K)
Van der Waals gas law	Implicit equation for V_g: $[V_g/(m_O + m_N) - b_v]$ $\cdot [p + a_v(m_O + m_N)^2/V_g^2] = R\hat{T}$	$a_v = 1.4 \times 10^{-6}$ bar m^6 mol^{-1}; $b_v = 32 \times 10^{-6}$ m^3 mol^{-1}
Bubble radius	$r = (3V_g \lambda^2 b^2(w + w_b)/4\pi N)^{1/3}$	N is the number flux of bubbles released at diffusor per unit time

*V_g is the gas volume per total volume of the bubble-water mixture in the inner core of the plume (dimensionless).

of specific heat per unit water volume ($\rho_w \kappa$) is constant, and neglecting the heat content of the gas volume, the conservation equation for the heat flux ($\pi b^2 w \rho_w \kappa T$) can be reduced to the corresponding expression for the temperature flux $F_T = \pi b^2 w T$:

$$\frac{d}{dz}(\pi b^2 w T) = 2\alpha \pi b w T_a \quad (°C\ m^2\ s^{-1}) \qquad (6)$$

where T_a is the ambient water temperature given by measured temperature profiles or by the lake model.

Flux of total dissolved solids. For water temperatures close to 4°C, the concentration of dissolved solids, ex-

pressed by the salinity S, plays a role in establishing the density stratification. Hence it is necessary to include the mass balance for dissolved solids:

$$\frac{d}{dz}(\pi b^2 w \rho_w S) = 2\alpha \pi b w \rho_a S_a \quad (kg\ m^{-1}\ s^{-1}) \qquad (7)$$

where S_a is the ambient salinity.

Fluxes of dissolved oxygen and nitrogen. There are two gases of interest, molecular oxygen (O_2) and nitrogen (N_2), and two phases, dissolved and gaseous, for each. For each species the gas transfer term appears as a gain (or loss) in the dissolved gas conservation equation and as a loss (or gain) in

TABLE 3b. Parameter Approximations

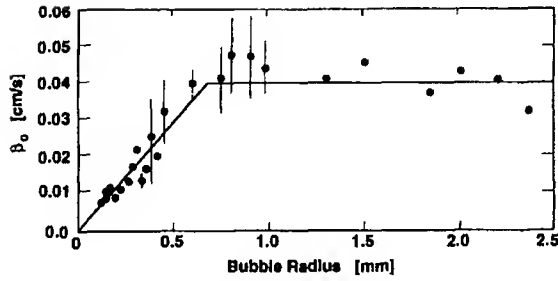| Parameter	Approximation	Units
Bubble slip velocity (Figure 5)	$w_b(r) = w_1(r/r_*)^{1.357}$ $r/r_* < 7.0 \times 10^{-4}$	m s^{-1}
	$w_b(r) = w_2$ $7.0 \times 10^{-4} < r/r_* < 5.1 \times 10^{-3}$	m s^{-1}
	$w_b(r) = w_3(r/r_*)^{0.547}$ $r/r_* > 5.1 \times 10^{-3}$	m s^{-1}
	with $w_1 = 4474$ m s^{-1}; $w_2 = 0.23$ m s^{-1}; $w_3 = 4.202$ m s^{-1}; $r_* = 1$ m	
Gas transfer coefficient for molecular oxygen and nitrogen (Figure 3)	$\beta_i(r) = 0.6$ m s^{-1} (r/r_*) $(r/r_*) < 6.67 \times 10^{-4}$, $i = O, N$	m s^{-1}
	$\beta_i(r) = 4 \times 10^{-4}$ m s^{-1} $(r/r_*) > 6.67 \times 10^{-4}$, $i = O, N$	m s^{-1}
Molecular oxygen solubility constant (Figure 4)	$K_O(T) = K_{O1} + K_{O2}T + K_{O3}T^2$ with $K_{O1} = 2.125$ mol m^{-3} bar^{-1}; $K_{O2} = -0.05021$ mol m^{-3} bar^{-1} °C^{-1}; $K_{O3} = 5.77 \times 10^{-4}$ mol m^{-3} bar^{-1} °C^{-2}	mol m^{-3} bar^{-1}
Molecular nitrogen solubility constant (Figure 4)	$K_N(T) = K_{N1} + K_{N2}T + K_{N3}T^2$ with $K_{N1} = 1.042$ mol m^{-3} bar^{-1}; $K_{N2} = -0.0245$ mol m^{-3} bar^{-1} °C^{-1}; $K_{N3} = 3.171 \times 10^{-4}$ mol m^{-3} bar^{-1} °C^{-2}	mol m^{-3} bar^{-1}
Constants Entrainment coefficient	$\alpha = 0.11$	
Plume radius ratio	$\lambda = 0.8$	

Fig. 3. Mass transfer coefficients β_O for oxygen measured in tap water as a function of bubble radius, based on data (solid circles) compiled by *Motarjemi and Jameson* [1978]. In this model the same mass transfer coefficients for oxygen and nitrogen were used, since the two molecules have nearly identical molecular diffusivities. The solid line shows the parametrization $\beta_O(r) = \beta_N(r)$ used in this paper.

the gas phase conservation equation. The gas flux through bubble surfaces is given by

$$\beta_i(c_{si} - c_i) \quad (\text{mol m}^{-2}\text{ s}^{-1}) \qquad (8)$$

where β_i is the mass transfer coefficient (Figure 3) for the gas species i (O_2 or N_2), c_i is the in situ dissolved gas concentration, and c_{si} is the saturation concentration determined by Henry's law:

$$c_{si} = K_i p_i \quad (\text{mol m}^{-3}) \qquad (9)$$

Here p_i is the in situ partial pressure of the gas phase of species i and K_i is the solubility constant (Figure 4).

In order to calculate the total gas transfer per unit height of the bubble plume we use the total number flux of bubbles, N, a quantity which, according to the list of assumptions (see section 2.2, ninth assumption) is determined by the initial conditions (initial bubble radius r°, total gas input at diffusor and diffusor depth; Tables 3a and 4) and then remains constant within the plume. The number of bubbles per unit plume height is then simply $N/(w + w_b)$, where $(w + w_b)$ is the total bubble velocity (w_b is bubble slip velocity; Figure 5). The total surface area of bubbles per unit plume height is found by multiplying by the area of each bubble, i.e., $4\pi r^2 N/(w + w_b)$. The total gas transfer rate per unit height is then obtained by multiplying this aggregate surface area (per unit height) by the local gas flux:

$$\frac{4\pi r^2 N}{w + w_b}\beta_i(K_i p_i - c_i) \quad (\text{mol s}^{-1}\text{ m}^{-1}) \qquad (10)$$

The conservation equation for each dissolved species i, i.e., O_2 and N_2, includes entrainment of ambient lake water (concentrations c_{ia} for $i = O$ and N) and gas exchange:

$$\frac{d}{dz}(\pi b^2 w c_O) = 2\alpha\pi b w c_{Oa} + \frac{4\pi r^2 N}{w + w_b}\beta_O(K_O p_O - c_O)$$

$$(\text{mol s}^{-1}\text{ m}^{-1}) \qquad (11)$$

$$\frac{d}{dz}(\pi b^2 w c_N) = 2\alpha\pi b w c_{Na} + \frac{4\pi r^2 N}{w + w_b}\beta_N(K_N p_N - c_N)$$

$$(\text{mol s}^{-1}\text{ m}^{-1}) \qquad (12)$$

Fluxes of gaseous oxygen and nitrogen. The rate of change of advective flux of gaseous O_2 and N_2 is equal to the rate of dissolution or stripping as determined above:

$$\frac{d}{dz}[\pi b^2\lambda^2(w + w_b)m_O] = -\frac{4\pi r^2 N}{w + w_b}\beta_O(K_O p_O - c_O)$$

$$(\text{mol s}^{-1}\text{ m}^{-1}) \qquad (13)$$

$$\frac{d}{dz}[\pi b^2\lambda^2(w + w_b)m_N] = -\frac{4\pi r^2 N}{w + w_b}\beta_N(K_N p_N - c_N)$$

$$(\text{mol s}^{-1}\text{ m}^{-1}) \qquad (14)$$

(m_O and m_N are the gaseous concentration of the species per unit bulk volume of the bubble-water mixture). Note that the relevant volume flux for the gaseous components contains the total bubble velocity, $w + w_b$, and the reduced plume radius, λb. Upon solving these equations it is found that the proportion of O_2 and N_2 in the rising gas bubbles is changing. For instance, pure O_2 bubbles will strip N_2 from the water column at the same time that O_2 is being dissolved.

The assumptions made in developing these eight equations could be generalized, but at the price of adding parameters. For instance, one could distinguish five separate top hat radii for velocity, bubbles, dissolved gases, temperature, and salinity (giving four different λ ratios). The refinement is not warranted at this time, since information is lacking on how to select different λ values. Hence, we use only two top hat radii: b for velocity, temperature, salinity, and dissolved gases, and λb for bubbles. It is well known from previous investigations that λ is significantly less than 1, and probably about 0.8 [*Milgram*, 1983].

2.4. Variable Transformation

To simplify the solution we let the basic dependent variables be the eight integrated fluxes defined in Table 2, namely those for water volume, momentum, temperature, dissolved solids and the dissolved and gaseous phases of molecular O_2 and N_2. With these definitions, the eight conservation equations ((4)–(7) and (11)–(14)) may be rewritten in terms of the new variables:

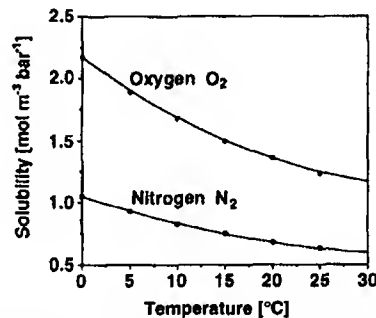$$\frac{d\mu}{dz} = 2\alpha(\pi M)^{1/2} \qquad (15)$$

Fig. 4. Solubility constants K_i of molecular nitrogen and oxygen as functions of temperature. Dots represent values taken from *Marshall* [1976]. Solid lines show second order polynomial fits used in this model.

TABLE 4. Initial Conditions for Bubble Plume Calculation

Initial Plume Variable	Symbol	Method for Determining Initial Value
Plume radius	$b°$	effective radius of the entire diffusor unit (diffusor geometry)
Vertical plume velocity	$w°$	$w°$ depends on source and plume properties; see section 2.5
Volume flux of plume water	$\mu°$	$\mu° = \pi b°^2 w°$
Momentum flux	$M°$	$M° = \pi b°^2 w°^2$
Temperature	$T°$	ambient temperature at diffusor depth
Temperature flux	$F_T°$	$F_T° = \mu°T°$
Dissolved species		
Concentrations	$S°, c_O°, c_N°$	ambient concentrations at diffusor depth
Fluxes	$F_S°, D_O°, D_N°$	$F_S° = \mu°S°, D_O° = \mu°c_O°, D_N° = \mu°c_N°$
Gas fluxes	$G_N°, G_O°$	nitrogen and/or oxygen input rate (mode of operation)
Bubble radius*	$r°$	design (material and porosity) of diffusor
Pressure	$p°$	depth of diffusor (topography and installation) and ambient density profile
Number flux of bubbles†	$N°$	initial gas fluxes, bubble radius and pressure at the diffusor depth (Table 3a)

*It may be possible to vary bubble radius during operation by switching between different installed diffusor tubes. For the system "Tanytarsus" a switch between small (oxygenation mode) and large (artificial mixing mode) bubbles is possible.
†The number flux of bubbles, $N(z)$, is kept constant in the plume: $N(z) = N°$.

$$\frac{dM}{dz} = \frac{\rho_a - \rho_p}{\rho_p} g\lambda^2 \frac{\mu^2}{M} + \frac{\rho_a - \rho_w}{\rho_p} g \frac{\mu^2}{M} (1 - \lambda^2) \tag{16}$$

$$\frac{dF_T}{dz} = 2\alpha(\pi M)^{1/2} T_a \tag{17}$$

$$\frac{dF_S}{dz} = 2\alpha(\pi M)^{1/2} \rho_a S_a \tag{18}$$

$$\frac{dD_O}{dz} = 2\alpha(\pi M)^{1/2} c_{Oa} + \frac{4\pi r^2 N}{(M/\mu) + w_b} \beta_O \left(K_O p_O - \frac{D_O}{\mu} \right) \tag{19}$$

$$\frac{dD_N}{dz} = 2\alpha(\pi M)^{1/2} c_{Na} + \frac{4\pi r^2 N}{(M/\mu) + w_b} \beta_N \left(K_N p_N - \frac{D_N}{\mu} \right) \tag{20}$$

$$\frac{dG_O}{dz} = -\frac{4\pi r^2 N}{(M/\mu) + w_b} \beta_O \left(K_O p_O - \frac{D_O}{\mu} \right) \tag{21}$$

$$\frac{dG_N}{dz} = -\frac{4\pi r^2 N}{(M/\mu) + w_b} \beta_N \left(K_N p_N - \frac{D_N}{\mu} \right) \tag{22}$$

This is a set of eight coupled nonlinear first-order differential equations which can be integrated numerically. The system contains five additional variables (ρ_p, ρ_w, r, p_O, p_N) which are linked to basic variables by equations of state (Table 3a) and thus can be adjusted after every integration step. Furthermore, there are other physicochemical parameters which are either kept constant throughout the model calculation (e.g., relative bubble plume radius λ, entrainment coefficient α) or can be calculated from empirical approximations (Table 3b). The number flux of bubbles N is established by the initial gas volume flux and the assumed initial bubble radius, and then remains constant within the plume.

2.5. Initial Conditions

The model calculations depend crucially on both the initial plume conditions, which are summarized in Table 4, and the ambient lake water profiles. Whereas the ambient profiles are given by the state of the lake (influenced however by the plume operation in the long term, see section 2.7), the initial conditions can be controlled to a certain extent by the design and operation of the diffusor units.

We have to specify the initial values of the eight flux variables defined in Table 2. According to the eleventh assumption, the initial values of temperature $T°$, salinity $S°$, dissolved O_2 concentration c_O and dissolved N_2 concentra-
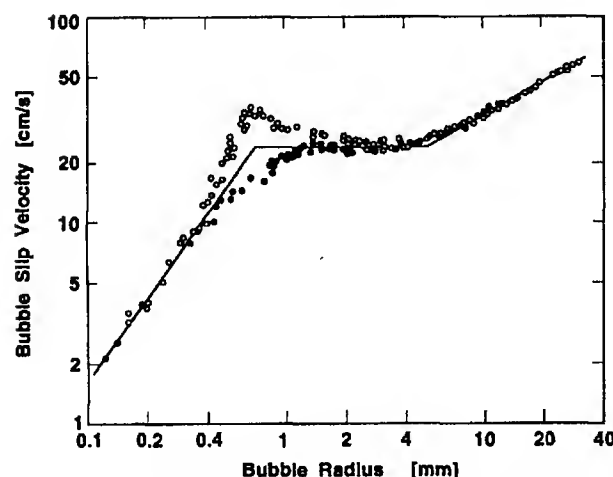

Fig. 5. Terminal slip velocity of air bubbles, w_b, measured in tap water (solid circles) and distilled water (open circles) [Haberman and Morton, 1954]. The solid line represents the approximation used in this model.

tion c_N^o are given by the ambient lake water characteristics at the depth of the diffusor. However, to determine the respective initial fluxes we need to multiply each by the initial volume flux μ^o which is discussed below. The gaseous O_2 and N_2 fluxes, G_O^o and G_N^o, are the key initial variables to be controlled by the mode of operation of the diffusor. The initial bubble radius, r^o, is determined mainly by the design of the diffusor (pore size) and cannot be controlled by varying the gas flow rate (unless it is very large). The number flux of bubbles, $N = N^o$, kept constant in the whole plume, is determined by total gas flux, $G_O^o + G_N^o$, initial bubble radius, r^o, and pressure, p^o (Table 3a), and is not an independent initial condition.

The initial inner plume radius (λb^o) is determined by the apparent size of the bubble source area. Specifying λ and b^o establishes the width of the velocity plume. In practice, a diffusor unit may consist of several diffusor tubes distributed in a starlike pattern of six arms, as shown in Figure 1b [Stadelmann, 1988]. In such cases we consider the area of the entire diffusor unit as a uniform source of buoyancy and consequently set the initial plume area $\pi(\lambda b^o)^2$ equal to the circular area covered by the tubes.

Mathematically, the vertical velocity w^o is an additional independent initial variable. In reality, however, the initial water velocity should be determined by the properties of the source and of the ambient water. It has been found useful to define a densimetric Froude number (dimensionless) as

$$Fr = \frac{w'}{[2\lambda b g (\rho_a - \rho_p)/\rho_p]^{1/2}} \qquad (23)$$

For a single-phase plume Fr is simply inversely proportional to the local Richardson number Ri [Fischer et al., 1979] which has the unique value of 0.557 along the plume, except near the source. The constant of proportionality depends on the type of plume profiles being used; here $Fr = (\pi/4)^{1/4} Ri^{-1}$. Thus the Froude number of the plume should everywhere have a value of 1.69, except near the source. However, for bubble plumes there is an additional characteristic velocity, the bubble slip velocity w_b. Thus we do not expect a unique starting condition to exist. For very small bubbles $(w_b \rightarrow 0)$, the initial Froude number should be the same as for a single-phase plume. From the model calculations that follow we find that as z increases, Fr does indeed tend to a nearly constant value of about 1.7. For initial values of $Fr^o < 1.5$, the plume water velocity w initially (immediately above the diffusor) increases with increasing z (reasonable behavior), while for $Fr^o > 1.5$, w first decreases in the model (unlikely). Therefore, for the standard case (section 3.1) we use the value in between, namely, $Fr^o = 1.6$, and for the sensitivity analysis (section 3.2) we analyze the effect of varying Fr^o values.

2.6. Solution Procedure

The stationary solution for the flux variables (Table 2) is calculated by a three-step iteration loop. In the first step the eight differential flux equations ((15)–(22)) are integrated using the standard first-order Euler method, starting from the initial values listed in Table 4. The vertical coordinate increment dz is controlled by keeping the maximum relative change of the flux variables below a chosen value (1‰). By sensitivity analysis it was found that the 1‰ criterion is sufficiently small to guarantee that the final values of the

plume variables (Table 1) are not increment dependent (<1‰ relative error). After each iteration the equations of state (Table 3a) are solved for the partial pressure of O_2 and N_2 (p_O, p_N), the water and plume densities (ρ_w, ρ_p), and the bubble radius (r). In the third and last step, the remaining parameters, bubble slip velocity, w_b (Figure 5), mass transfer coefficients, β_i (Figure 3), and the solubility constants, K_O and K_N (Figure 4), are calculated from the parameterization listed in Table 3b.

The iteration is interrupted and the program stopped when the plume velocity approaches zero or when the plume reaches the surface. Comparison of the final plume water density with the ambient density profile then allows the determination of the equilibrium depth, i.e., the depth to which the plume water would sink back if no further mixing occurred. However, the fallback plume (which we do not attempt to model) entrains some additional water on the way down; as a result, in reality it does not fall back completely to the calculated equilibrium depth.

2.7. Plume Model in Relation to Lake Model

The plume model is only one component of the overall lake model. In the simplest case, the lake is considered to consist of two parts: the small plume zone (one or more vertical columns) and the much larger lake zone outside the plumes (Figure 1a). The lake zone may in many cases be considered to be horizontally well mixed or uniform in properties (such as temperature T or dissolved O_2); i.e., $T_a(x, y, z, t) = T_a(z, t)$.

The plume is assumed to be in quasi-steady state, operating for some period of time Δt (of the order of days) with essentially fixed ambient environmental profiles determined by the lake zone. Then the lake zone profiles are adjusted to reflect the results of the plume action over the given time period Δt. In other words, the ambient profiles change so slowly that they may be considered piecewise constant for the purpose of the plume calculations.

The presentation of the lake zone model is not the purpose of this paper. However, for just the physical aspects, the basic equations for coupling to the plume model are conservation of water mass and conservation of any scalar species or pollutant. For conservation of water mass at level z, the vertical rate of change of the vertical flow, wA, through the lake cross section A (w is far-field vertical upward velocity, Figure 1a), is equal to the plume outflow per unit height $q_p(z)$ minus the plume entrainment $q_e(z)$:

$$\frac{d(wA)}{dz} = q_p - q_e \quad (\text{m}^2 \text{ s}^{-1}) \qquad (24)$$

By definition, either one or the other of q_p and q_e must be zero at a particular level z; i.e., the plume is either entraining $(q_p = 0)$ or detraining $(q_e = 0)$.

In the far field of the lake the mass balance of any conservative substance with concentration $c_a(z)$ is given by

$$A \frac{\partial c_a}{\partial t} + \frac{\partial (c_a w A)}{\partial z} = q_p c_p - q_e c_a \quad (\text{mol s}^{-1} \text{ m}^{-1}) \qquad (25)$$

where c_a and c_p describe ambient and mean plume concentrations, respectively.

The plume model uses $c_a(z)$ (and $T_a(z)$) as inputs, and produces $a_\sim$, $a_\sim$, and $c_\sim$ as outputs (Figure 1a) which are used to compute new values of w and c_p at given time

TABLE 5. Characteristics of Internal Lake Restoration Measures in Baldeggersee (Switzerland)

Parameter	Value or Description
Lake Data	
Location	47°12'N, 8°16'E, (15 km north of Lucerne, Switzerland)
Surface altitude	462 m above sea level
Surface area	5.2 km^2
Volume	176 × 10^6 m^3
Maximum depth	66 m
Oxygenation Mode (May–October)	
Operation	four to six diffusors at depth between 42 and 64 m
Total O$_2$ input	3–4.5 × 10^3 kg d^{-1} 0.025–0.037 N m^3 s^{-1}*
O$_2$ input per diffusor unit	~0.005–0.007 N m^3 s^{-1}
Artificial Mixing Mode (November–April)	
Operation	three to four diffusors or nozzles at depth between 58 and 64 m
Total air input	0.056 N m^3 s^{-1}
Air input per diffusor unit	0.014–0.017 N m^3 s^{-1}

*1 N m^3 = 1 m^3 of gas at 1 bar and 0°C.

intervals Δt by finite difference equations representing the lake model (equations (24) and (25)). This procedure was demonstrated by *Imboden* [1985].

3. The Case of Baldeggersee: Application and Sensitivity Evaluation of the Model

In this section application of the model to Baldeggersee, a highly eutrophic lake (Table 5), is described. Among all

Swiss lakes, Baldeggersee has the longest record of artificial oxygen and air input [*Imboden*, 1985]. Artificial destratification with an air bubble plume began in February 1982 followed by a first experimental oxygenation of the hypolimnion using pure oxygen during the next summer.

Vertical profiles of O$_2$, temperature and salinity measured in July 1983 (oxygenation) and November 1983 (artificial mixing) are chosen as the input data to run the bubble plume model (Figure 6). Measured N$_2$ profiles in Baldeggersee were approximately constant and close to the surface saturation value in winter. Hence a constant value of c_N = 0.71 mol m^{-3} (20 g m^{-3}), corresponding to N$_2$ saturation at T = 4°C at the altitude of Baldeggersee, was taken as the ambient N$_2$ concentration. It is assumed that the density of the water is defined only by the temperature and the concentration of dissolved solids, which consist mainly of Ca^{2+} and HCO$_3^-$. The influence of dissolved solids on the vertical density gradient is negligible in the thermocline of most lakes, although in the prerestoration period chemical density gradients in the deep hypolimnion may be important as well [*Joller*, 1985]. The ambient density profiles for July and November 1983 shown in Figure 6d were calculated from water temperature and electrical conductivity using the modified equations given by *Bührer and Ambühl* [1975] (Table 3a).

3.1. The Standard Cases

The model calculations are based on two standard situations as listed in Table 6. Since the initial values of plume size, vertical plume velocity and bubble radius are not exactly known, reasonable values for the standard cases
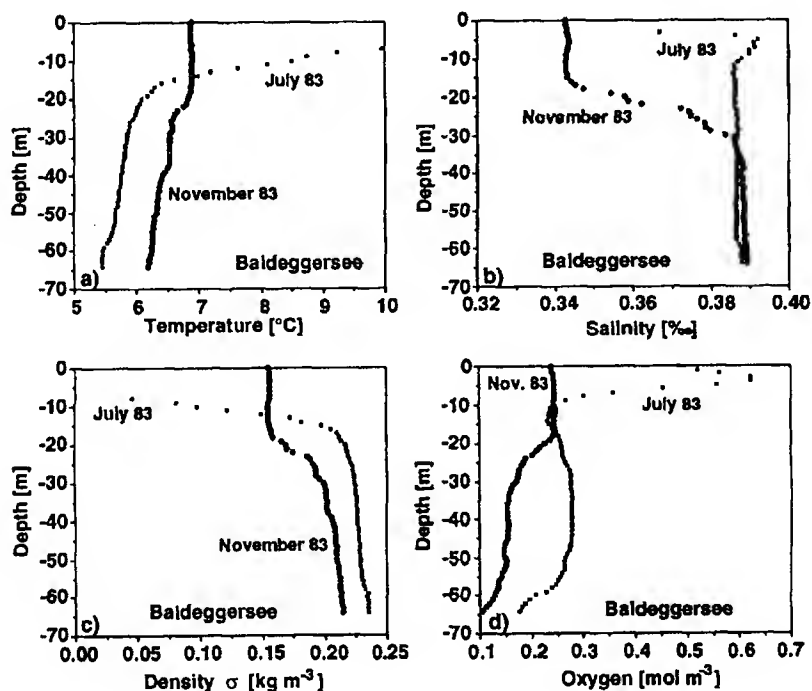

Fig. 6. Temperature, salinity, density ($\sigma = p - 1000$ kg m^{-3}), and oxygen profiles, measured in July (solid squares) and November (open circles) 1983 in Baldeggersee. These profiles serve as input data for the two standard case model calculations.

TABLE 6. Model Input Values for One Diffusor Unit, Applied to Standard Case and Sensitivity Analysis

Parameter		Standard Case	Sensitivity Analysis
Diffusor depth, m	z^o	65	n.v.*
Initial plume size, m^2	πb^{o2}	20	0–50
Entrainment factor	α	0.11	0.05–0.2
Oxygenation			
O$_2$ input,† N m^3 s^{-1}		0.0062	0.001–0.1
Initial Froude number‡	Fr^o	1.6 ($w^0 = 0.125$ m/s)	1.0–2.0
Initial bubble radius, m	r^o	0.001	10^{-4} to 10^{-1}
Temperature, salinity and oxygen profiles		July 1983 (Figure 6)	n.v.
Artificial Mixing			
Air input,† N m^3/s		0.014	n.v.
Initial Froude number‡	Fr^o	1.6 ($w^0 = 0.172$ m/s)	0.5–2.5
Initial bubble radius, m	r^o	0.006	n.v.
Temperature, salinity and oxygen profiles		Nov. 1983 (Figure 6)	n.v.

*Here n.v. denotes not varied.
†1 N m^3 = 1 m^3 of gas at 1 bar and 0°C.
‡See section 2.5 for the choice of the initial Froude number, equation (23).

were selected followed by a sensitivity analysis of the model results with respect to these choices. The calculated vertical variations of important model variables along the plume are shown in Figure 7 for both modes of operation, i.e., pure oxygen input during the summer and air input during the winter.

The most important difference between the two cases (Table 6) lies in the initial bubble radius, i.e., 1 mm in July versus 6 mm in November. During oxygenation (July) the

surface-to-volume ratio of the bubbles is large. The bubbles dissolve quickly and their volume is only 0.1% of the initial value at about 40 m depth (Figure 7c). When the bubbles disappear, the colder and heavier water from the lake bottom loses its buoyancy (Figure 7e), the plume stops (Figure 7a), disperses, sinks part way, and merges with the surrounding lake water at the depth of neutral density. The model calculation is restricted to the zone where the plume is still rising. At the depth of maximum plume rise (DMPR) some
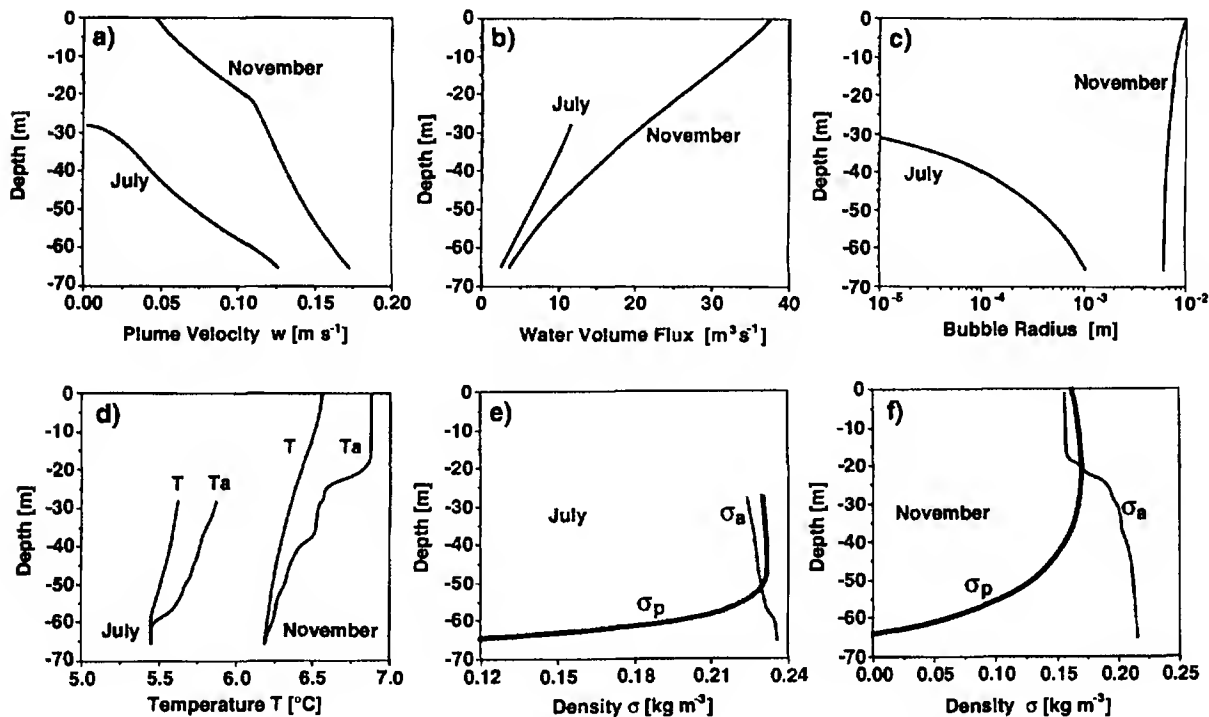

Fig. 7. Model calculations for bubble plumes in Baldeggersee using standard parameters from Table 6 and ambient profiles from Figure 6. Profiles of important model variables along the vertical plume axis are shown for the two modes of operation: oxygenation during summer (July) and artificial mixing with compressed air during winter (November).
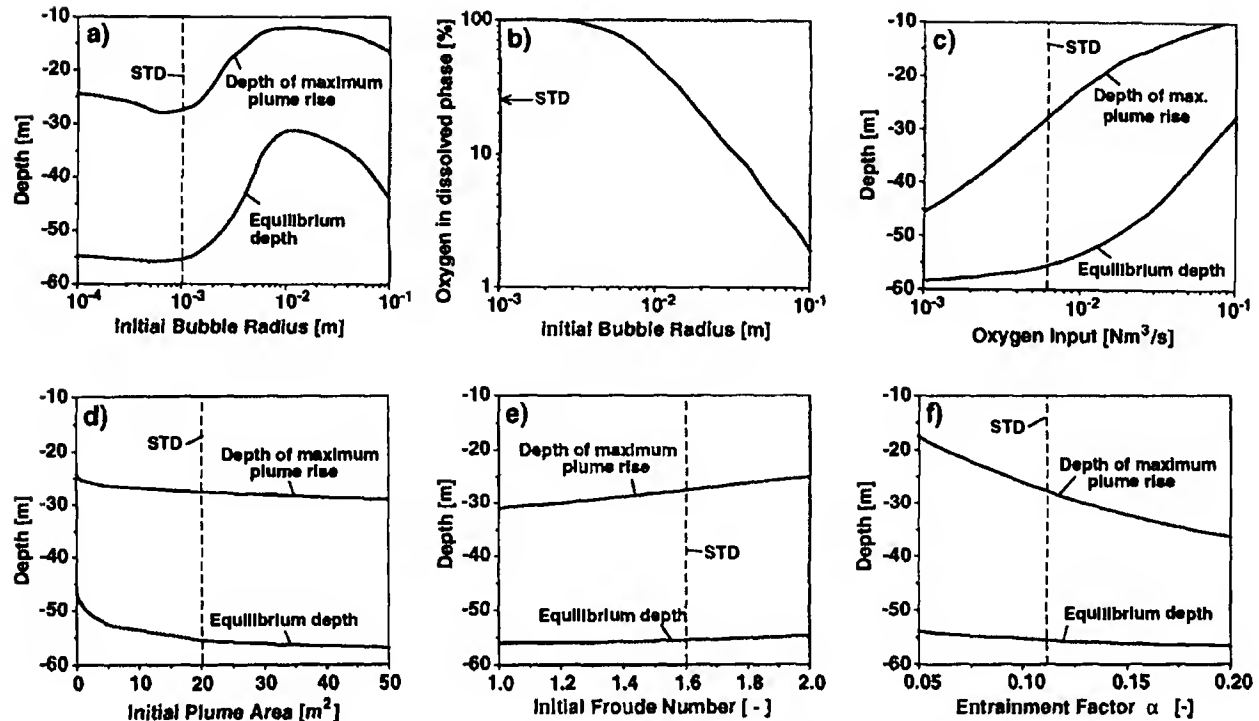
Fig. 8. Sensitivity of plume model calculated for the case of oxygen input into Baldeggersee using the standard situation of July 1983 (Table 6). Only one parameter is varied from its standard value (labeled by "STD") for each calculation. See text for definition of equilibrium depth.

bubbles may still exist if the system operates with large enough bubbles. Possible further dissolution or secondary plume creation [McDougall, 1978] by the escaping bubbles above DMPR is not considered in this model. If small bubbles are used, however, they disappear before the DMPR is reached. In the momentum overshoot phase of negative buoyancy no secondary plumes have to be considered; the plume then behaves as an ordinary one [Morton et al., 1956].

In contrast, during artificial mixing with air (November), gas exchange is slower since the bubbles have a larger initial radius. The rate of increase in bubble size due to decompression is similar to the rate of decrease due to dissolution. The net effect, however, is a slight increase in the in situ bubble radius (Figure 7c). Therefore, the plume retains its buoyancy up to 20 m below the lake surface (Figure 7f). The remaining momentum brings the plume to the surface (Figures 7a and 7b).

Note that the differences between the summer and winter cases are primarily related to the different initial bubble sizes; the chemical composition of the bubbles (oxygen or air, respectively) is less important for deep lakes since the high hydrostatic in situ pressure makes the gas exchange rate nearly independent of the ambient dissolved gas concentration at this depth.

The larger size of the bubbles is not the only reason why, in the artificial mixing case, the plume reaches the surface. Higher gas flux and weaker ambient stratification also support stronger plumes. Higher gas flux leads to a larger density difference (i.e., buoyancy), and a higher initial plume velocity (momentum flux). The weak stratification of the water column provides little negative buoyancy to stop the

plume. The effects of initial gas flux and bubble size on the plume will be investigated in the following sensitivity analysis.

3.2. Sensitivity Analysis

With respect to the application of the model to internal lake restoration the most important model characteristics are the vertical extension of the plume, the magnitude of the induced vertical volume flux of water, and the fraction of oxygen transferred to the dissolved phase. It is therefore important to investigate the sensitivity of these quantities with respect to those input parameters which either can be influenced by the design of the diffusor system or are not well known from field observations. It is not easy to compare different model results for the winter case in a didactically clear way, since, depending on the parameters, the modeled plumes may or may not reach the surface. Therefore the following sensitivity analysis refers only to the summer case, which allows easier comparison (Figure 8). For each calculation, all parameters except the one which is varied correspond to the standard case (Table 6).

Among all the parameters, initial bubble size and initial gas flow have the largest influence on the behavior of the bubble plume, especially on the depth of maximum plume rise (DMPR). If the initial bubble radius is less than 1 mm, the DMPR is about 25–28 m and is nearly independent of bubble size (Figure 8a). For larger bubbles, the DMPR becomes shallower and the plume reaches its highest level for a radius of about 1 cm. The curve (Figure 8a) can be qualitatively explained in terms of the size dependence of the
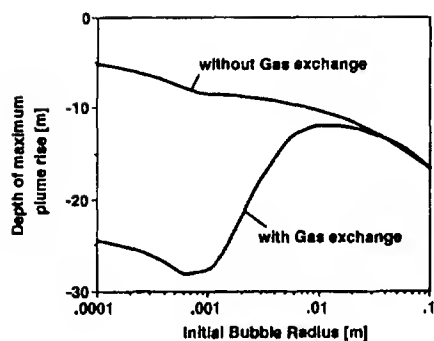
Fig. 9. Maximum plume rise calculated as a function of initial bubble size for the standard situation of July 1983 with and without gas exchange (i.e., dissolution of bubbles). Plume dynamics is strongly dependent on dissolution for bubbles of radius smaller than about 5 mm.

gas exchange and bubble slip velocity alone. Since the gas exchange rate (fractional volume changes per unit time) depends on the surface-to-volume ratio of the bubbles, the oxygen dissolves faster in the lake if the bubbles are small. In addition, smaller bubbles have lower slip velocities and thus a longer contact time with the water before reaching the DMPR.

For bubbles with a radius of less than about 0.7 mm, the exchange rate (fractional volume changes per unit time) is approximately independent of bubble size, since the transfer velocity is proportional to bubble radius, whereas the surface-to-volume ratio is inversely proportional to bubble radius (Table 3b and Figure 3). As a consequence, the smaller and slower the bubbles are, the more buoyancy is generated and the longer the buoyancy lasts. This causes the plume to rise higher. Bubbles with a radius greater than about 0.7 mm have decreasing gas exchange rates per unit volume (since the transfer rate is constant) and constant slip velocities up to a radius of 5 mm. The height of the plume will consequently increase with bubble size. For bubbles with a radius greater than about 10 mm, the height of the plume decreases again since dissolution no longer has any influence (Figure 9). The bubbles rise so rapidly that the buoyancy (proportional to $(w + w_b)^{-1}$) is significantly diminished; the bubbles escape the DMPR and start a new plume (not described by the model).

Because pure oxygen is expensive it is of major importance to operate a lake oxygenation system so as to minimize the amount of oxygen lost by escaping bubbles and to deliver the oxygen as exactly as possible to the required depths. As shown in Figure 8b, for bubbles with a radius of less than 3 mm, more than 99% of the O_2 dissolves. For bubbles with a radius of 3 mm, vertical water circulation reaches a maximum while no O_2 bubbles escape from the hypolimnion. For larger bubbles the total transfer rate decreases rapidly to reach a value of less than 10% for a radius greater than about 3 cm.

The oxygen input rate directly influences the density and thus the buoyancy of the plume. As seen in Figure 8c, an increase in the O_2 input rate from 10^{-3} to 10^{-1} N m^3 s^{-1} causes the DMPR to rise from 45 m to 10 m depth. For large O_2 input rates the DMPR is determined mainly by the position of the thermocline, i.e., the zone of maximum density gradient. If the total oxygen flow rate and the plume

intrusion depth range are prescribed, the model allows the determination of the minimum number of diffusor units needed to reoxygenate at the desired depths. For example, if the oxygen input per diffusor is reduced to 50% (e.g., by doubling the number of diffusors in the lake), the DMPR sinks by 8 m (Figure 8c). Likewise, for artificial mixing with air bubbles, the model can be used to find the optimal bubble size and the minimum airflow rate as a function of the number of diffusors, provided that the ambient stratification and the turnover rate are given.

The initial plume size and initial Froude number (or water velocity), two parameters which are difficult to estimate without additional and complicated field measurements, do not have a significant influence on the DMPR (Figures 8d and 8e). The initial plume size cannot vary more than between about half the diffusor area (10 m^2) and twice this area (40 m^2). The initial plume velocity is expected to correspond approximately to a densimetric Froude number of 1.6, which we choose slightly smaller than the apparent asymptotic value in the near field of 1.7. The low sensitivity of the model calculation with respect to these two parameters means that during oxygenation the properties of the plume are determined mainly by the plume's dynamics and not by the initial conditions.

As mentioned above, the entrainment factor is an empirical constant which has been determined in several laboratory experiments [Milgram, 1983]. A typical value for Gaussian profiles is 0.08, which is equivalent to 0.11 for top hat profiles. Since the entrainment of surrounding water decelerates the water plume, the DMPR depends strongly on this factor (Figure 8f).

Bubble dissolution has a drastic effect on plume dynamics. In Figure 9 the calculated DMPR is shown as a function of initial bubble size with and without gas exchange, respectively. Since small bubbles dissolve faster and have lower slip velocities than large ones, the effect of dissolution on the DMPR is most prominent for small bubbles. For radii larger than about 2 cm, dissolution can be ignored. The result dramatically shows the importance of gas exchange for bubble plume models, if the initial bubble radius is less than about 5 mm, in deep water (65 m depth in this example).

3.3. Artificial Tracer Experiment

On August 22/23, 1983, in collaboration with the Institute of Geography of the University of Bern, a tracer experiment was conducted in Baldeggersee. During a period of 10 min, 1.5 kg of uranin, a fluorescent dye which had previously been dissolved in 200 L of water taken from the lake bottom, was introduced into the plume at a depth of 57 m, just above one of the diffusors, which at this time was releasing 0.0083 N m^3 s^{-1} of O_2. The tracer was pumped from a platform into a hose fixed to the diffusor unit. The temporal evolution of the dye cloud was then measured using an in situ fluorometer operated from the platform.

During the initial phase of the experiment, part of the dye rose up to a depth of 5 m. The average rising velocity was 0.16 m s^{-1} below 40 m depth, and about 0.04 m s^{-1} above this depth (Table 7). After 12 hours, most of the uranin was found between 10 and 23 m depth (Figure 10); a small amount was found below this layer.

Since the parameter to which the model is most sensitive namely, the initial bubble radius r^o, is not very well known,

TABLE 7. Uranin Experiment and Model Calculation, August 1983

	Model*	Field Experiment
Depth of maximum dye rise (above plume), m		5
Depth of maximum plume rise, m	13–11	
Depth of tracer insertion, m		10–23
Equilibrium depth,† m	30–25	
Plume velocity, m/s		
57–40 m depth	0.12–0.13	0.16
40–14 m depth	0.06–0.08	
40–5 m depth		~0.04

*Parameters: initial bubble radius, 2–4 mm; initial plume velocity, 0.15 m/s ($Fr° = 1.6$); oxygen flow, 0.0083 N m^3 s^{-1}; depth of diffusor, 57 m; initial cross-sectional area, 20 m^2; initial plume radius, 2.52 m; ambient profiles, July 1983 (Figure 6).

†Depth to which the plume water sinks back once it has lost all momentum. The model value was calculated by assuming that no entrainment of ambient water into the plume occurs once the plume has reached its highest level. Therefore, the value given represents a maximum value.

a rigorous test of the model is not possible. However, model results are found to agree reasonably well with observation if $r°$ is taken to lie within the range 2–4 mm (Table 7). Based on visual inspection of the bubbles leaving the diffusor tubes and on the fact that ≲1% of the oxygen escaped to the surface, the actual size of $r°$ was estimated to lie within this range. In the lower part of the plume, the observed upward velocity of the dye was close to the modeled plume velocity. In the upper part, the upward velocity of the dye was lower than the modeled plume velocity, and the dye was found to rise to a greater height than that predicted by the model. We presume that small secondary plumes generated by undissolved bubbles remaining after the main plume has stopped rising carried part of the dye up to a depth of 5 m, resulting in a relatively low apparent upward velocity (Table 7). The fact that the tracer was later detected in the lake mainly between the modeled DMPR (11–13 m) and the modeled equilibrium depth (30–25 m) supports this interpretation.

Plume water appears to have mixed with the surrounding water at different rates during the sinking phase. Detailed tests of the model are planned for newer diffusor systems.

4. DISCUSSION

In this section the model is discussed and compared with the results of other investigations in order to explore the range of its validity and to identify open questions.

1. The scientific literature contains just a few experimental data sets which are suitable for comparing model calculations with measurements. The hydrodynamic part of the model was tested by comparing model results with data from the Bugg Spring experiment of Milgram [1983]. In this experiment air was injected at 50 m depth through a nozzle of comparatively small area (about 10^{-2} m^2) into a nonstratified system. The model was run with entrainment factors $\alpha_{th} = 0.116$ determined from the observed value α_g and adapted to the top hat distribution by putting $\alpha_{th} = \sqrt{2}\alpha_g$. Calculated and observed values for volume flux, plume radius and plume velocity agreed within 10% everywhere within the vertical profile. The model calculations are also close to the proportionality between plume water volume flux μ and the square root of the airflow rate observed by Leitch and Baines [1989]. Since bubble dissolution was not important in their experiment, the bubble solution dynamics was tested by comparison with the experiments of Motarjemi and Jameson [1978] in which bubbles of different sizes were released at 10 m depth. Calculated and observed dissolution rates were equal to within a few percent.

2. In this model we do not distinguish between the zone of flow establishment and the zone of the fully developed plume. We also neglect the initial adjustment of the bubble slip velocity just above the diffusor. We try to reduce this insufficiency of the model by choosing appropriate initial plume velocities. There are physical arguments for reducing the range of the initial Froude number $Fr°$. As displayed in Figure 11 for the case of an unstratified water column, the Froude number (equation (23)) approaches a maximum value of $Fr \approx 1.7$ at about 15–25 m above the diffusor for all initial Froude numbers less than 1.7. In fact, any initial value of $Fr°$

Distance from Diffusor [m]
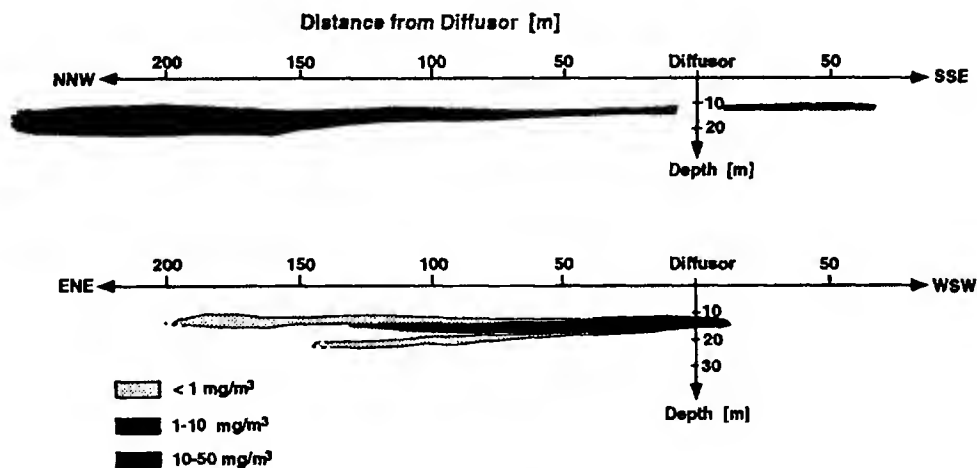

▨ < 1 mg/m³
■ 1-10 mg/m³
■ 10-50 mg/m³

Fig. 10. Distribution of uranin in Baldeggersee 12 hours after injection into the bubble plume just above the diffusor at 57 m depth. The two diagrams show tracer concentration along two mutually perpendicular transects. Most of the uranin is dispersed between 10 m and 23 m depth. (Courtesy of Naturaqua, Bern, Switzerland.)
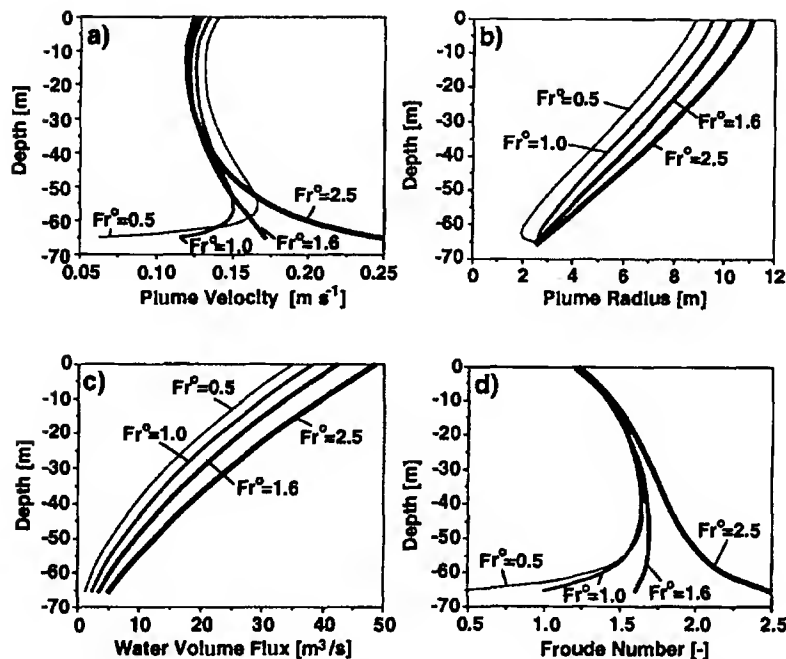
Fig. 11. Plume velocity and radius, volume flux and local Froude number Fr as functions of depth in unstratified water calculated with standard parameters for artificial mixing (Table 6) for various initial Froude numbers Fr° (Fr° labeled on curves). Note the contraction and acceleration of the plume for $Fr^\circ < 1.0$ and the asymptotic behavior of Fr for $Fr^\circ < 1.7$.

> 1.7 is unrealistic because the plume would have to undergo a decrease in velocity immediately above the diffusor (just where bubbles enter the flow), as can be seen in Figure 11a for the case $Fr^\circ = 2.5$. For $Fr^\circ < 1.5$ the plume is accelerated immediately above the diffusor, as demonstrated in Figure 11a for the case $Fr^\circ = 1.0$. For $Fr^\circ \gtrsim 1.0$ the plume initially undergoes contraction as it rises (Figure 11b). This contraction becomes more pronounced as Fr° decreases to 0.5. Because a slight contraction can be observed in tank experiments [Müller et al., 1987], we regard values of 0.75–1.0 as a reasonable lower bound for Fr°.

The initial Froude number Fr° depends most likely on the geometry of the diffusor source, since for the zone of flow establishment it is relevant whether the water can flow upward through the diffusor area (open source, diffusor above the bed) or whether the water has to flow horizontally to the rising plume (closed source, diffusor resting on the bed). It seems likely that in the latter case the initial Froude number Fr° will be smaller. Because the slight contraction which was observed in tank experiments occurred for a closed source [Müller et al., 1987] and because the lake restoration diffusor unit with widely spaced tubes represents an open source, we conclude that the initial Froude number for the latter lies between 1.0 and 1.7.

3. We assumed top hat distributions for all plume properties. Mathematically, the scaling involved here is nearly equivalent to that inherent in the horizontally integrated model, presented by Ditmars and Cederwall [1974]. It simplifies the model, but does not restrict its dynamic generality, as long as the profiles (of velocity and buoyancy) remain similar at all heights. We introduced λ, the ratio of the inner plume radius (containing the bubbles) to the velocity radius, as the only plume geometry parameter. However, as long as

the water velocities in the bubble core and the outer annulus are equal, the model is independent of λ, as is evident from (16). We retained λ in this model, however, in order to obtain the correct equations for O_2 and N_2 if the double plume model [McDougall, 1978] is used.

4. In the case of strong stratification, single-phase plume models do not adequately describe the plume if the bubbles are not completely dissolved at the predicted depth of maximum plume rise. Bubble plume experiments carried out by McDougall [1978] in a stratified tank showed that fluid from the outer annulus can leave the plume at levels of neutral buoyancy and spread out horizontally, while the center of the plume, where all the bubbles are concentrated, continues to rise. The present model disregards the double plume structure, the detrainment, and the development of secondary plumes initiated by the remaining bubbles. Secondary plumes are created when oxygenation is carried out with relatively large bubbles which are not yet dissolved at DMPR, or in the case of artificial mixing, when the airflow rate is not large enough to bring the entire plume to the surface. For such situations, the model presented here loses its validity as soon as the water has lost its vertical momentum. However, oxygen input with adequately small bubbles which disappear completely (Figures 7c and 7e) will not generate secondary plumes. The price for using the double plume model is the addition of a further two entrainment factors.

5. The entrainment coefficient α is not a constant for all plumes. A simple parameterization is not obvious. In our model for the standard case $\alpha_{th} = \sqrt{2}\alpha_g = 0.11$ was used, corresponding to $\alpha_g = 0.08$ as given by Fischer et al. [1979]. Milgram [1983] calculated α for bubble plumes of various scales based on data from several authors and correlated

these values with a "bubble Froude number F_B" defined by local plume properties. *Milgram*'s [1983] values for α_{th} averaged 0.081 and 0.12 for airflow rates of 0.024 and 0.118 N m^3 s^{-1}, respectively, for the 50-m-deep Bugg Spring experiment. *Fannelop and Sjoen* [1980] observed values of α_{th} from 0.10 to 0.14, increasing with airflow rates in the range 0.005–0.022 N m^3 s^{-1}.

6. In the conservation equations used here, vertical turbulent flux terms (such as $w'c'$) are neglected compared to fluxes based on mean properties, presuming that the former are small compared to the latter. This assumption is equivalent to a momentum amplification factor of $\gamma = 1$ [*Milgram*, 1983]. The analysis of *Milgram* [1983, Table 1] yielded values of $\gamma = 1.0$–1.1 for typical oxygenation gas rates and $\gamma = 1.1$–1.26 for gas rates appropriate to artificial mixing. The corresponding overestimation of the momentum gain would consequently be not more than 21%. However, *Milgram* [1983] has shown that for plumes with low bubble density, γ can increase dramatically.

7. There are many questions concerning bubble plumes still remaining open which will have to be addressed in tank and field experiments. Apart from the problems raised in the discussion above, we would like to mention the question of how bubble size affects bubble dynamics [*Müller et al.*, 1987], the problem of continuous detrainment and problems related to the interaction of the plume with the ambient flow field in the lake (cross flow, plume wandering). Some of these questions are being investigated in the new bubble-plume tank of the Swiss Federal Institute of Technology [*Müller et al.*, 1987]. We think that the mathematical model presented here provides a useful framework for further investigations and helps to relate laboratory experiments to field situations when bubble dissolution and expansion are important.

5. SUMMARY AND CONCLUSIONS

1. A steady, horizontally averaged plume model was developed based on the entrainment hypothesis, variable buoyancy determined by ambient profiles and actual plume properties, and processes of bubble gas exchange and decompression. The model was applied to a stratified lake for a diffusor system with a large open source and low gas flow rates (of the order of 5×10^{-4} N m^3 s^{-1} m^{-2}). Model calculations were in encouraging agreement with experimental data.

2. Gas exchange, decompression and bubble slip velocity affect both bubble volume and bubble residence time. Consequently, buoyancy flux is a complex function of height. For small bubbles, gas exchange determines plume dynamics to a large extent.

3. Apart from the initial bubble size, the gas flow rate and entrainment coefficient are the parameters to which the model is most sensitive. The sensitivity to diffusor size and initial velocity turned out to be small, provided the initial velocity was chosen below an upper bound. We argue that a reasonable range of the initial velocity is given by the condition $1 < Fr° < 1.7$ for an open source (diffuser situated above the bottom), and $Fr° < 1$ for a closed source (diffusor resting on the bottom).

4. Model calculations clearly define two modes of diffusor operation: oxygenation (or aeration) and artificial mixing. Optimal bubble size depends crucially on the objectives

and on the radius-dependent parameters mass transfer and slip velocity. In order to prevent oxygen loss by escaping bubbles and to achieve insertion into the deepest layers for oxygenation, bubbles of radius $\lesssim 1$ mm are the best choice (here about 0.8 mm). In contrast, artificial mixing is most efficient for an initial bubble radius of about 1 cm.

5. Given the operational goals, the model helps to optimize system design in order to conduct the internal restoration of a lake as economically as possible.

6. The model can be used as a tool to design lake aeration systems and evaluate sensitivity to operation parameters. It can also help in transferring laboratory results to the field. Finally, it serves to define areas where additional research is needed.

REFERENCES

Asaeda, T., and J. Imberger, Structures of bubble plumes in stratified environments, *Environ. Dyn. Rep. ED-88-250*, Univ. of West. Aust., Nedlands, 1988.

Bucksteeg, K., and F. Hollfelder, Versuche zur Bestimmung der Leistungsfähigkeit eines Gerätes zur Tiefenwasserbelüftung, *GWF Gas Wasserfach Wasser Abwasser, 119*, 65–72, 1978.

Bührer, H., and H. Ambühl, Die Einleitung von gereinigtem Abwasser in Seen, *Schweiz. Z. Hydrol., 37*, 347–369, 1975.

Ditmars, J. D., and K. Cederwall, Analysis of air-bubble plumes, in *Proceedings, 14th Coastal Engineering Conference, Copenhagen,* chap. 128, pp. 2209–2226, American Society of Civil Engineers, New York, 1974.

Durst, F., B. Schoenung, K. Selanger, and M. Winter, Bubble-driven liquid flows, *J. Fluid Mech., 170*, 53–82, 1986.

Fannelop, T. K., and K. Sjoen, Hydrodynamics of underwater blowouts, *Norw. Marit. Res.*, no. 4, 17–32, 1980.

Fast, A. W., and R. G. Hulquist, Supersaturation of nitrogen gas caused by artificial aeration in reservoirs, *Tech. Rep. E-82-9*, U.S. Army Eng. Waterways Exp. Sta., Vicksburg, Miss., 1982.

Fischer, H. B., E. J. List, R. C. Y. Koh, J. Imberger, and N. H. Brooks, *Mixing in Inland and Coastal Waters*, Academic Press, San Diego, Calif., 1979.

Goossens, L. H. J., *Reservoir Destratification With Bubble Columns*, Delft University Press, Delft, Netherlands, 1979.

Haberman, W. L., and R. K. Morton, An experimental study of bubbles moving in liquids, *Proc. Am. Soc. Civ. Eng., 80*, 379–427, 1954.

Hussian, N. A., and B. S. Narang, Simplified analysis of air bubble plumes in moderately stratified environments, *J. Heat Transfer, 106*, 543–551, 1983.

Imboden, D. M., Restoration of a Swiss lake by internal measures: Can models explain reality? in *Lake Pollution and Recovery. Proceedings,* pp. 91–102, European Water Pollution Control Association, Rome, 1985.

Joller, T., Untersuchung vertikaler Mischungsprozesse mit chemisch physikalischen Tracern im Hypolimnion des eutrophen Baldeggersees, *Dissertation 7830*, 94 pp., Eidgenöss. Tech. Hochsch., Zurich, Switzerland, 1985.

Kobus, H., Bemessungsgrundlagen und Anwendungen für Luftschleier im Wasserbau, *Wasser Abwasser Forsch. Prax., 7*, 168 pp., 1973.

Leitch, A. M., and W. D. Baines, Liquid volume flux in a weak bubble plume, *J. Fluid Mech., 205*, 77–98, 1989.

Marshall, T., *Gas Encyclopaedia*, p. 1150, Elsevier, New York, 1976.

McDougall, T. J., Bubble plumes in stratified environments, *J. Fluid Mech., 85*, 655–672, 1978.

Milgram, J. H., Mean flow in round bubble plumes, *J. Fluid Mech., 133*, 345–376, 1983.

Milgram, J. H., and R. J. Van Houten, Plumes from sub-sea well blowouts, in *Proceedings of the Third International Conference on Behaviour of Off-Shore Structures*, edited by C. Chryssostomidis and J. J. Connor, pp. 659–684, Hemisphere, New York, 1982.

Morton, B. R., Forced plumes, *J. Fluid Mech.*, 5, 151–163, 1959.

Morton, B. R., G. I. Taylor, and J. S. Turner, Turbulent gravitational convection from maintained and instantaneous sources, *Proc. R. Soc. London, Ser. A, 234*, 1–23, 1956.

Motarjemi, M., and G. J. Jameson, Mass transfer from very small bubbles—The optimum bubble size for aeration, *Chem. Eng. Sci., 33*, 1415–1423, 1978.

Müller, A., E. Grass, A. Wüest, and A. Gyr, Modelling of bubble plumes, paper presented at XXII Congress, Int. Assoc. for Hydraul. Res., Lausanne, Switzerland, 1987.

Patterson, J. C., and J. Imberger, Simulation of bubble plume destratification systems in reservoirs, *Aquatic Sci., 51*, 3–18, 1989.

Rast, W., and G. F. Lee, Nutrient loading: Estimates for lakes, *J. Environ. Eng. N. Y., 109*, 502–512, 1983.

Stadelmann, P., Zustand des Sempachersees, *Wasser Energie Luft, 80*, 81–96, 1988.

Stöckli, A., and M. Schmid, Die Sanierung des Hallwilersees, *Wasser Energie Luft, 79*, 143–149, 1987.

Topham, D. R., Hydrodynamics of an oil well blowout, *Beaufort Sea Tech. Rep. 33*, Inst. of Ocean Sci., Sidney, B. C., 1975.

Zic, K., and H. G. Stefan, Analysis and simulation of mixing of stratified lakes or reservoirs by air bubble plumes, *Proj. Rep. 305*, St. Anthony Falls Hydraul. Lab., Univ. of Minn., Minneapolis, 1990.

N. H. Brooks, W. M. Keck Laboratory of Hydraulics and Water Resources, California Institute of Technology, Pasadena, CA 91125.

D. M. Imboden and A. Wüest, Institute for Aquatic Sciences and Water Pollution Control, EAWAG, CH-8600 Dübendorf, Switzerland.

Exhibit C

HYPOLIMNETIC OXYGENATION: COUPLING BUBBLE-PLUME AND RESERVOIR MODELS

D. F. McGinnis[1], J. C. Little[1] and A. Wüest[2]

[1]*Department of Civil & Environmental Engineering, Virginia Polytechnic Institute and State University, Blacksburg, Virginia 24061-0246, USA*

[2]*Applied Aquatic Ecology, Federal Institute for Environmental Science and Technology (EAWAG), Kastanienbaum, CH-6047, Switzerland*

ABSTRACT

Stratification of reservoirs may result in hypolimnetic oxygen depletion with negative consequences for water quality in hydropower reservoirs, water supply reservoirs, and cold-water fisheries. Although bubble plumes are used to add oxygen to the hypolimnion without significantly disrupting the thermal density structure, they nevertheless introduce energy, which causes mixing. The induced mixing changes the vertical density gradient, and hence the operation of the plume. To account for this effect, a bubble-plume model was coupled in a preliminary fashion with a hydrodynamic reservoir model and then used to predict operational data obtained from Spring Hollow Reservoir in Virginia, USA. The coupled model was able to accurately predict the extent of hypolimnetic warming. Although oxygen consumption was turned off in the reservoir model, the predictions followed the form of the observed oxygen concentration profiles quite closely.

KEYWORDS

Aeration; bubble plume; hypolimnion; mixing, oxygen transfer; reservoir

NOMENCLATURE

C	dissolved concentration, $mol\ m^{-3}$.
E	entrainment, $m^2\ s^{-1}$.
F_D	dissolved species flux, $mol\ s^{-1}$.
F_G	gaseous species flux, $mol\ s^{-1}$.
F_S	salinity flux, $g\ s^{-1}$.
F_T	temperature flux, $^\circ C\ m^3\ s^{-1}$.
g	gravitational acceleration, $m\ s^{-2}$.
H	Henry's coefficient, $mol\ m^{-3}\ bar^{-1}$.
K_L	mass transfer coefficient, $m\ s^{-1}$.
L	plume length, m.
M	water momentum, $m^4\ s^{-2}$.
N	number flux of bubbles, s^{-1}.
P	pressure, bar.
Q	plume flow rate, $m^3\ s^{-1}$.
r	bubble radius, m.
S	salinity, $g\ kg^{-1}$.
T	temperature, $^\circ C$.

v	velocity, m s^{-1}.
W	plume width, m.
y	gaseous concentration, mol m^3.
z	depth, m.

Greek letters

α	entrainment coefficient, -.
λ	spreading coefficient, -.
ρ	density, kg m^{-3}.

Subscripts

a	ambient water
b	bubble
i	gas species, oxygen or nitrogen
p	plume water and gas mixture
w	plume water

INTRODUCTION

Thermal stratification of lakes and reservoirs can result in substantial hypolimnetic oxygen depletion, which may have a negative impact on cold-water fisheries, the drinking-water treatment process, and water quality downstream of hydropower reservoirs (Little and McGinnis, 2000). One solution to these problems is to install bubble-plume diffusers that replenish hypolimnetic oxygen without destratifying the reservoir (Wüest et al., 1992). While bubble plumes are successful at adding oxygen, the added energy will induce some degree of mixing in the hypolimnion, depending on the design and operational characteristics. The impact of the induced mixing needs to be considered when these systems are designed. For example, partial erosion of the thermocline and warming of the hypolimnion may cause premature destratification of the reservoir. Higher temperatures and plume induced mixing may also be responsible for an increase in hypolimnetic oxygen demand (Little and McGinnis, 2000). Finally, while plume operation changes the thermal structure of the reservoir, the performance of the bubble plume itself depends strongly on the vertical density gradient. This complex interaction between plume and reservoir needs to be taken into account in the design and operation of bubble plumes. In this paper, a preliminary attempt is made to account for this interaction by coupling a model that predicts the performance of a bubble plume with a hydrodynamic reservoir model.

Application of coupled model

The coupled model was tested using data collected from Spring Hollow Reservoir (SHR) located in Roanoke County, Virginia, USA. Spring Hollow is a side-storage reservoir with an existing bubble-plume diffuser that uses air as the source of oxygen (Little and McGinnis, 2000). SHR tends to be mesotrophic and experiences low dissolved oxygen towards the end of the stratified period. Therefore, it is only necessary to operate the diffuser for a period of several weeks in the late summer. Table 1 provides design and operational characteristics. Figures 1 and 2 show temperature and oxygen profiles, beginning on Sep 28 immediately before diffuser start-up. During continuous operation of the diffuser, data were collected on Sep 30, Oct 2, Oct 5, and Oct 9. The diffuser was shut down on Oct 13, but unfortunately no data were collected on that day. Although the diffuser successfully adds oxygen, it is clear that it also causes gentle mixing of the hypolimnion, which in turn causes some warming of the hypolimnetic water. Following shut down, additional data were collected on Oct 21 and Oct 28, showing no further warming of the hypolimnion, but continued depletion of dissolved oxygen. The coupled model should be able to predict

the observed rate of oxygen addition as well as the extent of thermocline erosion and hypolimnetic warming.

Table 1. Operating conditions for bubble-plume diffuser in Spring Hollow Reservoir.

Parameter	Value
Maximum depth [m]	55
Surface area [10^6 m^2]	0.4
Total water volume [10^6 m^3]	7.2
Active diffuser length [m]	360
Average diffuser depth [m]	43
Air flow rate [Nm^3 h^{-1}]*	43

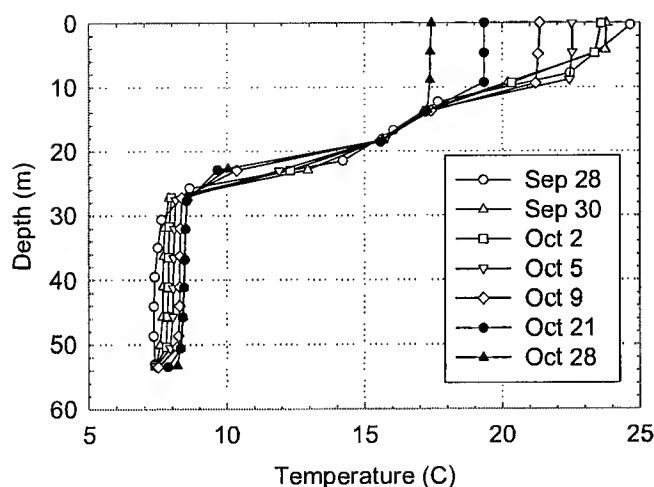*1 Nm^3 denotes 1 m^3 of gas at 1 bar and 0 °C

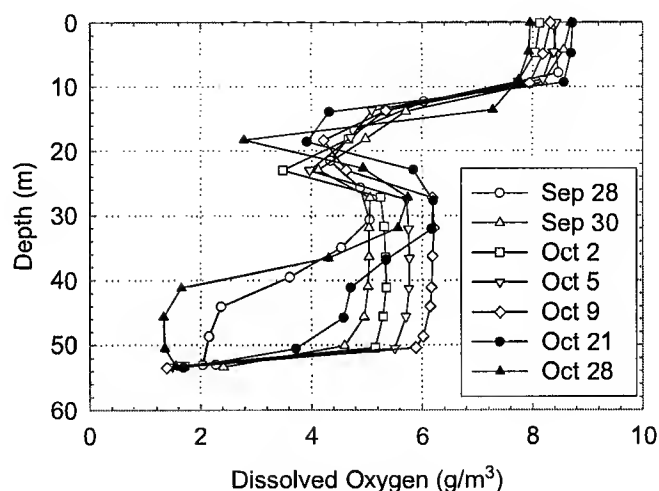Figure 1. Observed temperature profiles in Spring Hollow Reservoir.

Figure 2. Observed oxygen profiles in Spring Hollow Reservoir.

Plume model

A model for predicting the performance of circular bubble plumes has been developed by Wüest et al. (1992). Based on eight flux equations that are solved simultaneously, the model predicts water flow rate, oxygen transfer and plume rise height, given the diffuser depth, applied gas flow rate, initial bubble size, and diffuser geometry (Wüest et al., 1992). A key contribution of this work was the use of a variable buoyancy flux to account for gas dissolution as well as decompression. This is especially important when pure oxygen is used because the rate of dissolution is very high. The diffuser installed in Spring Hollow Reservoir is linear and the eight model equations (Table 2 and 3) were modified to conform to linear, as opposed to circular, geometry. The entrainment coefficient, α, was set at 0.08 and the spreading coefficient, λ, was 0.85, as reported by Fannelop et al. (1991) for linear plumes. The computational procedure and other details are the same as for the circular plume model (Wüest et al., 1992). Although the linear plume model has not been fully calibrated, the performance was checked by comparing predictions based on a square diffuser with those predicted for a circular diffuser of equal area. Similar results were obtained.

Table 2. Key model variables.

Variable	Formula	Units
Entrainment	$E = 2(L + W)\alpha v$	$m^2 s^{-1}$
Plume Water Volume Flux	$Q = LWv$	$m^3 s^{-1}$
Momentum Flux	$M = LWv^2$	$m^4 s^{-2}$
Temperature Flux	$F_T = QT_p$	$^{\circ}C\ m^3 s^{-1}$
Dissolved Solids Flux	$F_s = QS\rho_w$	$g\ s^{-1}$
Dissolved O_2 and N_2 Fluxes	$F_{D_i} = QC_i$	$mol\ s^{-1}$
Gaseous O_2 and N_2 Fluxes	$F_{G_i} = LW\lambda^2(v + v_b)y_i$	$mol\ s^{-1}$

Table 3. Non-linear differential flux equations.

Water Volume Flux	$\dfrac{dQ}{dz} = E$
Momentum Flux	$\dfrac{dM}{dz} = \dfrac{\rho_a - \rho_p}{\rho_p} gLW\lambda^2 + \dfrac{\rho_a - \rho_w}{\rho_p} gLW(1 - \lambda^2)$
Temperature Flux	$\dfrac{dF_T}{dz} = ET_a$
Salinity Flux	$\dfrac{dF_s}{dz} = E\rho_a S_a$
Dissolved Gas Flux	$\dfrac{dF_{Di}}{dz} = EC_i + \dfrac{4\pi r^2 N}{v + v_b} K_L(H_i P_i - C_i)$
Gas Flux	$\dfrac{dF_{Gi}}{dz} = \dfrac{4\pi r^2 N}{v + v_b} K_L(H_i P_i - C_i)$

Reservoir model

CE-QUAL-W2 (W2) is a two-dimensional, laterally averaged, hydrodynamic and water quality model (USACE, 1995). W2 includes horizontal, but not vertical, momentum, and accounts for momentum transfer from influent streams and the associated shear stress imparted to the surrounding water. W2 was applied to SHR for the year 1998 when the aeration system was operated. A temperature calibration was performed adjusting only the wind-sheltering coefficient. Based on the model calibration, no significant warming is expected to occur in the hypolimnion if the diffuser is not in operation. W2 was then set up to run during the aeration period. During diffuser operation there was no inflow into the reservoir and the only outflow was seepage loss and water supplied to the water treatment plant. For simplicity, all dissolved oxygen (DO) sinks were turned off, with DO treated as a conservative tracer.

Coupled plume and reservoir model

The location of the 360-m long diffuser changes in elevation with its deepest point being closest to the dam wall. Therefore, as shown in Figure 3, it is represented in W2 as 5 discrete segments in consecutive columns. For the purpose of coupling, the plume model is used to compute the flow rate of ambient water entrained as the plume rises, and the flow rate, temperature, and oxygen concentration of the water that is detrained upon reaching the depth of maximum plume rise. In other words, entrainment removes water of known temperature and oxygen concentration from a range of depths, while detrainment returns the sum of all the entrained water at the specified discharge location after adding the predicted amount of oxygen. As shown in Figure 3, this plume action is simulated within W2 by withdrawing water from the "entrainment"

cells (marked with X in Figure 3) and discharging it at the "detrainment" cell (marked with O in Figure 3). Because of the changing temperature gradient during the course of the simulation, the plume rise height also changes. It was therefore necessary in some cases to specify a new detrainment cell during the course of the simulation, as indicated in Figure 3.
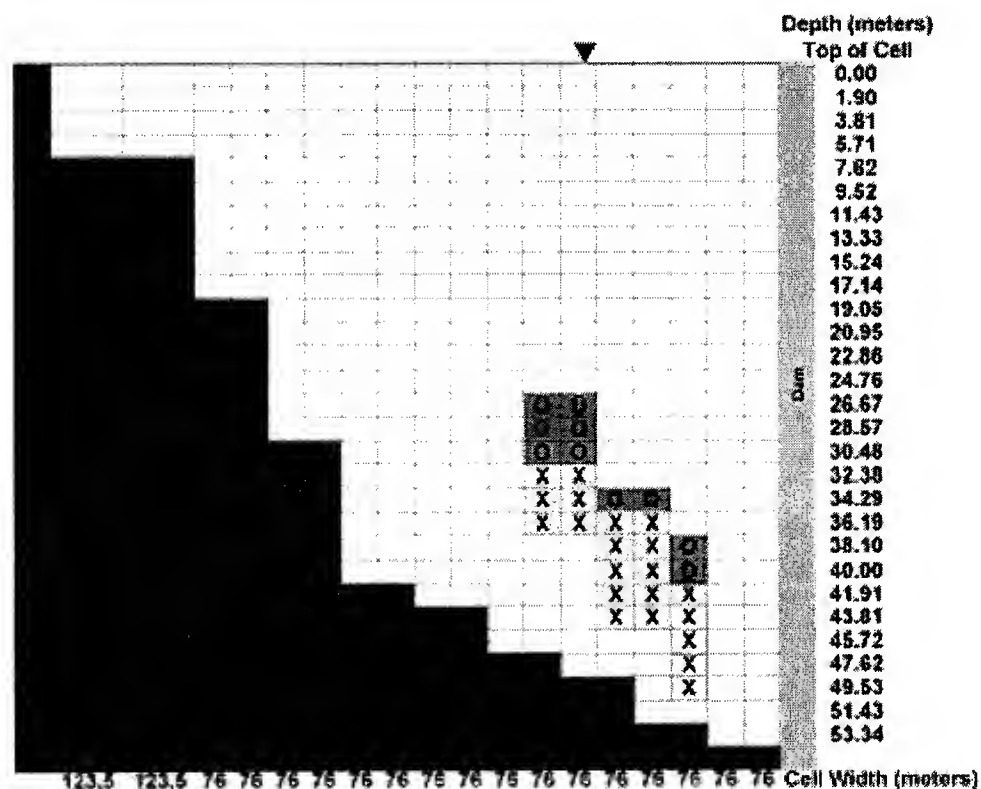

Figure 3. Reservoir grid section for CE-QUAL-W2.

Although the reservoir is laterally averaged, the entrainment operation is adequately represented using a simple withdrawal. However, the entire plume discharge is mixed into the detrainment cell. Because the theoretical plume width at the point of detrainment approaches infinity, this instantaneous mixing appears reasonable to a first approximation. However, the selection of detrainment cell size might be an important consideration when the coupling procedure is refined.

The "manual" coupling procedure was handled as follows. First, the initial reservoir conditions on Sep. 28 were used in the plume model to obtain the flow rate of entrained and detrained water. This procedure was performed for each of the 5 diffuser segments shown in Figure 3. Then, starting on Sep. 28 at 12h00, and using the 5 sets of predicted data, the coupled plume/W2 model was run for 6 hours. The predicted ambient temperature and DO profiles obtained at the end of this 6-hour period were then used as input to the plume model to generate a new set of predicted plume entrainment and detrainment data for each of the 5 plume segments. The entire procedure was repeated until Oct. 9 at 12h00.

RESULTS AND DISCUSSION

The results of the preliminary coupling procedure are shown in Figures 4 and 5. Excluding the water below the diffuser, Figure 4 shows that the coupled model predicts mixing and warming induced by plume operation quite accurately. The thermocline is eroded during the entire period of operation, even though the plume only partially penetrates the thermocline during the first day of simulation at the 2 highest diffuser segments shown in Figure 3. Thereafter, the plume stops between 1 and 3 meters below the thermocline. The results suggest that the flow of detrained water causes sufficient mixing near the thermocline to result in almost exactly the right amount of warming in the hypolimnion. Factors causing

mixing include vertical dispersion of horizontal momentum, momentum transfer from the detraining plume water, and horizontally generated shear. A more thorough investigation into the dominant mixing mechanisms is required.

Although all oxygen sinks are turned off in the W2 model, Figure 5 shows that the coupled model predicts the evolution of hypolimnetic DO fairly well. Once the effects of sediment and other oxygen demands are correctly incorporated in W2, the predicted oxygen concentrations will not increase as rapidly. However, as currently represented, the plume model under-predicts the rate of oxygen addition because oxygen transfer ceases when the plume detrains. Bubbles are still present in the hypolimnion and will continue to rise through the water column. In effect, this produces a weaker secondary plume that results in some additional mixing and oxygen transfer in the hypolimnion, as well as at higher locations in the reservoir. The effects of the secondary plume will be investigated, and if significant relative to the primary plume, will be incorporated in the coupled model.
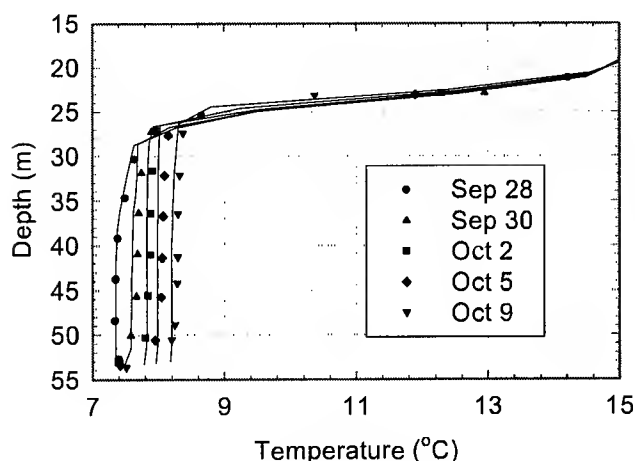
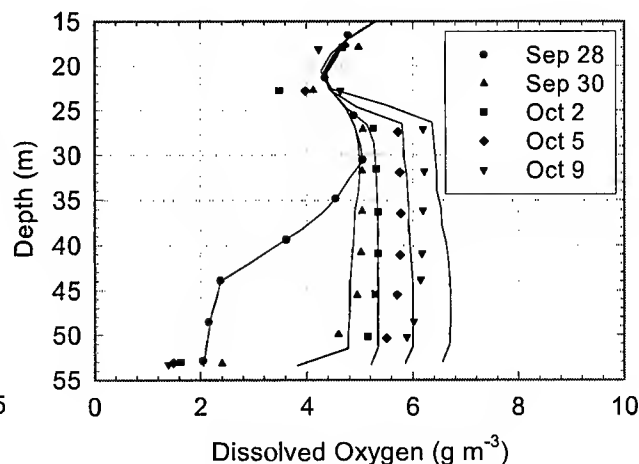Figure 4. Observed versus predicted hypolimnetic temperature.

Figure 5. Observed versus predicted hypolimnetic DO.

FUTURE WORK

While the preliminary results are very encouraging, the iterative "manual" coupling procedure is time consuming. The plume model will therefore be incorporated as a subroutine in W2 so that the computation can be done automatically. Further testing of the coupled model will be carried out on new data collected at SHR in Virginia as well as at Lake Baldegg in Switzerland. Ultimately, the coupled model could also be used to improve the calibration of the plume model.

REFERENCES

Cole T.M. and Buchak E.M. (1995). CE-QUAL-W2: A two-dimensional, laterally averaged, Hydrodynamic and Water Quality Model, Version 2.0. Instruction Report EL-95-. US Army Engineering Waterways Experiment Station, Vicksburg, MS.

Fannelop T.K., Hirschberg S. and Kuffer J. (1991). Surface Current and Recirculating Cells Generated by Bubble Curtains and Jets. *Journal of Fluid Mechanics, 229*, 629-657.

Little J.C. and McGinnis D.F. (2000). Hypolimnetic Oxygenation: Predicting Performance using a Discrete-Bubble Model. *Proceedings of 1st World Water Congress, International Water Association (IWA)*, Paris, France, July 3-7.

Wüest A., Brooks N.H. and Imboden D.M. (1992). Bubble plume modeling for lake restoration. *Wat. Resour. Res.*, **28**, 3235-3250.

Exhibit D

Linear bubble plume model for hypolimnetic oxygenation: Full-scale validation and sensitivity analysis

V. L. Singleton,[1] P. Gantzer,[1] and J. C. Little[1]

[1] An existing linear bubble plume model was improved, and data collected from a full-scale diffuser installed in Spring Hollow Reservoir, Virginia, were used to validate the model. The depth of maximum plume rise was simulated well for two of the three diffuser tests. Temperature predictions deviated from measured profiles near the maximum plume rise height, but predicted dissolved oxygen profiles compared very well with observations. A sensitivity analysis was performed. The gas flow rate had the greatest effect on predicted plume rise height and induced water flow rate, both of which were directly proportional to gas flow rate. Oxygen transfer within the hypolimnion was independent of all parameters except initial bubble radius and was inversely proportional for radii greater than approximately 1 mm. The results of this work suggest that plume dynamics and oxygen transfer can successfully be predicted for linear bubble plumes using the discrete-bubble approach.

1. Introduction

[2] Bubble plumes are used in a variety of industrial and environmental applications including mixing in chemical reactors, stripping of dissolved gases, containment of spills, prevention of ice formation, protection of harbors from damaging waves [*Fanneløp et al.*, 1991], and destratification of lakes and reservoirs [*Schladow*, 1992]. In addition to airlift aerators [*Burris et al.*, 2002] and Speece cones [*McGinnis and Little*, 1998], bubble plumes are commonly used for hypolimnetic aeration and oxygenation, which preserves stratification of water bodies while adding oxygen to the deepest layer. Hypolimnetic anoxia negatively affects the drinking water treatment process, cold-water fisheries, and water quality downstream of hydropower reservoirs. In the United States, releases from hydropower reservoirs typically must comply with state water quality criteria for minimum dissolved oxygen (DO) concentrations [*Peterson et al.*, 2003]. Oxygen depletion may lead to increases in hydrogen sulfide, ammonia, and phosphorus and the release of reduced iron and manganese from the sediments. Hydrogen sulfide, iron, and manganese in drinking water usually require additional treatment [*Cooke and Carlson*, 1989]. Finally, hypoxia can affect sex differentiation and development in fish, resulting in male-dominated populations with reduced reproductive success [*Shang et al.*, 2006].

[3] A bubble plume model to predict oxygen transfer from linear diffuser systems was presented by *McGinnis et al.* [2001], based on the model for a circular diffuser developed earlier by *Wüest et al.* [1992]. While several models for point-source or circular bubble plumes have been proposed [*Asaeda and Imberger*, 1993; *Brevik and Kluge*, 1999; *Ditmars and Cederwall*, 1974; *Fanneløp and Sjøen*, 1980; *Johansen*, 2000; *Kobus*, 1968; *McDougall*, 1978; *Milgram*, 1983; *Rayyan and Speece*, 1977; *Sahoo and Luketina*, 2003; *Schladow*, 1992; *Wüest et al.*, 1992; *Zheng et al.*, 2002], less work has been conducted on linear (also referred to as line, two-dimensional, or planar) bubble plumes. *Kobus* [1968] developed one of the first analytical models for linear bubble plumes, which uses an empirical correlation to calculate buoyancy flux. *Ditmars and Cederwall* [1974] presented a model similar to that of *Kobus* [1968] but included bubble slip velocity. *Brevik* [1977] proposed a phenomenological theory for two-dimensional bubble plumes comparable with that of *Ditmars and Cederwall* [1974], except that kinetic energy was used to predict entrainment. *Wilkinson* [1979] proposed that full-scale linear plumes could be characterized by a Weber number. *Laureshen and Rowe* [1987] presented a model for two-dimensional bubble plumes in which plume spreading, entrainment, and momentum amplification were assumed to be functions of the plume Weber number and empirical constants. *Fanneløp et al.* [1991] developed a model for linear plumes in shallow water and studied the resulting surface currents and recirculation cells. Last, *Brevik and Kluge* [1999] expanded an existing model for linear bubble plumes to account for vertical turbulence. Although much insight into plume dynamics was gained, none of these models for linear or two-dimensional bubble plumes accounted for ambient stratification or gas transfer. The first linear bubble plume model to include gas transfer was presented by *McGinnis et al.* [2001], who converted the circular bubble plume model of *Wüest et al.* [1992] to linear geometry. The incorporation of gas transfer is critical because the rapid dissolution rate of oxygen, and nitrogen

[1]Department of Civil and Environmental Engineering, Virginia Polytechnic Institute and State University, Blacksburg, Virginia, USA.

when compressed air is used, strongly influences the buoyancy of the plume [*Wüest et al.*, 1992]. Gas transfer is especially important in deep water bodies and for weak plumes because the increased contact time allows greater gas exchange. Last, the prediction of oxygen addition from hypolimnetic oxygenation systems is facilitated. Despite the usefulness of the linear bubble plume model, it has not yet been validated at full scale and over a range of operating conditions.

[4] Using extensive, high-spatial-resolution conductivity and temperature as a function of depth (CTD) transect data collected in Spring Hollow Reservoir (SHR), Virginia, during diffuser operation in 2003 and 2004, the performance of the linear bubble plume model is evaluated. The motivation for this work includes verification of model performance prior to use for design and investigation of critical model parameters through sensitivity analysis. Also, the accuracy of model predictions for depth of maximum plume rise (DMPR) and induced water flow rate should be assessed prior to coupling with lake/reservoir hydrodynamic and water quality models, such as CE-QUAL-W2 [*McGinnis et al.*, 2001]. In this paper an improved linear bubble plume model is presented, observations and model predictions are compared, and results of a sensitivity analysis are discussed.

2. Bubble Plumes in Stratified Water Bodies

[5] During hypolimnetic oxygenation with bubble plumes, compressed gas is continually supplied to diffusers, usually located immediately above the sediments, and is allowed to bubble freely. A gas-water plume mixture that is less dense than the ambient water is created, which causes the mixture to ascend through the hypolimnion. As the mixture rises, ambient water is entrained into the plume, and the plume width increases. The entrained fluid produces a double-plume structure, consisting of an inner core that contains the bubble-water mixture surrounded by an outer annulus that contains plume water relatively free of bubbles [*McDougall*, 1978]. As the outer annulus entrains stratified hypolimnetic water, the plume width increases and the density decreases. When the negative buoyancy of the entrained fluid exceeds the positive buoyancy imparted by the bubbles, the plume detrains water at a rate nearly equal to that previously entrained [*Lemckert and Imberger*, 1993]. At this depth, the velocity of the relatively dense water within the plume decreases to zero, and the plume stops rising. The detraining plume water then forms an annular downward flow immediately outside the outer annulus of the upward flowing plume water. The detraining plume water entrains ambient water until a depth of neutral buoyancy is reached, where a horizontal intrusion is created into the hypolimnion [*Asaeda and Imberger*, 1993]. The undissolved bubbles remaining in the bubble-water mixture separate from the inner core flow and continue to rise to the surface, repeating the entire process.

3. Linear Bubble Plume Model

[6] The linear bubble plume model utilizes the discrete-bubble approach, which has also been applied to the airlift aerator and Speece cone and was recently reviewed in detail by *Singleton and Little* [2006]. The linear bubble plume

model is composed of horizontally integrated equations based on the conservation of mass, momentum, and heat. Eight flux equations are solved simultaneously to predict water flow rate, plume temperature, oxygen and nitrogen transfer and concentration, salinity, and plume rise height, given diffuser geometry and depth, applied gas flow rate, and initial bubble size (Tables 1 and 2). The model accounts for density stratification due to vertical temperature and salinity gradients. Entrainment is assumed to be proportional to the local (with respect to depth) plume water velocity and perimeter. Bubble size varies as the bubbles rise due to expansion and dissolution, and bubble slip velocity and gas transfer coefficients are functions of bubble radius [*Wüest et al.*, 1992]. Also, Henry's constants for oxygen and nitrogen are functions of temperature [*Wüest et al.*, 1992]. The bubble plume model equations were originally developed by *Wüest et al.* [1992] for circular geometry but were modified by *McGinnis et al.* [2001] for the linear geometry of the system installed in SHR. The equations that include the spreading coefficient (λ) were recently refined [*Singleton and Little*, 2005] to more accurately reflect the geometry of the plume at the ends of the linear diffuser (Tables 1 and 2), which is approximated in plan view as a long, thin rectangle. Additional refinements to the model of *McGinnis et al.* [2001], which are detailed in the following paragraphs, include use of a correlation to calculate initial bubble size [*McGinnis and Little*, 2002], correction of the entrainment coefficient (α) and λ for top-hat profiles, and use of a Froude number (*Fr*) to calculate initial water velocity [*Fischer et al.*, 1979; *Wüest et al.*, 1992]. Also, water quality profiles from the plume near-field, as opposed to the reservoir far-field, were used as boundary conditions [*McGinnis et al.*, 2004].

[7] The entrainment coefficient and λ were set at 0.11 and 0.93, respectively. These values were derived by *Fanneløp et al.* [1991] by fitting Gaussian profiles to laboratory data and were modified for the top-hat profile assumption of the model using [*Fanneløp and Sjøen*, 1980]

$$\alpha_T = \sqrt{2}\,\alpha_G \qquad (1)$$

$$\lambda_T = \sqrt{\frac{\lambda_G^2 + 1}{2}}, \qquad (2)$$

where the subscripts T and G refer to top-hat and Gaussian profiles, respectively. For simplicity, top-hat or uniform profiles are assumed for water velocity, temperature, salinity, dissolved and gaseous constituents, and bubble velocity [*Wüest et al.*, 1992]. Other model assumptions are as follows: (1) The linear plume width W for temperature and dissolved constituents is equal to the width of the plume velocity profile, whereas the bubbles are confined to an inner core of width λW ($\lambda < 1$); (2) ambient currents are negligible; (3) the diffuser produces bubbles at a constant rate and uniform size that are evenly distributed over the cross section of initial width λW_o; (4) bubble coalescence is neglected; (5) initial water properties of the plume are those of ambient water at the diffuser depth; and (6) exchange of gases other than oxygen and nitrogen is not considered.

[8] The model predictions are strongly dependent on the initial plume conditions and the plume boundary conditions

Table 1. Key Variables of the Linear Bubble Plume Model[a]

Variable	Formula	Units
Entrainment factor	$E = 2(L + W)\alpha v$	m²/s
Plume water volume flux	$Q = LWv$	m³/s
Momentum flux	$M = LWv^2$	m⁴/s²
Temperature flux	$F_T = QT_p$	°C m³/s
Dissolved solids flux	$F_s = QS\rho_w$	kg/s
Dissolved O_2 and N_2 fluxes	$F_{D_i} = QC_i$	mol/s
Gaseous O_2 and N_2 fluxes	$F_{G_i} = \lambda W[L - W(1 - \lambda)](v + v_b)y_i$	mol/s

[a]Revised from *McGinnis et al.* [2001].

of temperature, dissolved oxygen, and salinity. Initial conditions for the bubble plume model were determined as detailed by *Wüest et al.* [1992], except for the following deviations. Initial bubble size is calculated using the correlation developed by *McGinnis and Little* [2002] for the type of linear diffuser installed in SHR:

$$d_{3,2} = 1.12 + 0.938q. \qquad (3)$$

The correlation was determined using measured Sauter-mean bubble diameter ($d_{3,2}$) values of 1.1–2.2 mm collected over actual unit gas flow rates q of 0.08–0.88 m²/h at the diffuser.

[9] For the circular bubble plume model, *Wüest et al.* [1992] proposed that the induced vertical water velocity v at the diffuser depth is equivalent to the initial plume water velocity. To estimate the initial velocity, *Wüest et al.* [1992] defined a densimetric Fr and utilized a relationship between the local Richardson number (Ri) and Fr derived by *Fischer et al.* [1979] for single-phase, round buoyant jets discharging vertically. The circular bubble plume model was recently validated by *McGinnis et al.* [2004], so a similar procedure was used to determine the initial plume velocity for the linear bubble plume. Corresponding equations for Fr were derived for planar or linear plumes using relationships presented by *Fischer et al.* [1979] to obtain

$$Fr = Ri^{-\frac{3}{4}} \qquad (4)$$

$$Fr = \frac{v}{\left[\lambda Wg\left(\rho_a - \rho_p\right)/\rho_p\right]^{\frac{1}{2}}}; \qquad (5)$$

where g is gravitational acceleration, ρ_a is the ambient water density, and ρ_p is the bubble plume density. The local Ri for planar jets has a constant value of 0.735 at distances from

the source where the flow is more like a plume [*Fischer et al.*, 1979]. Consequently, Fr for a planar or linear plume is equal to 1.26, except close to the source. *Wüest et al.* [1992] assumed that the bubble slip velocity near the source was relatively low, so the initial Froude number (Fr_o) should be equal to the value for a single-phase plume. Unlike the circular plume model, the Fr profiles predicted by the linear bubble plume model continually increase with depth for the diffuser installed in SHR (not shown). For $Fr_o \leq 2.0$, the plume velocity initially increases with decreasing depth immediately above the linear diffuser (Figure 1a). This effect was also predicted by *Fanneløp and Webber* [2003] for buoyant plumes rising from areal sources, where a point of maximum velocity occurred above the source. Additionally, the plume neck (point of minimum radius or width) is always below the point of maximum velocity in the plume [*Fanneløp and Webber*, 2003]. A neck is not predicted for the linear bubble plume when $Fr_o = 2.0$ (Figure 1b). However, necking or contraction will only occur when the momentum immediately above the source is relatively low and/or the entrainment coefficient is relatively low [*Fanneløp and Webber*, 2003]. Also, *Wüest et al.* [1992] reasoned that a plume from an open source (diffuser above sediments) may not contract because initially entrained water is not obstructed. Therefore Fr_o for an open source will likely be higher than that for a closed source (diffuser resting on sediments). Because the linear diffuser in SHR is an open source (Figure 2), Fr_o for the linear bubble plume was assumed to be 2.0, and a sensitivity analysis was conducted to determine the effect of varying Fr_o.

[10] The differential flux equations of the linear bubble plume model (Table 2) were solved numerically using the fourth-order Runge-Kutta method. Further information on the general solution procedure, equations of state, and model assumptions is provided by *Wüest et al.* [1992] and *McGinnis et al.* [2004]. The model calculations are only valid over the plume rise height, up to the DMPR. When the plume stops rising, a secondary plume may form above as bubbles that are not completely dissolved continue to rise [*Asaeda and Imberger*, 1993; *McDougall*, 1978; *Schladow*, 1992]. This phenomenon can occur when a bubble plume is released into strong density stratification.

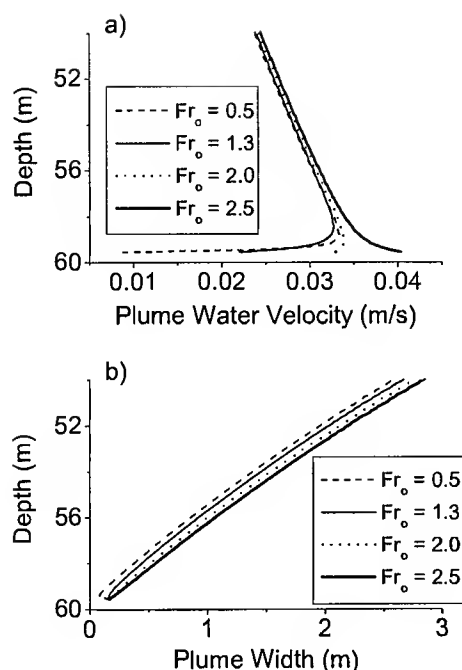## 4. Application to Spring Hollow Reservoir, Virginia

4.1. Field Data Collection

[11] To fully evaluate the linear bubble plume model, experimental data for boundary conditions, rise height, and in-plume constituent profiles are required. Testing was

Table 2. Nonlinear Differential Flux Equations of the Linear Bubble Plume Model[a]

Flux	Equation
Water volume	$dQ/dz = E$
Momentum	$dM/dz = [(\rho_a - \rho_w)/\rho_p]gLW + [(\rho_w - \rho_p)/\rho_p]g\lambda W[L - W(1 - \lambda)]$
Temperature	$dF_T/dz = ET_a$
Salinity	$dF_s/dz = E\rho_a S_a$
Dissolved gas	$dF_D/dz = EC_a + [4\pi r^2 N/(v + v_b)]K_L(H_i P_i - C_i)$
Gas	$dF_G/dz = -[4\pi r^2 N/(v + v_b)]K_L(H_i P_i - C_i)$

[a]Revised from *McGinnis et al.* [2001].

Figure 1. Effect of initial Froude number (Fr_o) on predictions of plume water velocity and plume width using linear bubble plume model.

conducted using a full-scale linear diffuser (Figure 2) installed in Spring Hollow Reservoir, Virginia (Figure 3). Constructed in 1995, SHR is a small monomictic, mesotrophic side-stream reservoir that is generally stratified from May to December. The reservoir is managed by the Western Virginia Water Authority and serves as one of the principle drinking water sources for Roanoke County. The water body has a maximum depth of 65 m and a maximum surface elevation of 431 m. The approximate surface area and volume are 0.54 km² and 12.4 × 10⁶ m³, respectively. To prevent anoxia in the hypolimnion and the associated deterioration of raw water quality, a linear diffuser equipped with fine-bubble porous hoses was installed in 1997 (Figure 3). The 305-m-long diffuser can be supplied with compressed air or pure oxygen at various gas flow rates and is located in the deepest portion of the reservoir (368–372 m elevation). On the basis of an average surface elevation of 430 m, the depth of the diffuser during testing ranged from 58 to 62 m along its length. Table 3 provides the diffuser operating parameters in 2003 and 2004.

[12] Diffuser tests were performed in 2003 using compressed air (21% O_2) supplied at a high gas flow rate (45 Nm³/h average) during 29 June to 14 July and pure oxygen (97% O_2) supplied at a low flow rate (11 Nm³/h average) during 14–26 August. A third test was conducted in 2004 using pure oxygen, but at a higher gas flow rate (40 Nm³/h maximum) during 22 October to 5 November. In 2003, the diffuser quickly mixed the rather small hypolimnetic volume during both tests, and the water quality conditions on the dates of data collection (2 July and 17 August for compressed air and pure oxygen, respectively) were by that time relatively homogeneous as a result of plume-induced mixing. One of the primary objectives of the 2004

experiments was to maximize the plume signature in the hypolimnion and to increase confidence in the linear plume model validation under a different set of boundary conditions. In 2004, the data were therefore collected on 24 October, soon after start of diffuser operation. Additionally, the 2004 test was performed later in the stratified season to maximize the ambient DO and temperature gradients in the hypolimnion.

[13] To establish appropriate boundary conditions for the plume model, characterization of the plume near-field environment is necessary [McGinnis et al., 2004]. Therefore the data collected included numerous high-spatial-resolution CTD (Sea-Bird model SBE 19plus; 4-Hz sampling rate) transects measured almost daily before, during, and after diffuser operation. The CTD profiler was also equipped with a DO probe (1.4-s response time measured at 20°C). Profiles were obtained laterally across the diffuser at 0.5-m increments for 0–10 m, 2-m increments for 10–20 m, and 5-m increments for 20–40 m from the centerline of the diffuser in both directions (Figures 3 and 4). (The diffuser centerline location is shifted to the left for 2004 (Figures 4c and 4f) because the diffuser was repositioned earlier in the year. Also, the operational length of the diffuser was decreased for that year (Table 3).)

[14] The geometry of SHR affects the extent and rate of circulation within the hypolimnion induced by the bubble plume. Because of the relatively small size of SHR, operation of the linear diffuser created uniform conditions below the thermocline within days after startup. While SHR bathymetry influences plume-induced mixing in the hypolimnion, the effect on short-term plume operation is negligible because the time that individual bubbles spend in the hypolimnion is of the order of minutes. The bubbles and resulting plume experience a pseudo steady state with respect to ambient conditions. Effects on data collection due to the ends of the linear diffuser were assumed to be negligible because the lateral profile location was over 150 m from a diffuser end (Figure 3), and the diffuser is designed to release a uniform gas flow along its length.

4.2. Observations and Model Validation

[15] Plume rise height, spreading, and constituent profiles predicted by the linear bubble plume model were compared with experimental observations. Critical model input parameters for the three test conditions (2 July 2003, 17 August 2003, and 23 October 2004) are shown in Table 3. The boundary conditions were obtained from averaged near-field lateral profiles [McGinnis et al., 2004] (±2 m and ±1 m from plume centerline for 2003 and 2004, respectively) and differed significantly between 2003 and 2004 (Figure 5). (The presence of two thermoclines in 2003 is due to the pumped reservoir inflow that discharges at 396-m elevation, which corresponded to approximately 34-m depth during diffuser testing. The lower thermocline delineates the effective hypolimnion for the oxygenation system.)

[16] Measured contours of temperature and DO are shown in Figure 4, along with corresponding model predictions for plume width and the DMPR. The actual plume boundaries are not well defined in the contour plots, so comparison with predicted plume widths is difficult. The lack of distinct plume boundaries was due to the almost well mixed conditions in the hypolimnion as a result of diffuser
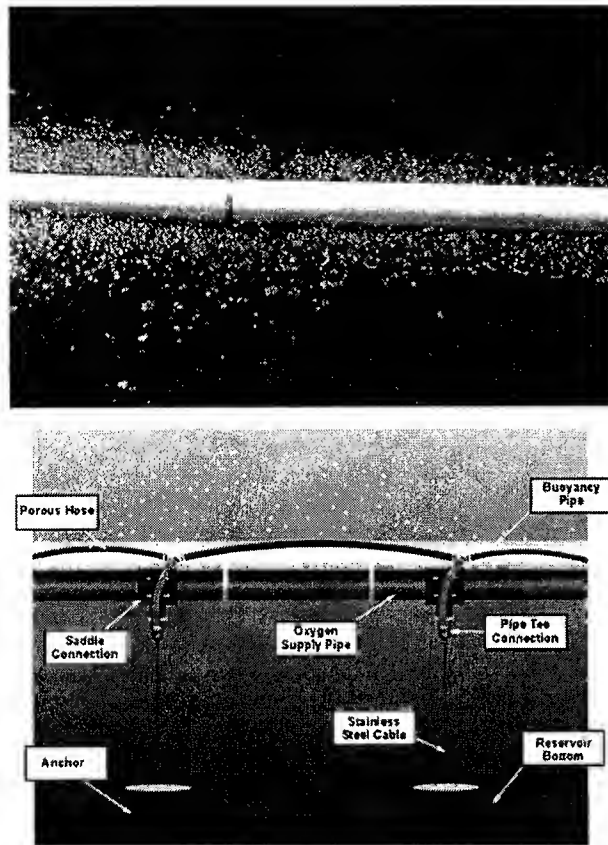
Figure 2. Photograph and schematic of linear bubble plume diffuser in Spring Hollow Reservoir, Virginia. Courtesy of Mark Mobley, Mobley Engineering, Inc.

operation, particularly for 2003 (Figures 4a–4d). Also, use of compressed air did not produce a strong DO plume signature for the July test compared with the August and October tests with pure oxygen. The actual plume rise height is easier to distinguish, especially in the DO contours for August and October. The predicted depths of maximum plume rise are 38.2, 46.1, and 48.8 m for July, August, and October, respectively. For July and October, the DMPR is simulated well by the model (Figures 4a, 4b, 4e, and 4f). However, the model appears to underestimate the plume rise height for August, when the gas flow rate was comparatively low (Table 3). The under-predicted DMPR may have been due to an overestimated value for α. In a detailed study of round plumes, *Milgram* [1983] found that α is directly proportional to the plume gas holdup or fraction. However, the linear bubble-plume model assumes that α is constant (Table 3).

[17] The structure of the plumes is similar to those observed by *Asaeda and Imberger* [1993] for round bubble plumes in weak stratification (Figure 4). Depending on the gas flow rate and stratification strength, three types of horizontal intrusions from the plume were reported. The pattern of the DO contours for October (Figure 4f) closely resembles type 1, which corresponds to a high gas flow rate or weak stratification [*Asaeda and Imberger*, 1993]. This is similar to a single plume impinging on a free surface, which

is analogous to the thermocline in SHR. Although the plume for July is not easily discerned from the temperature or DO contours, the structure is most likely similar to a type 1 plume. The July plume appears to detrain primarily at the lower thermocline with one strong intrusion, as evidenced by accumulation of higher oxygenated water near the top of the plume (Figure 4b). The plume for August is best classified as type 3, which is for low gas flow rates or strong density stratification [*Asaeda and Imberger*, 1993]. Type 3 plumes do not have steady intrusions, but instead are characterized by alternating, collapsing eddies that cause the plume to meander.

[18] Referring to the October test (Figure 4f), the higher DO concentrations at lower depths adjacent to both sides of the plume were likely the result of detrained water that sinks past the equilibrium depth due to momentum. The temperature isotherms were also depressed immediately beside the plume (Figure 4e). This phenomenon was also observed by *McGinnis et al.* [2004]. The DO concentration immediately above the predicted DMPR and near the vertical plume centerline for October 2004 is higher than the ambient concentration (Figure 4f). This could have been caused by the formation of a secondary plume above the DMPR resulting from incompletely dissolved bubbles. The model estimates that the bubble size at the top of the first plume was about 5×10^{-5} m for October 2004, which is relatively large compared with July 2003 and August 2003 (Figure 6f). These undissolved bubbles could have created a secondary plume, which entrained oxygenated water from the detrainment of the first plume and carried it higher into the water column.

[19] Vertical profiles of constituents and properties within the plumes were also predicted for the three diffuser tests (Figure 6). For the July test with compressed air, the higher gas flux creates a greater buoyancy flux and a higher initial plume water velocity (Figure 6d). Also, the concentration driving force for oxygen transfer is lower compared with pure oxygen, which decreases the rate of bubble dissolution with depth (Figure 6f). These effects result in a higher DMPR for July compared with August (Figures 4 and 6). The model predictions for 2004 differ from those of 2003 because of the differing boundary conditions (Figure 5). The plume rise height for the October test with pure oxygen is less than that for August, even though the gas flux was more than tripled (Table 3). The ambient temperature, and hence density, stratification was stronger in 2004, which provided greater negative buoyancy to decrease plume momentum. The stronger ambient density stratification also caused the plume velocity to decrease more rapidly with depth in 2004 despite a higher initial velocity from the diffuser (Figure 6d). The lower plume rise height in October resulted in lower plume water flow rates than July (Figure 6e), even with comparable gas fluxes applied (Table 3).

[20] Average temperature, DO, and density profiles within the plumes were also measured (Figures 6a–6c). The temperature, and consequently density, predictions for July and October deviate from the measured profiles where the plumes reach the top of the hypolimnion (Figures 6a and 6c), or where the rate of plume spreading is greatest (Figure 4). The model underpredicts the final plume temperature by approximately 0.3° and 0.2°C for July and October, respectively. One reason for the discrepancy
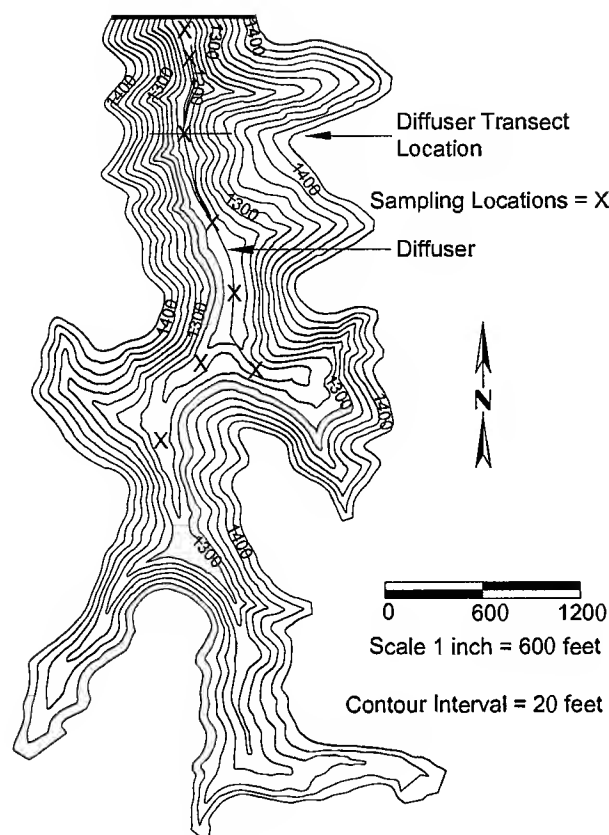
Figure 3. Bathymetric map of Spring Hollow Reservoir, Virginia, showing locations of linear bubble plume diffuser and conductivity-temperature-depth (CTD) lateral transects.

may be that the model assumes α is constant. In addition to the dependence on plume gas holdup, *Milgram* [1983] also found that α for a circular plume is directly proportional to the local plume radius. As the plume approaches its maximum rise height, the width increases rapidly

(Figure 4). If linear plume dynamics are similar to circular plumes, then α for linear plumes may also increase as the plume width increases. Additionally, the boundary profiles selected may not accurately reflect the actual ambient conditions immediately adjacent to the plume along its entire rise height. Measured vertical CTD profiles at the estimated plume width were averaged and used for boundary conditions. However, the plume width varies greatly with depth (Figure 4), so use of vertical profiles at a single lateral distance from the diffuser is not appropriate. Also, the average plume width was visually estimated from the temperature and DO contour plots (Figure 4), but the actual plume boundaries are not well defined.

[21] The model predicts the plume DO profiles well for all three diffuser tests (Figure 6b). For July and August the model characterizes the initial increase in DO immediately above the diffuser quite accurately. The initial rapid increase in DO for August and October is due to the higher oxygen saturation concentration at depth with the use of pure oxygen. The high hydrostatic pressure causes the oxygen transfer rate to be almost independent of the ambient DO concentration at the depth of diffuser. By contrast, the initial DO increase for the July test with compressed air is more modest (Figure 6b). The shape of the predicted DO profile for October differs somewhat from the experimental data, even though the final values at the DMPR differ by only 0.3 g/m^3. The hypolimnion and hence the plume near-field were more heterogeneous in 2004 than 2003, which may have contributed to the overprediction at lower depths if the selected boundary profiles did not accurately represent water entrained into the plume.

[22] Another source of inaccuracy could be the correlation equation used to calculate initial bubble size (equation (3)). This relationship was developed using data collected over actual air flow rates per unit length of diffuser of 0.08–0.88 m^2/h [*McGinnis and Little*, 2002]. The actual gas flow rates per unit length of diffuser for the July, August, and October tests were 0.019, 0.0063, and 0.024 m^2/h, respectively. Therefore the initial bubble diameters used in the model were extrapolated beyond the valid correlation range.

Table 3. Conditions for Linear Bubble Plume Model Validation and Sensitivity Analysis for Spring Hollow Reservoir, Virginia[a]

Parameter	2 July 2003	17 Aug 2003	23 Oct 2004	Sensitivity Range
Oxygen in gas supply, %	21	97	97	n/a
Entrainment coefficient [ ]	0.11	0.11	0.11	0.05–0.2
Spreading coefficient [ ]	0.93	0.93	0.93	0.5–1.0
Initial Froude number [ ]	2.0	2.0	2.0	1.0–3.0
Operational diffuser length, m	300	300	250	60–625
Initial plume width, m	0.16	0.16	0.16	n/a
Initial plume area, m^2	50	50	42	10–100
Gas flow rate,[b] Nm^3/h	38	13	40	1–400
Initial gas flux,[c] m/h	0.76	0.26	0.96	0.02–9.5
Initial bubble radius, m	5.7×10^{-4}	5.6×10^{-4}	5.7×10^{-4}	$10^{-4}–10^{-1}$
Diffuser depth,[d] m	60	60	59	n/a
Reservoir maximum depth, m	64	65	64	n/a
Reservoir surface area, $10^6 m^2$	0.53	0.53	0.53	n/a
Reservoir total volume, $10^6 m^3$	12	12	12	n/a

[a]Reservoir conditions on testing days are also included.
[b]Nm^3 denotes 1 m^3 of gas at 1 bar and 0°C.
[c]Sensitivity analysis range refers to varying gas flow rate while maintaining constant initial plume area.
[d]Depth at location of lateral CTD transect.
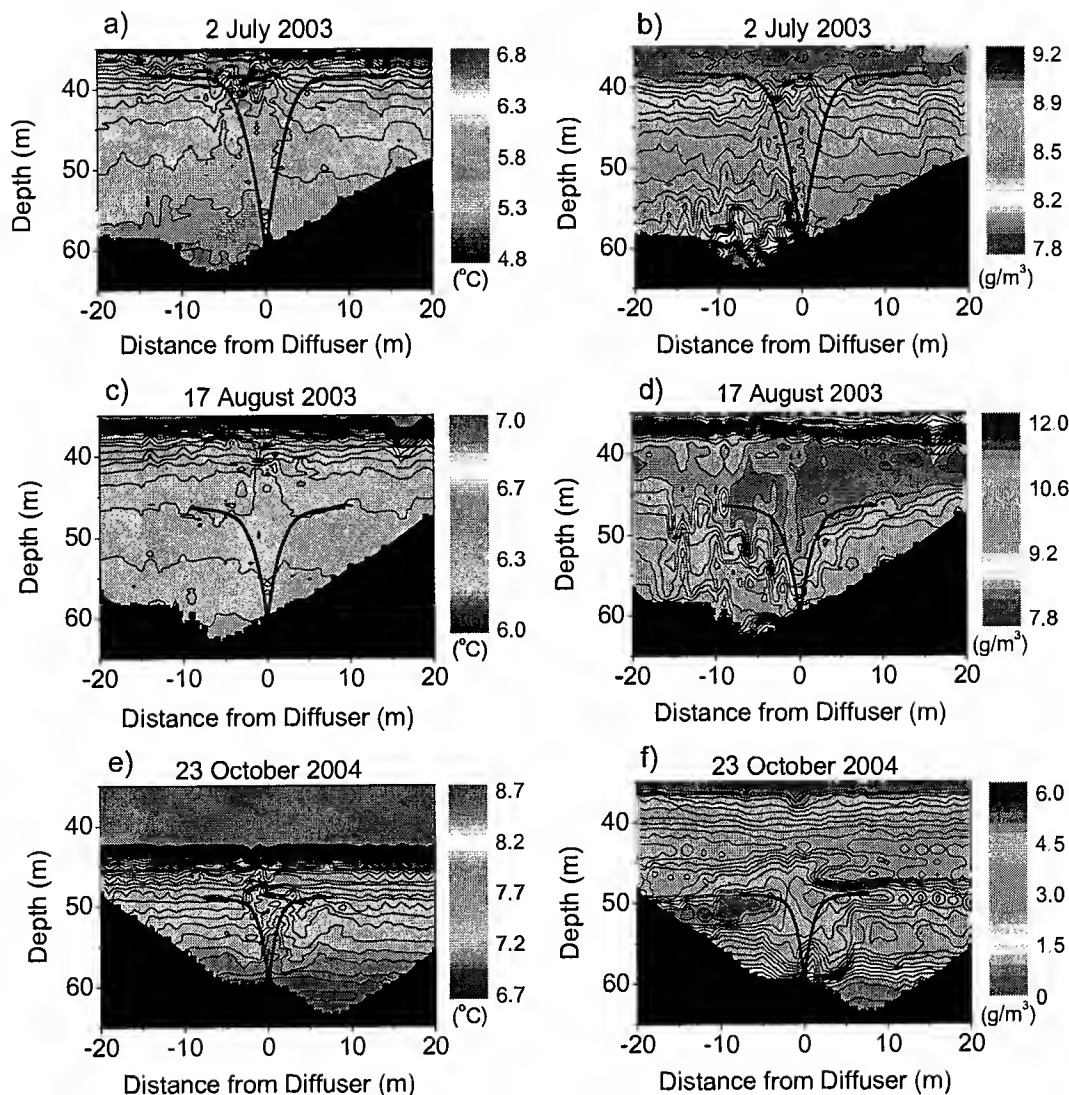
Figure 4. Measured (left) plume temperature (°C) and (right) dissolved oxygen (DO) (g/m³) contours with linear bubble plume model predictions for diffuser operation with air (2 July 2003) and pure oxygen (17 August 2003 and 23 October 2004) in Spring Hollow Reservoir, Virginia. Contours were interpolated from CTD profiles collected at locations indicated by small black squares along the bottom of each plot.
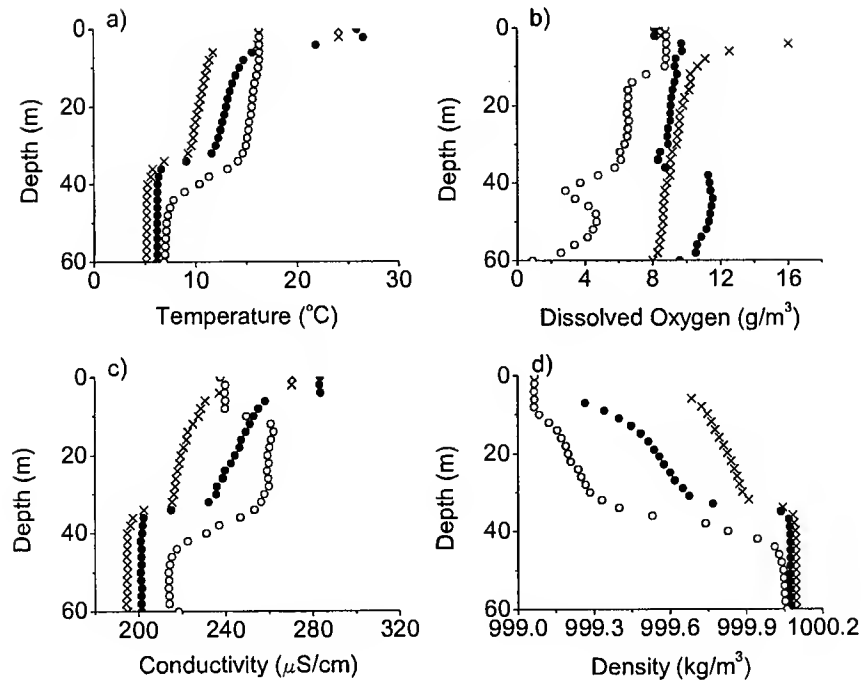
4.3. Sensitivity Analysis

[23] A sensitivity analysis was performed with the linear bubble plume model to determine the effects on plume rise height, oxygen transfer efficiency, and induced water flow rate, because these parameters are important for design and operation of hypolimnetic aeration/oxygenation systems. Parameter perturbation was used, in which input variables are independently adjusted to determine their individual effects on model predictions. The model variables investigated are either difficult to measure or can be controlled through system design or operation (Table 3). Currently, α and λ for the linear plume model are empirical constants [*Fanneløp et al.*, 1991], and the initial plume water velocity is calculated using a densimetric *Fr* [*Wüest et al.*, 1992]. The initial plume area, gas flow rate, and, to a lesser extent, initial bubble size can be controlled through diffuser design and operation. The sensitivity of model predictions to

ambient dissolved nitrogen was also examined for the standard case using compressed air (2 July 2003). The model assumes that the background dissolved nitrogen concentration is equivalent to the saturated value at atmospheric partial pressure and the average hypolimnetic water temperature.

[24] The DMPR is most influenced by gas flow rate and initial bubble radius (Figures 7e and 7f). The gas flow rate is directly related to the density of the plume bubble-water mixture and subsequently the positive buoyancy and upward momentum of the plume (Table 2). For gas flow rates greater than approximately 100 Nm³/h, the plume rise height is controlled more by the depth of the thermocline in SHR (Figure 5a). As the plume rise height approaches the thermocline, further increases in the buoyancy and momentum fluxes can not overcome the strong ambient density stratification. The 2003 predictions are more a function of

Figure 5. Input boundary conditions for linear bubble plume model validation and sensitivity analysis. Data collected from Spring Hollow Reservoir, Virginia, during diffuser operation with compressed air (2 July 2003, crosses) and pure oxygen (17 August 2003, solid circles, and 23 October 2004, open circles).

gas flow rate than those for October 2004 because of differing boundary conditions (Figure 5).

[25] The plume rise height is moderately sensitive to initial bubble radius (Figure 7f). For initial radii less than about 1 mm, the DMPRs are nearly independent of bubble size. As initial bubble sizes increase, the plumes ascend higher and reach a maximum height for a radius of about 6 mm for each diffuser test. The shapes of the curves can be attributed to the dependence of bubble rise velocity and gas transfer coefficients on bubble radius [*Wüest et al.*, 1992]. The DMPR predictions for August are more sensitive to initial bubble radius than those for July and October (Figure 7f). The plume on 17 August 2003 did not have sufficient buoyancy and momentum to rise to the thermocline because a relatively low gas flow rate was applied (Figure 4c and Table 3). By contrast, the plume dynamics for July and October were influenced to a greater degree by the thermocline, which in effect damped the sensitivity of plume rise height to the initial bubble radius.

[26] The predicted DMPR for the linear bubble plume is virtually independent of Fr_0 and λ over the ranges analyzed (Figures 7b and 7c). The plume rise height is moderately sensitive to α. Entrainment into the plume is a function of plume size, water velocity, and α (Table 1), and entrainment of ambient water decelerates the plume. Plume rise is influenced to a somewhat greater degree by the initial plume area. As the plume area is increased, the buoyancy flux decreases because the gas flow rate is constant. Plume rise height was unaffected by variations in the ambient dissolved nitrogen concentration from 50 to 200% saturation in the hypolimnion for the 2 July 2003 diffuser test. Similar to the analysis for DMPR, induced water flow rate at the top of the plume was found to be insensitive to Fr_0 and λ and

somewhat more sensitive to α and the initial plume area (results not shown). Plume water flow rate is most influenced by gas flow rate and initial bubble radius. Higher gas flow rates produce greater buoyancy and momentum fluxes, which results in greater plume rise heights and increased entrainment.

[27] Oxygen transfer efficiency (total mass of oxygen transferred relative to initial mass of oxygen in bubbles) within the hypolimnion was independent of all parameters except initial bubble radius, decreasing from nearly 100% to around 20% for air and pure oxygen as the initial radii increased from approximately 1 mm to 1 cm (Figure 8). Oxygen transfer can continue above the DMPR if the bubbles are not dissolved. However, secondary plumes are not accounted for in the model. Even though undissolved bubbles at the top of the plume may continue to transfer oxygen during ascent, the oxygen may not be added at the desired depth (i.e., below the thermocline). A local minimum with respect to induced water flow rate at the top of the plume is predicted for a bubble radius of about 1 mm for the conditions in SHR (not shown). This suggests that while maximum oxygen transfer efficiency can be achieved with a 1-mm initial bubble radius, vertical water circulation, and hence oxygen distribution in the hypolimnion, will not be optimized. As the bubble radius is increased from 1 mm, induced water flow rate increases as well for radii up to 5 mm, but oxygen transfer efficiency decreases rapidly within this range (Figure 8).

5. Comparison of Linear and Circular Bubble Plume Models

[28] The primary difference between the linear and circular bubble plume models is the plume geometry. For a
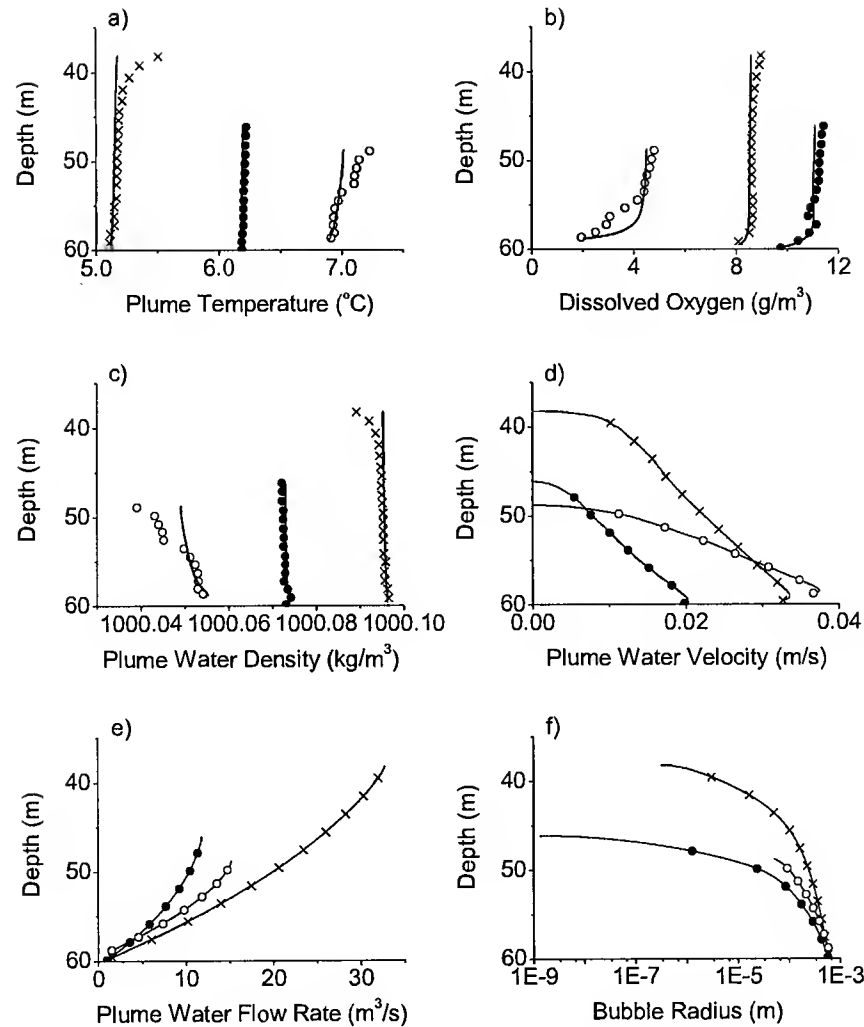
Figure 6. In-plume profiles predicted by linear bubble plume model, represented as (a–c) solid lines and (d–f) solid lines and symbols. Input data collected from Spring Hollow Reservoir, Virginia, during diffuser operation with compressed air (2 July 2003, crosses) and pure oxygen (17 August 2003, solid circles, and 23 October 2004, open circles). Measured average in-plume temperature, DO, and plume water density represented as symbols (Figures 6a–6c).

given plume cross-sectional area, the perimeter of a linear plume is much greater than for a circular or round plume. The initial estimated plume area and perimeter of the linear diffuser in SHR for July 2003 was about 50 m² and 600 m, respectively (Table 3). This corresponds to an equivalent radius and perimeter of approximately 4 m and 25 m, respectively, for a circular plume. In this case, the perimeter of the linear plume is 24 times greater than for the circular plume. For both the linear and circular plume models, entrainment of ambient water is directly proportional to local plume perimeter, local plume water velocity, and α (Table 1). The larger perimeter of the linear plume greatly increases ambient entrainment, which contributes to the negative buoyancy of the plume and causes the plume to decelerate more rapidly. This results in a lower plume rise height compared with the circular plume.

[29] The sensitivity of the linear bubble plume model to various parameters was comparable to results for the circu-

lar bubble plume model analysis. Gas flow rate had the greatest effect on DMPR predictions by both models, and the linear plume model was less sensitive to initial bubble radius than the circular plume model was [*Wüest et al.*, 1992]. The latter may be due to differences between temperature boundary conditions, which caused plume dynamics in SHR to be more influenced by thermocline depth. Initial bubble size greatly affected oxygen transfer efficiency for both diffuser geometries, decreasing rapidly as the radii increased beyond 1 mm and 3 mm for the linear and circular plumes, respectively. Both the linear and circular plume model predictions for DMPR were relatively insensitive to Fr_o and initial plume area (Figure 7 and *Wüest et al.* [1992]). However, circular model predictions for DMPR were more sensitive to α. Overall, the linear model was less sensitive to input parameters than the circular model, but this insensitivity is probably due to the relatively
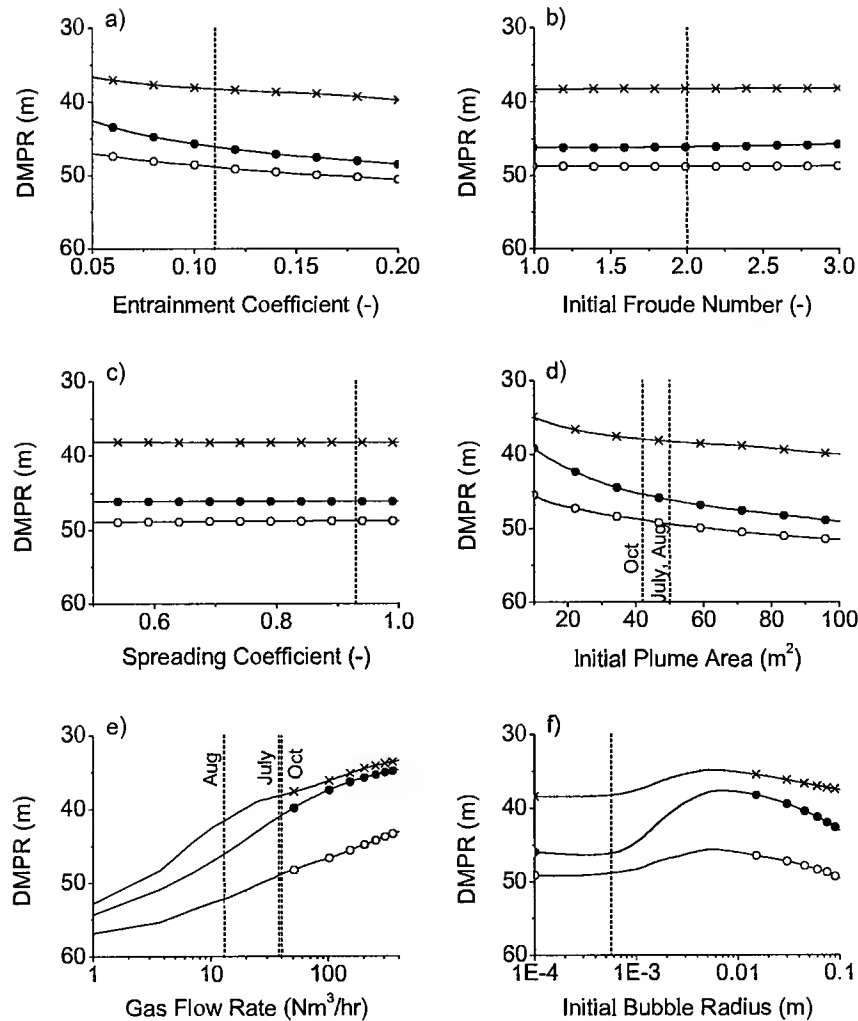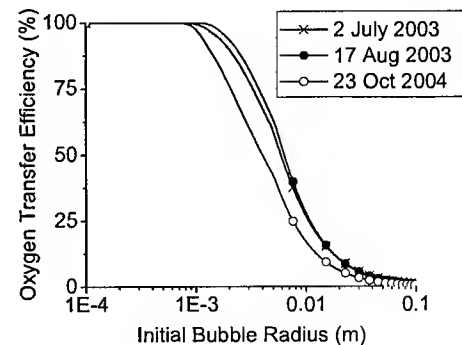
Figure 7. Effect of linear bubble plume model parameters on depth of maximum plume rise (DMPR). Standard values for each parameter are indicated by the vertical dashed lines. Input data collected from Spring Hollow Reservoir, Virginia, during diffuser operation with compressed air (2 July 2003, crosses) and pure oxygen (17 August 2003, solid circles, and 23 October 2004, open circles).

homogeneous boundary conditions in the hypolimnion of SHR caused by diffuser mixing.

6. Summary and Conclusions

[30] In the current work, the linear bubble plume model of *McGinnis et al.* [2001] was improved, and the updated model was evaluated using data collected from a full-scale hypolimnetic oxygenation system installed in Spring Hollow Reservoir, Virginia. Three diffuser experiments were conducted using compressed air and pure oxygen over a range of flow rates. Predicted plume rise height, spreading, and constituent profiles were compared with experimental observations. For July 2003 and October 2004, the DMPR was simulated well by the model. However, the model underestimated the plume rise height for August 2003, when the gas flow rate was comparatively low. The model underpredicted the final plume temperature by approximately $0.3°$ and $0.2°C$ for July 2003 and October 2004, respectively. The model predicted the plume DO

Figure 8. Effect of initial bubble radius on oxygen transfer efficiency predicted by linear bubble plume model. Input data collected from Spring Hollow Reservoir, Virginia, during diffuser operation with compressed air (2 July 2003) and pure oxygen (17 August 2003 and 23 October 2004).

profiles very well for all three diffuser tests, including simulating the initial rapid transfer of oxygen immediately above the diffuser.

[31] A sensitivity analysis was performed to determine the effect of various model input parameters. The DMPR and induced water flow rate were most influenced by gas flow rate and initial bubble radius, moderately sensitive to α and the initial plume area, and insensitive to Fr_o, λ, and ambient dissolved nitrogen. Oxygen transfer within the hypolimnion was independent of all parameters except initial bubble radius, decreasing from nearly 100% to around 20% for air and pure oxygen as the initial radii increased from approximately 1 mm to 1 cm.

[32] The linear bubble plume model for hypolimnetic oxygenation has been successfully validated. The model can be used to design lake and reservoir oxygenation systems and to optimize existing systems to maximize oxygen addition. Application of the linear plume model requires knowledge of the gas flow rate, initial bubble radius, initial plume area, and near-field constituent profiles (boundary conditions). Additionally, several empirical parameters must be estimated including α and λ. Even though all of the model inputs may not be known with certainty for a given aeration or oxygenation system, the model can be used for preliminary design and coarse optimization. Also, plume rise height, water flow rate, and oxygen transfer efficiency were found to be primarily dependent on gas flow rate and initial bubble radius.

[33] Operation of bubble plumes for hypolimnetic oxygenation usually alters the ambient temperature and DO conditions of a water body. Plume dynamics and oxygen transfer are strongly related to the near-field water column properties, establishing a feedback loop that continually changes plume dynamics. This complex plume-lake interaction should be accounted for in the design and operation of bubble plume diffusers. *McGinnis et al.* [2001] performed a preliminary coupling of the linear bubble plume model with an existing reservoir model, CE-QUAL-W2 [*Cole and Wells*, 2003], and obtained encouraging results. Efforts are currently under way to further develop the coupled model to predict plume performance and the near- and far-field reservoir responses. In the absence of near-field boundary profiles, far-field or simulated constituent profiles can be used to provide a reasonable estimate of plume performance.

Notation

b plume radius (circular bubble plume), m.
d bubble diameter, mm.
C dissolved concentration, mol/m^3.
E entrainment factor, m^2/s.
F_D dissolved species flux, mol/s.
F_G gaseous species flux, mol/s.
F_S salinity flux, kg/s.
F_T temperature flux, °C m^3/s.
Fr Froude number [ ].
g gravitational acceleration, m/s^2.
H Henry's constant, mol/m^3/bar.
K_L mass transfer coefficient, m/s.
L plume length, m.
M water momentum, m^4/s^2.

N number flux of bubbles, 1/s.
P pressure, bar.
Q plume flow rate, m^3/s.
q actual gas flow rate per unit diffuser length, m^2/h.
Ri Richardson number [ ].
R bubble radius, m.
S salinity, g/kg.
T temperature, °C.
v velocity, m/s.
W plume width, m.
y gaseous concentration, mol/m^3.
Z depth, m.

Greek letters

α entrainment coefficient [ ].
λ spreading coefficient [ ].
ρ density, kg/m^3.

Subscripts

3,2 Sauter-mean.
G Gaussian profile.
O oxygen.
N nitrogen.
T top-hat profile.
a ambient water.
b bubble.
i gas species, oxygen or nitrogen.
o initial.
p plume water and gas mixture.
w plume water.

References

Asaeda, T., and J. Imberger (1993), Structure of bubble plumes in linearly stratified environments, *J. Fluid Mech.*, *249*, 35–57.

Brevik, I. (1977), Two-dimensional air-bubble plume, *J. Waterw. Port Coastal Ocean Div. Am. Soc. Civ. Eng.*, *103*, 101–115.

Brevik, I., and R. Kluge (1999), On the role of turbulence in the phenomenological theory of plane and axisymmetric air-bubble plumes, *Int. J. Multiphase Flow*, *25*, 87–108.

Burris, V. L., D. F. McGinnis, and J. C. Little (2002), Predicting oxygen transfer and water flow rate in airlift aerators, *Water Res.*, *36*, 4605–4615.

Cole, T. M., and S. A. Wells (2003), CE-QUAL-W2: A two-dimensional, laterally averaged, hydrodynamic and water quality model, Version 3.2, U.S. Army Eng. and Res. Dev. Cent., Vicksburg, Miss.

Cooke, G. D., and R. E. Carlson (1989), *Reservoir Management for Water Quality and THM Precursor Control*, 387 pp., Am. Water Works Assoc. Res. Found., Denver, Colo.

Ditmars, J. D., and K. Cederwall (1974), Analysis of air-bubble plumes, paper presented at the 14th Coastal Engineering Conference, Am. Soc. of Civ. Eng., Copenhagen, 24–28 June.

Fanneløp, T. K., and K. Sjøen (1980), Hydrodynamics of underwater blowouts, *Norw. Marit. Res.*, *4*, 17–33.

Fanneløp, T. K., and D. M. Webber (2003), On buoyant plumes rising from area sources in a calm environment, *J. Fluid Mech.*, *497*, 319–344.

Fanneløp, T. K., S. Hirschberg, and J. Kueffer (1991), Surface current and recirculating cells generated by bubble curtains and jets, *J. Fluid Mech.*, *229*, 629–657.

Fischer, H. B., E. J. List, R. C. Y. Koh, J. Imberger, and N. H. Brooks (1979), *Mixing in Inland and Coastal Waters*, 483 pp., Elsevier, New York.

Johansen, O. (2000), DeepBlow—A Lagrangian plume model for deep water blowouts, *Spill Sci. Technol. Bull.*, *6*, 103–111.

Kobus, H. E. (1968), Analysis of the flow induced by air-bubble systems, paper presented at the 11th Coastal Engineering Conference, Am. Soc. of Civ. Eng., London.

Laureshen, C. J., and R. D. Rowe (1987), Modeling of plane bubble plumes, paper presented at the 24th National Heat Transfer Conference and Exhibition, Am. Soc. of Mech. Eng., Pittsburgh, Pa., 9–12 Aug.

Lemckert, C. J., and J. Imberger (1993), Energetic bubble plumes in arbitrary stratification, *J. Hydraul. Eng.*, *119*, 680–703.

McDougall, T. J. (1978), Bubble plumes in stratified environments, *J. Fluid Mech.*, *85*, 655–672.

McGinnis, D. F., and J. C. Little (1998), Bubble dynamics and oxygen transfer in a Speece cone, *Water Sci. Technol.*, *37*, 285–292.

McGinnis, D. F., and J. C. Little (2002), Predicting diffused-bubble oxygen transfer rate using the discrete-bubble model, *Water Res.*, *36*, 4627–4635.

McGinnis, D. F., J. C. Little, and A. Wuest (2001), Hypolimnetic oxygenation: Coupling bubble-plume and reservoir models, paper presented at Asian Waterqual 2001: First IWA Asia-Pacific Regional Conference, Int. Water Assoc., Fukuoka, Japan, 12–15 Sept.

McGinnis, D. F., A. Lorke, A. Wüest, A. Stöckli, and J. C. Little (2004), Interaction between a bubble plume and the near field in a stratified lake, *Water Resour. Res.*, *40*, W10206, doi:10.1029/2004WR003038.

Milgram, J. H. (1983), Mean flow in round bubble plumes, *J. Fluid Mech.*, *133*, 345–376.

Peterson, M. J., G. F. Cada, M. J. Sale, and G. K. Eddlemon (2003), Regulatory approaches for addressing dissolved oxygen concerns at hydropower facilities, 38 pp., U.S. Dep. of Energy Off. of Energy Efficiency and Renewable Energy, Idaho Falls, Idaho.

Rayyan, F., and R. E. Speece (1977), Hydrodynamics of bubble plumes and oxygen absorption in stratified impoundments, *Prog. Water Technol.*, *9*, 129–142.

Sahoo, G. B., and D. Luketina (2003), Modeling of bubble plume design and oxygen transfer for reservoir restoration, *Water Res.*, *37*, 393–401.

Schladow, S. G. (1992), Bubble plume dynamics in a stratified medium and the implications for water quality amelioration in lakes, *Water Resour. Res.*, *28*, 313–321.

Shang, E. H. H., R. M. K. Yu, and R. S. S. Wu (2006), Hypoxia affects sex differentiation and development, leading to a male-dominated population in zebrafish (Danio rerio), *Environ. Sci. Technol.*, *40*, 3118–3122.

Singleton, V. L., and J. C. Little (2005), Linear bubble plume model for hypolimnetic oxygenation: Full-scale evaluation and sensitivity analysis, paper presented at 9th Workshop on Physical Processes in Natural Waters, Lancaster Univ., Lancaster, UK, 4–6 Sept.

Singleton, V. L., and J. C. Little (2006), Designing hypolimnetic aeration and oxygenation systems: A review, *Environ. Sci. Technol.*, *40*(24), 7512–7520, doi:10.1021/es060069s.

Wilkinson, D. L. (1979), Two-dimensional bubble plumes, *J. Hydraul. Div. Am. Soc. Civ. Eng.*, *105*, 139–154.

Wüest, A., N. H. Brooks, and D. M. Imboden (1992), Bubble plume modeling for lake restoration, *Water Resour. Res.*, *28*, 3235–3250.

Zheng, L., P. D. Yapa, and F. Chen (2002), A model for simulating deep-water oil and gas blowouts: I. Theory and model formulation, *J. Hydraul. Res.*, *41*, 339–351.

———————————

P. Gantzer, J. C. Little, and V. L. Singleton, Department of Civil and Environmental Engineering, Virginia Polytechnic Institute and State University, 418 Durham Hall, Blacksburg, VA 24061-0246, USA. (jcl@vt.edu)

Exhibit E

CARBON DIOXIDE IN WATER AND SEAWATER: THE SOLUBILITY OF A NON-IDEAL GAS

R.F. WEISS

Scripps Institution of Oceanography, University of California at San Diego, La Jolla, Calif. 92037 (U.S.A.)

ABSTRACT

Weiss, R.F., 1974. Carbon dioxide in water and seawater: the solubility of a non-ideal gas. Mar. Chem., 2: 203—215.

New measurements of the solubility of carbon dioxide in water and seawater confirm the accuracy of the measurements of Murray and Riley, as opposed to those of Li and Tsui. Corrections for non-ideal behavior in the gas phase and for dissociation in distilled water are required to calculate solubility coefficients from these sets of data. Equations for the solubilities of real gases are presented and discussed. Solubility coefficients for carbon dioxide in water and seawater are calculated for the data of Murray and Riley, and are fitted to equations in temperature and salinity of the form used previously to fit the solubilities of other gases.

INTRODUCTION

Until very recently, direct determinations of the solubility of CO_2 in seawater have been limited to a few measurements of Krogh (1904). Most authors have preferred to use approximations based on the solubility of CO_2 in aqueous sodium chloride solutions. Buch et al. (1932) prepared tables of seawater CO_2 solubilities from the Bohr (1899) data for sodium chloride solutions, using the assumption that the effect of sea salt on the solubility is equal to the effect of an equal weight of sodium chloride. Lyman (1957) refined this assumption by considering the salting-out of the various constituents of sea salt, suggesting that the Buch et al. values may be about 0.5% too high.

The lack of direct measurements of CO_2 solubility in seawater has recently been alleviated by two independent sets of data: those of Li and Tsui (1971), determined by infrared analysis, and those of Murray and Riley (1971), determined gravimetrically. Unfortunately, the agreement between these sets of measurements is poor. Whereas the data of Li and Tsui support the values assumed by Buch et al., the solubility data of Murray and Riley are as much as 3.8% lower than those of Li and Tsui at higher temperatures and salinities. The agreement is better at lower temperatures and in distilled water, so that

the differences cannot be expressed either as a constant offset or as a constant factor.

In hopes of resolving these discrepancies, it was decided to make several independent measurements of CO_2 solubility. If it could be shown that a few accurate measurements covering a wide range of temperature and salinity were consistently in close agreement with one of the two sets of data, this would provide strong support for the accuracy of that set at all measured temperatures and salinities.

The second objective of this work was the fitting of the best CO_2 solubility data to an equation in temperature and salinity of the form used previously to fit the solubilities of N_2, O_2, and Ar (Weiss, 1970), He and Ne (Weiss, 1971a), H_2 (Crozier and Yamamoto, 1974), and Kr (Weiss and Kyser, in preparation). CO_2 is many times more soluble than any of the gases treated previously, and in the gas phase its departures from the ideal gas approximation are large compared to the accuracy with which its solubility can be measured. Therefore, before the use of such equations is justified, it is necessary to use Henry's law for real gases and to test its validity over a range of partial pressures of CO_2. Also, it is necessary to test the validity of the logarithmic Setchénow salting-out relation (Weiss, 1970, 1971b) for CO_2 in seawater.

Both Li and Tsui (1971), and Murray and Riley (1971), noted that their measurements would be affected by the dissociation of dissolved hydrated CO_2 to form bicarbonate, and accordingly they acidified their seawater samples to a sufficiently low pH so that this effect could be neglected. However, both studies failed to take this effect into account for their distilled-water measurements, which were made without acidification. Although this effect cancels in direct comparisons between the two sets of measurements, the proper use of Henry's law and of the Setchénow relation requires that the data be corrected for dissociation.

All distilled water CO_2 solubility data discussed in the following sections have been corrected for dissociation using the following approximation:

$$[CO_2] = [\Sigma CO_2] - \sqrt{K_1' \, [\Sigma CO_2]} \tag{1}$$

where $[CO_2]$ is the sum of the concentrations of dissolved CO_2 and undissociated hydrated CO_2, $[\Sigma CO_2]$ is the sum of the concentrations of all dissolved CO_2 species as measured in the solubility experiment, and K_1' is the first apparent dissociation constant at the temperature of the measurement.[*1] Solubilities measured in distilled water for $p_{CO_2} \simeq 1$ atm are thus reduced by $\sim 0.18\%$ at $0°C$, to $\sim 0.46\%$ at $40°C$.

HENRY'S LAW AND REAL GASES

King (1969, ch.4) presents an excellent and thorough discussion of Henry's law and its application to real gases over a wide range of pressures. By ex-

---

[*1] Values of K_1' were calculated according to Harned and Davis (1943, eq.15):
$\log_{10} K_1' = -3404.71/T + 14.8435 - 0.032786 \, T$.

pressing the activity of the solute in the gas phase by its fugacity, and by making the appropriate thermodynamic correction for the expansion of the solution by the dissolved gas, the "modified Henry's law equation" is obtained:

$$f_i = Q_i x_i \exp(P\bar{v}_i/RT) \tag{2}$$

where f_i is the fugacity of gas i, x_i is the mole fraction of i in solution, $\bar{v}_i$ is the partial molal volume of i in solution, R is the gas constant, T is the absolute temperature, P is the total pressure at the liquid-gas interface, and Q_i, the modified Henry's law constant for i, is a function only of the temperature and the nature of the solvent.

Conveniently, King uses the CO_2—water system as an example to illustrate the application of eq.2. Using literature data, with special emphasis on the work of Wiebe and Gaddy (1939; 1940), King (1969, pp.219—220) demonstrates that eq.2 holds over the entire CO_2-pressure range from zero to several hundred atmospheres, at a number of different temperatures.[2] The use of the modified form of Henry's law to calculate CO_2 solubilities over wide ranges of total pressures and CO_2 partial pressures, based on accurate solubility measurements made at pressures near 1 atm, is therefore well justified.[3] This is particularly germane to studies dealing with the solubility of natural levels of atmospheric CO_2.

In treating the solution of atmospheric gases in natural waters, it is convenient to express the solubility in terms of the Bunsen coefficient β, thereby avoiding the problem of evaluating the mole fraction of the gas in mixed solvents such as seawater. The Bunsen coefficient is defined here as the volume of gas (STP) absorbed per unit volume of the *solution*, at the temperature of the measurement, when the total pressure and the fugacity are both 1 atm.[4] This is preferable to the usual definition of β for ideal gases, in which the *partial* pressure is set at 1 atm and the *total* pressure is not specified, because the total pressure is required to define the system (see eq.2). Thus, C_i, the volume (STP) of gas i dissolved in a unit volume of *solution* at the temperature of the measurement, is given by the relation:

$$C_i = \beta_i f_i \exp[(1 - P)\bar{v}_i/RT] \tag{3}$$

where:

$$\beta_i = Q_i^{-1} V_i^{\dagger} \rho N \exp(-\bar{v}_i/RT) \tag{4}$$

and $V_i^{\dagger}$ is the volume of one mole of the real gas i at STP, ρ is the density of the *solution*, N is the number of moles in a unit weight of *solvent*, and P is in atmospheres. Since the solubility of most gases ($\bar{v} \cong 30$ cm^3/mole) is decreased

---

[2] Note that helium solubility measurements by these workers are in excellent agreement with recent microgasometric data (Weiss, 1971a).

[3] A more detailed discussion of CO_2 solubility as a function of pressure is given in the Appendix.

[4] Pressures are given here in atmospheres because of the widespread use of this unit to define standard states. Atmospheres may be converted to bars (10^5newtons/m^2), the more fundamental unit commonly used in high-pressure work, by multiplying by 0.986923.

by only ~0.15% per atmosphere increase in total pressure, the small deviations from 1 atm total pressure which are encountered in many natural conditions may be neglected, thereby reducing the exponential term in eq.3 to unity.

In the special case of CO_2, solubilities are generally used in calculations of chemical equilibria and are therefore best given in molar (moles/l of solution) or gravimetric (moles/kg of solution) units:

$$[CO_2] = K_0 f_{CO_2} \exp[(1 - P)\bar{v}_{CO_2}/RT] \tag{5}$$

where the constant K_0 equals $\beta/V^\dagger$ in molar units (moles/l · atm) or $\beta/\rho V^\dagger$ in gravimetric units (moles/kg · atm). Again, the exponential term may be taken as unity at total pressures near 1 atm.

In the following discussions, gas volumes and fugacity-pressure corrections are based on the virial equation of state. The appropriate expansions are carried only as far as the second virial coefficient $B(T)$, since the terms containing the third virial coefficient were always found to be negligible (~10^{-5}). Values of $B(T)$ in cm^3/mole, for CO_2 (Sengers et al., 1971) in the range 265—320°K, are well represented by a power series:

$$B(T) = - 1636.75 + 12.0408\ T - 3.27957 \cdot 10^{-2}\ T^2 + 3.16528 \cdot 10^{-5} T^3 \tag{6}$$

Thus, for the pure gas (neglecting the small contribution of water vapor), the solubility measurements discussed in the following sections have been corrected using the approximations (Guggenheim, 1967, pp.91 and 97):

$$V(P,T) = V^* (P,T) + B(T) \tag{7}$$

and:

$$\ln(f/P) = B(T) P/RT \tag{8}$$

where V is the volume of one mole of the real gas, and V^* is the volume of one mole of ideal gas.

In most natural applications which do not require accuracies greater than ~0.7%, the fugacity in eq.4 may be taken as equal to the partial pressure. However, if greater accuracy is desired, the fugacity must be calculated. For a nearly pure gas phase, eq.8 will suffice, but for multi-component gas phases, such as CO_2 in air, it is necessary to calculate fugacity in the mixture.

Useful equations for the calculation of fugacities in binary mixtures are given by Guggenheim (1967, pp.175—177):

$$f_1 = x_1 P \exp[(B_{11} + 2x_2^2 \delta_{12}) P/RT] \tag{9}$$

where the subscripts 1 and 2 refer to the two components of the mixture, x is the mole fraction, and B_{11} is the second virial coefficient of the pure gas 1. The quantity δ_{12} is defined by:

$$B_{12} = \frac{1}{2} (B_{11} + B_{22}) + \delta_{12} \tag{10}$$

where B_{12} is the cross virial coefficient for interactions between gas 1 and gas 2 molecules, and B_{11} and B_{22} refer to the pure gases 1 and 2, respectively. In addition to the binary mixtures, equations 8 and 9 may also be applied to mixtures of CO_2 in air when $x_{CO_2} \ll 1$.

Few direct measurements of cross-virial coefficients exist, so that the quantity δ_{12} must be evaluated from theoretical considerations. The quantity δ_{CO_2-air} has been evaluated from the Lennard-Jones (6-12) potential model following the method of Hirschfelder, Curtiss and Bird (1954, pp.166—170). The results in cm³/mole for the temperature range 273 to 313°K are well represented by the linear relation:

$$\delta_{CO_2-air} = 57.7 - 0.118\,T \tag{11}$$

The magnitude of this correction, as opposed to assuming $\delta = 0$ (Lewis and Randall rule), is about 0.2% in the overall solubility calculation, or about one third of the total deviation from ideal gas behavior.

Calculations of CO_2 fugacity using the virial equation of state are valid to within 0.1% for total pressures up to ~10 atm. Higher pressures require the use of more sophisticated equations of state, such as the Benedict, Webb and Rubin (1940; 1942) equation, which may be used to at least 500 atm (see Appendix).

DATA FITTING

The corrected data of Murray and Riley (1971) were fitted to the same equation in temperature and salinity which has been used to fit the solubilities of many other gases (see Introduction). This equation is derived from the integrated van't Hoff equation and the logarithmic Setchénow salinity dependence, and has the form (Weiss, 1970):

$$\ln K_0 = A_1 + A_2(100/T) + A_3 \ln(T/100) + \\ S\%_0[B_1 + B_2(T/100) + B_3(T/100)^2] \tag{12}$$

where K_0 may be expressed either in moles/l · atm, referring to a liter of solution at the temperature of the measurement and an atmosphere *fugacity* in the gas phase, or in moles/kg · atm, referring to a kilogram of solution. The A's and B's are constants, T is the absolute temperature, and $S\%_0$ is the salinity in parts per thousand. The method of fitting the data, and the conditions for justification of the Setchénow equation and the number of terms used in the expansion, are discussed elsewhere (Weiss, 1970).

The corrected Murray and Riley CO_2 data showed good agreement with the equations at all stages of the fitting procedure. The data show a root-mean-square deviation from the final fitted equation of $1.4 \cdot 10^{-4}$ moles/l · atm in K_0, or about 0.3%. Agreement with the Setchénow relation is shown in Fig.1 by the random nature of the deviations as a function of salinity for each measured isotherm. The fitted values of the constants in eq.12 are listed in Table I for K_0 in molar and in gravimetric units. Values of K_0 at various temperatures
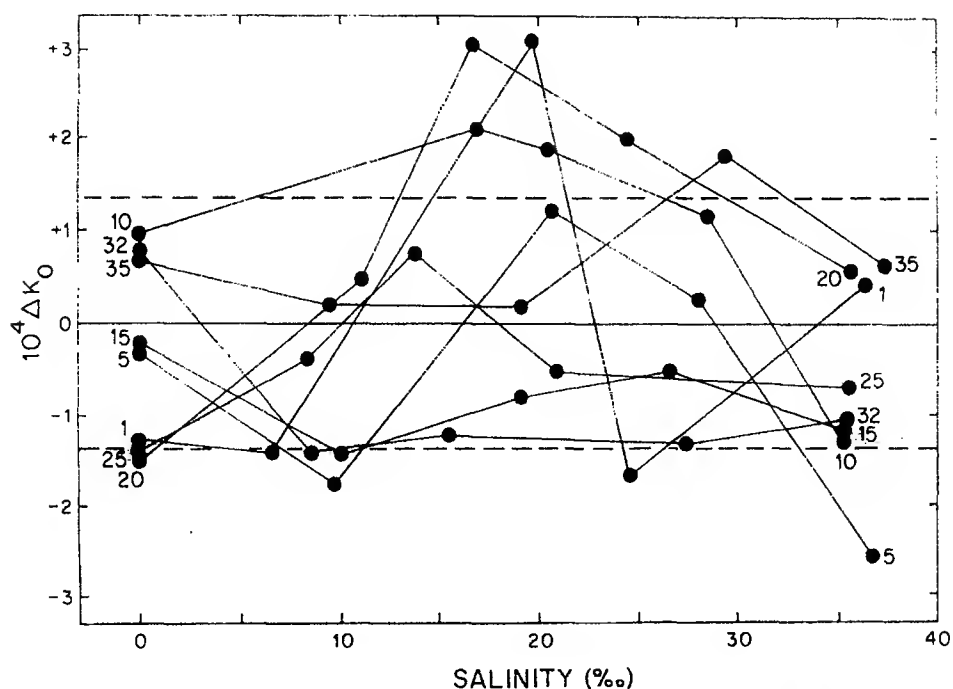
208

Fig.1. Deviations of the Murray and Riley (1971) CO_2 solubility data (corrected for dissociation and non-ideality) in moles/l·atm from the fitted curve (eq.12), plotted against salinity. Measurements made at constant temperature are connected by lines, and are labeled to the nearest °C. The dashed lines show ±1 standard deviation.

and salinities calculated from these constants are listed in Tables II and III.

Salting-out constants (the B's in eq.12) were also determined for the solubility of CO_2 in aqueous NaCl solutions using the data of Bohr (1899), corrected for dissociation. With NaCl concentration expressed as weight percent in solu-

TABLE I

Constants for the calculation of the solubility of CO_2 in molar and gravimetric units according to eq.12

| | Units of K_0 | |
	moles/l·atm	moles/kg·atm
A_1	−58.0931	−60.2409
A_2	90.5069	93.4517
A_3	22.2940	23.3585
B_1	0.027766	0.023517
B_2	−0.025888	−0.023656
B_3	0.0050578	0.0047036

TABLE II

The solubility coefficient K_0 (10^{-2} moles/l·atm)

	Salinity (‰)								
T(°C)	0	10	20	30	34	35	36	38	40
−1	—	—	7.273	6.903	6.760	6.724	6.689	6.620	6.551
0	7.758	7.364	6.990	6.635	6.498	6.465	6.431	6.364	6.298
1	7.458	7.081	6.723	6.382	6.251	6.219	6.187	6.123	6.060
2	7.174	6.813	6.469	6.143	6.017	5.986	5.955	5.894	5.833
3	6.905	6.558	6.229	5.916	5.795	5.766	5.736	5.677	5.619
4	6.650	6.317	6.001	5.701	5.585	5.557	5.528	5.472	5.416
5	6.408	6.088	5.785	5.497	5.386	5.358	5.331	5.277	5.223
6	6.178	5.871	5.580	5.303	5.196	5.170	5.144	5.092	5.040
8	5.751	5.469	5.200	4.945	4.846	4.822	4.797	4.749	4.702
10	5.366	5.105	4.857	4.621	4.529	4.507	4.485	4.440	4.396
12	5.017	4.776	4.546	4.327	4.243	4.222	4.201	4.160	4.119
14	4.700	4.477	4.264	4.062	3.983	3.964	3.945	3.906	3.869
16	4.412	4.205	4.008	3.820	3.747	3.729	3.712	3.676	3.641
18	4.149	3.958	3.775	3.600	3.533	3.516	3.499	3.466	3.434
20	3.910	3.732	3.562	3.400	3.337	3.322	3.306	3.275	3.245
22	3.691	3.526	3.368	3.217	3.158	3.144	3.130	3.101	3.073
24	3.491	3.337	3.190	3.050	2.995	2.982	2.968	2.942	2.915
26	3.307	3.164	3.027	2.897	2.846	2.833	2.821	2.796	2.771
28	3.138	3.005	2.878	2.756	2.709	2.697	2.685	2.662	2.639
30	2.983	2.859	2.741	2.627	2.583	2.572	2.561	2.540	2.518
32	2.840	2.725	2.615	2.509	2.468	2.457	2.447	2.427	2.407
34	2.708	2.601	2.498	2.400	2.361	2.352	2.342	2.323	2.305
36	2.587	2.487	2.391	2.299	2.263	2.254	2.246	2.228	2.211
38	2.474	2.382	2.292	2.207	2.173	2.165	2.157	2.140	2.124
40	2.370	2.284	2.201	2.121	2.090	2.082	2.074	2.059	2.044

tion, and K_0 in moles/l·atm, the constants are: $B_1 = -0.68330$, $B_2 = 0.40911$, $B_3 = -0.064989$. Averaged over the temperature range 0—40°C, K_0 is 0.8% higher in a 3.6% NaCl solution than K_0 in seawater of 36‰ salinity, calculated from the salting-out constants in Table I. This difference probably lies within the error of the Lyman (1957) prediction that K_0 in the NaCl solution would be 0.5% higher.

EXPERIMENTAL METHOD

Measurements of CO_2 solubility were carried out by the microgasometric technique used previously to measure He and Ne solubilities (Weiss, 1971a). High-purity CO_2 (certified ≥ 99.99%) was supplied by Matheson Gas Products and gas chromatographic analysis showed < 0.01% air contamination. Because of the high solubility of CO_2 compared to He and Ne, the amount of degassed

water added to the equilibration chamber was reduced to about one third of the total gas volume. Under these conditions, equilibration was extremely rapid (first-order rate constant $\tau \cong 30$ sec) so that the 6—10 minutes allowed for equilibration were more than adequate. Permeation of CO_2 through the indicator drop was rapid, and required that the chamber above the drop be filled with pure CO_2 prior to each equilibration. With this procedure, no drift in the indicator drop could be detected over a period of 1 h.

In order to obtain the most direct comparisons with the work of Murray and Riley and of Li and Tsui, chemical procedures similar to their's were followed. Distilled water measurements were performed without acidification and the corrections for dissociation were made. Surface seawater, collected at La Jolla and evaporated to increase its salinity by $\sim 2\%$, was passed through a 0.45μ filter, poisoned with 1 mg/liter $HgCl_2$, and its salinity determined to $\pm 0.004\%$ by an inductive salinometer. Sulfuric acid ($\sim 2N$) was then added to bring the pH to 2.2 and the salinity was adjusted by gravimetric determination of the amount of H_2O added in the acid solution. Following Murray and

TABLE III

The solubility coefficient K_0 $(10^{-2}$ moles/kg$\cdot$atm)

Salinity (‰)

T (°C)	0	10	20	30	34	35	36	38	40
−1	—	—	7.158	6.739	6.579	6.539	6.500	6.422	6.345
0	7.758	7.305	6.880	6.479	6.325	6.287	6.249	6.175	6.101
1	7.458	7.024	6.616	6.232	6.085	6.048	6.012	5.941	5.870
2	7.174	6.758	6.367	5.999	5.857	5.822	5.788	5.719	5.651
3	6.904	6.506	6.131	5.777	5.642	5.608	5.575	5.509	5.444
4	6.649	6.267	5.907	5.568	5.438	5.405	5.374	5.310	5.248
5	6.407	6.040	5.695	5.369	5.244	5.213	5.182	5.122	5.062
6	6.177	5.825	5.493	5.180	5.060	5.031	5.001	4.943	4.885
8	5.752	5.427	5.120	4.831	4.720	4.693	4.666	4.612	4.558
10	5.367	5.067	4.784	4.516	4.413	4.388	4.363	4.313	4.263
12	5.019	4.741	4.479	4.231	4.136	4.112	4.089	4.042	3.997
14	4.703	4.446	4.202	3.972	3.884	3.862	3.840	3.797	3.755
16	4.416	4.177	3.951	3.738	3.655	3.635	3.615	3.575	3.536
18	4.155	3.933	3.723	3.524	3.448	3.429	3.410	3.373	3.336
20	3.916	3.710	3.515	3.330	3.258	3.241	3.223	3.189	3.154
22	3.699	3.507	3.325	3.152	3.086	3.069	3.053	3.021	2.989
24	3.499	3.321	3.151	2.990	2.928	2.912	2.897	2.867	2.837
26	3.317	3.150	2.992	2.841	2.783	2.769	2.755	2.727	2.699
28	3.149	2.994	2.846	2.705	2.651	2.638	2.624	2.598	2.572
30	2.995	2.850	2.712	2.580	2.530	2.517	2.505	2.480	2.455
32	2.854	2.718	2.589	2.466	2.418	2.406	2.395	2.372	2.349
34	2.723	2.596	2.476	2.360	2.316	2.305	2.294	2.272	2.250
36	2.603	2.484	2.371	2.263	2.221	2.211	2.201	2.180	2.160
38	2.492	2.381	2.275	2.174	2.134	2.125	2.115	2.096	2.077
40	2.389	2.285	2.186	2.091	2.054	2.045	2.036	2.018	2.000

Riley (1971), the effect of the added H_2SO_4 molecules on the salinity was neglected as being insignificant with respect to altering the solubility of CO_2. The water was degassed using the same vacuum extraction method as in the previous work (Weiss, 1971a).

The results were calculated in the same manner as previous microgasometric measurements, except that the corrections for non-ideal behavior discussed in the foregoing section were applied. The correction for the expansion of the aqueous phase during equilibration was made using a partial molal volume of 32.3 cm^3 per mole of CO_2 (see Appendix). The overall accuracy of these CO_2 solubility measurements is estimated as ±0.2%.

RESULTS AND CONCLUSIONS

The microgasometric experimental values for K_0 in moles/l· atm at several temperatures and salinities, corrected for dissociation and non-ideality, are given in Table IV. Deviations of the microgasometric results from the fitted Murray and Riley data, plotted in Fig.2, show excellent agreement without systematic deviations. At each of the three different temperature and salinity conditions, the range of microgasometric points brackets the fitted curve. The average deviation of all the measured points is $1.5 \cdot 10^{-5}$ moles/l· atm, and the root-mean-square deviation is $1.2 \cdot 10^{-4}$ moles/l· atm. Curves for the deviations of the data of Li and Tsui, taken from their equations (1) and (2a) after correction for dissociation and non-ideality, are also plotted in Fig.2. Although their fresh-water measurements are in reasonably good agreement, the seawater data of Li and Tsui show large deviations from the fitted Murray and Riley

TABLE IV

Experimental CO_2 solubilities: microgasometric determinations of K_0 in moles/l· atm

Salinity (‰)	t (°C)	$K_0 \cdot 10^2$
0.0	20.61	3.848
0.0	20.63	3.843
0.0	20.60	3.867
0.0	20.59	3.834
0.0	20.61	3.840
35.330	6.59	5.071
35.330	6.60	5.063
35.330	6.60	5.068
35.330	6.59	5.041
35.330	20.62	3.245
35.330	20.63	3.272
35.330	20.63	3.245
35.330	20.63	3.255
35.330	20.63	3.254
35.330	20.63	3.252

212

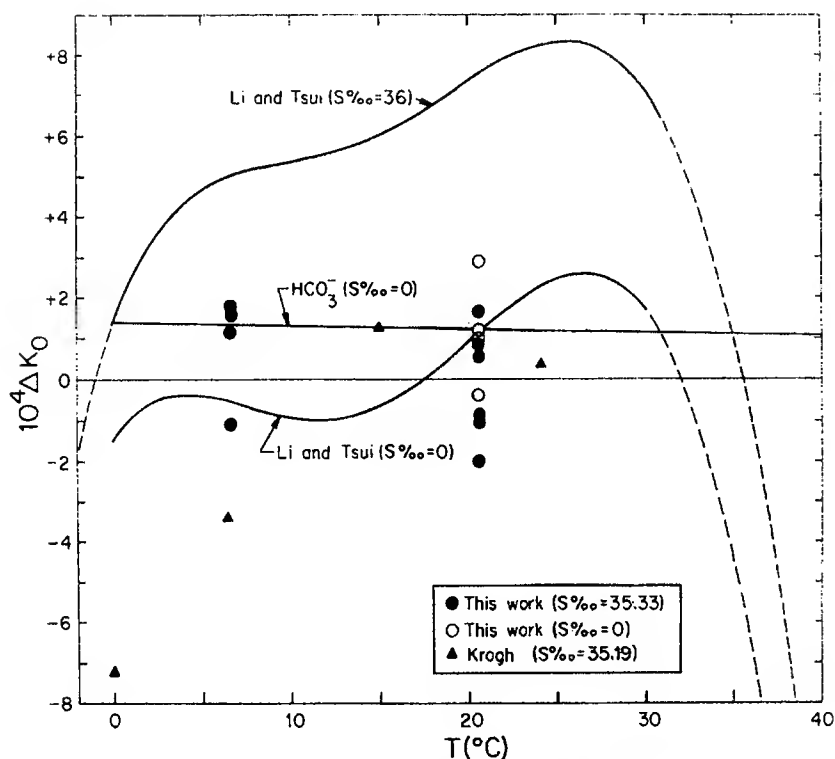Fig.2. Deviations of various CO_2 distilled water and seawater solubility data in moles/l· atm from the fit to the corrected data (see text) of Murray and Riley (1971), plotted against temperature. The curves for Li and Tsui (1971) are taken from their equations (1) and (2a), and, like the data of Krogh (1904), have been corrected for non-ideality and dissociation: the dashed portions of these curves represent the extrapolation of their equations beyond the range of their measurements. The magnitude of the error caused by dissociation for measurements made in distilled water at $pCO_2 = 1$ atm is shown by the line labeled "HCO_3^-".

data. Fig.2 also shows the corrected data of Krogh (1904), which agree well with Murray and Riley at the higher temperatures.

The microgasometric results provide independent confirmation of the accuracy of the CO_2 solubility measurements of Murray and Riley (1971) and show the measurements of Li and Tsui (1971) to be in error by as much as ~4% at the higher temperatures and salinities. The data of Murray and Riley, corrected for the effects of non-ideal gas behavior and for dissociation in the distilled water measurements, are well represented by the Setchénow and integrated van't Hoff equations used previously to fit the solubilities of several other comparatively ideal gases. Thus, CO_2 solubilities calculated from eq.12, using the constants in Table I, are believed to provide the most accurate values in the literature, with an overall accuracy estimated at $\pm 1 \cdot 10^{-4}$ moles/l· atm or about 0.2%. The solubility of CO_2 obeys the modified form of Henry's law

(eq.2) and it is therefore necessary to take account of the total pressure, as well as to calculate the fugacity of CO_2 in the gas phase, if full use is to be made of the accuracy of these solubility data.

ACKNOWLEDGEMENTS

APPENDIX

Carbon dioxide solubility at high pressures

At pressures greater than ~10 atm, CO_2 fugacities calculated from the virial equation of state, even when carried to the third virial coefficient, show large deviations from the literature values (Deming and Deming, 1939). Far better results are obtained with the Benedict, Webb and Rubin equation of state for pure substances (Benedict et al., 1940) and for mixtures (Benedict et al., 1942), which fit the observed $p-V-T$ data up to densities of twice the critical density. In the following discussion, Benedict, Webb and Rubin equation constants for pure CO_2 are taken from the Bishnoi and Robinson (1971)[*5] volume-dependent fit to the compressibility data of Reamer et al. (1944). Because the Benedict, Webb and Rubin equation is an explicit function of V and T, the solution for specific values of P is obtained by the method of successive approximations.

Fig.3 shows the distilled water CO_2 solubility data of Wiebe and Gaddy (1940) for the temperature range 12—40°C and the pressure range 25—500 atm, plotted as $\ln(f/x)$ against the total pressure P. Fugacities were calculated assuming a pure CO_2 phase at a pressure of P minus the vapor pressure of water. Negligible error was introduced by this approximation because of the small fraction of water vapor in the CO_2-rich phase. The straight lines plotted at each of the six experimental temperatures were fitted to the Wiebe and Gaddy data by the method of least-squares.

According to eq.2, if $\bar{v}$ is independent of P, then $\ln(f/x)$ plotted as a function of P at constant T should give a straight line with intercept $\ln Q$ and slope $(\bar{v}/RT)$. This relationship is strongly supported by the experimental data as shown in Fig.3. The root-mean-square deviation of the Wiebe and Gaddy measurements about the six straight lines is ~0.8%, and there is no systematic indication of departure from linearity. The slopes of these lines correspond to remarkably constant values of $\bar{v}$, with a mean of 32.3 cm³/mole and a standard deviation of 0.5 cm³/mole. Thus, the data show no significant variation in $\bar{v}$, either as a function of T over the range 12—40°C, or as a function of P up to 500 atm.

Results of the fit to the corrected Murray and Riley distilled water data (eq.12), measured at 1 atm, are also plotted in Fig.3. The overall agreement with the Wiebe and Gaddy data is good, although there may be a systematic difference at 12°C (the Wiebe and Gaddy data also show the greatest scatter at this temperature). On the average, the solubilities at 1 atm obtained from the linear fits to the Wiebe and Gaddy data are 0.4% lower in β (or higher in Q), and show a 2% root-mean-square difference.

[*5] The constants, converted from English to metric units (atm, l, mole, °K): $A_0 = 1.9521940$, $B_0 = 0.033065171$, $C_0 = 170449.55$, $a = 0.25264437$, $b = 6.6041298 \cdot 10^{-3}$, $c = 19592.012$, $\alpha = 4.7117009 \cdot 10^{-5}$, $\gamma = 4.3414415 \cdot 10^{-3}$, $R = 0.08205601$.
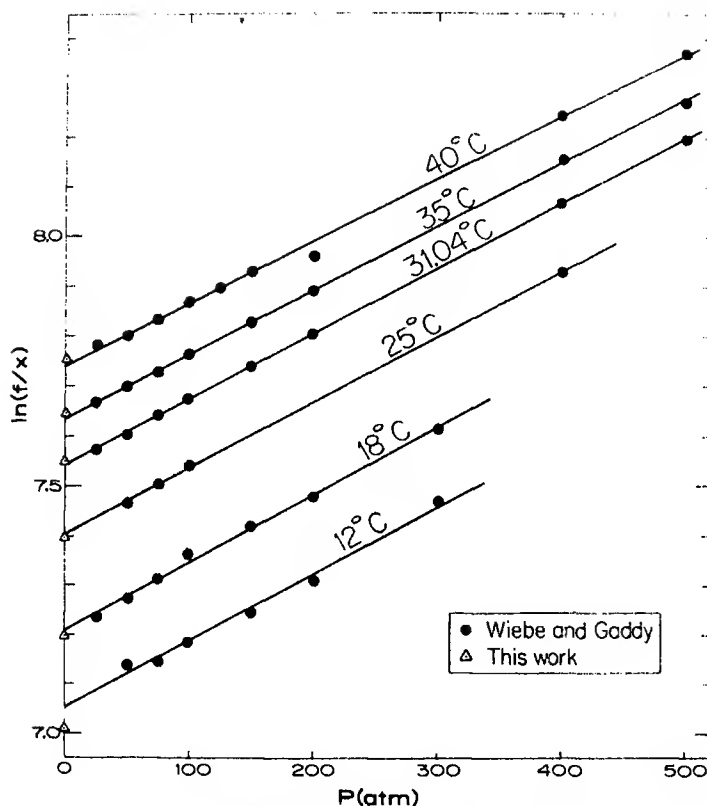
214

Fig.3. High-pressure distilled water CO_2 solubility data of Wiebe and Gaddy (1940) plotted as the logarithm of the fugacity to mole fraction ratio, against the total pressure. Solubilities at 1 atm calculated from eq.12 are plotted for the temperatures of the Wiebe and Gaddy measurements.

In summary, the high-pressure solubility data show that the modified form of Henry's law (eqs.2, 3, or 5) is valid for CO_2 in water over the entire pressure range of 0—500 atm, which corresponds to a dissolved CO_2 concentration range of 0—1.7 molar. Assuming that $\bar{v}$ for CO_2 is the same in seawater as in distilled water, as was shown by Enns et al. (1965) for O_2, the solubility of CO_2 in seawater at high pressures may also be calculated from these equations.

REFERENCES

Benedict, M., Webb, G.B. and Rubin, L.C., 1940. An empirical equation for the thermodynamic properties of light hydrocarbons and their mixtures. I. Methane, ethane, propane and n-butane. J. Chem. Phys., 8: 334—345

Benedict, M., Webb, G.B. and Rubin, L.C., 1942. An empirical equation for the thermodynamic properties of light hydrocarbons and their mixtures. II. Mixtures of methane, ethane, propane and n-butane. J. Chem. Phys., 10: 747—758

Bishnoi, P.R. and Robinson, D.B., 1971. An evaluation of methods for determining the parameters in the BWR equation of state using volumetric and heat capacity data. Can. J. Chem. Eng., 49: 642—650

Bohr, C., 1899. Definition und Methode zur Bestimmung der Invasions- und Evasions-coefficienten bei der Auflösung von Gasen in Flüssigkeiten. Werthe der genannten Constanten sowie der Absorptionscoefficienten der Kohlensäure bei Auflösung in Wasser und in Chlornatriumlösungen. Ann. Phys. Chem., 68: 500—525

Buch, K., Harvey, H.W., Wattenberg, H. and Gripenberg, S., 1932. Über das Kohlensäure-system in Meerwasser. Rapp. Cons. Explor. Mer, 79: 1—70

Crozier, T.E. and Yamamoto, S., 1974. The solubility of hydrogen in water, seawater and NaCl solutions. J. Chem. Eng. Data, 19: 242—244

Deming, W.E. and Deming, L.S., 1939. Some physical properties of compressed gases. VI. The fugacity of carbon dioxide. Phys. Rev., 56: 108—112

Enns, T., Scholander, P.F. and Bradstreet, E.D., 1965. The effect of hydrostatic pressure on gases dissolved in water. J. Phys. Chem., 69: 389—391

Guggenheim, E.A., 1967. Thermodynamics. North-Holland, Amsterdam, 5th ed., 390 pp.

Harned, H.S. and Davis, R., 1943. The ionization constant of carbonic acid in water and the solubility of carbon dioxide in aqueous salt solution from 0-50°. J. Am. Chem. Soc., 65: 2030—2037

Hirschfelder, J.O., Curtiss, C.F. and Bird, R.B., 1954. Molecular Theory of Gases and Liquids. Wiley, New York, N.Y., 1219 pp.

King, M.B., 1969. Phase Equilibrium in Mixtures. Pergamon, Oxford, 584 pp.

Krogh, A., 1904. On the tension of carbonic acid in natural waters and especially in the sea. Medd. om Grønland, 26: 331—405

Li, Y.H. and Tsui, T.F., 1971. The solubility of CO_2 in water and seawater. J. Geophys. Res., 76: 4203—4207

Lyman, J., 1957. Buffer Mechanism of Sea Water. Thesis, Univ. of California at Los Angeles, 196 pp.

Murray, C.N. and Riley, J.P., 1971. The solubility of gases in distilled water and seawater — IV. Carbon dioxide. Deep-Sea Res., 18: 533—541

Reamer, H.H., Olds, R.H., Sage, B.H. and Lacey, W.N., 1944. Phase equilibria in hydro-carbon systems. Methane-carbon dioxide system in the gaseous region. Ind. Eng. Chem., 36: 88—90

Sengers, J.M.H. Levelt, Klein, M. and Gallagher, J.S., 1971. Pressure—Volume—Tempera-ture Relationships of Gases — Virial Coefficients. U.S. N.B.S. Rept., U.S. Air Force Tech. Publ., AEDC-TR-71-39: 47 pp.

Weiss, R.F., 1970. The solubility of nitrogen, oxygen and argon in water and seawater. Deep-Sea Res., 17: 721—735

Weiss, R.F., 1971a. Solubility of helium and neon in water and seawater. J. Chem. Eng. Data, 16: 235—241

Weiss, R.F., 1971b. The effect of salinity on the solubility of argon in seawater. Deep-Sea Res., 18: 225—230

Wiebe, R. and Gaddy, V.L., 1939. The solubility in water of carbon dioxide at 50, 75 and 100°, at pressures to 700 atmospheres. J. Am. Chem. Soc., 61: 315—318

Wiebe, R. and Gaddy, V.L., 1940. The solubility of carbon dioxide in water at various temperatures from 12 to 40° and at pressures to 500 atmospheres. Critical phenomena. J. Am. Chem. Soc., 62: 815—817

Exhibit F

168

S7. Soule, H. M. *Trans. ASME*, **73**, 113, 112 (1951).

S8. Stringham, G. E., Simons, D. B., and Guy, H. P. *U. S. Geol. Surv. Prof. Pap.* **562-C** (1969).

T1. Taneda, S. *J. Phys. Soc. Jpn.* **11**, 302, 307 (1956).

T2. Torobin, L. B., and Gauvin, W. H. *Can. J. Chem. Eng.* **38**, 142, 153 (1960).

U1. Underwood, R. L. *J. Fluid Mech.* **37**, 95, 114 (1969).

V1. Van der Hegge Zijnen, B. G. *Appl. Sci. Res.* **A6**, 129, 140 (1956).

W1. Wadell, H. *J. Geol.* **41**, 310, 331 (1933).

W2. Wadell, H. *J. Franklin Inst.* **217**, 459, 460 (1934).

W3. Wehrman, O. H. *Phys. Fluids* **9**, 1285, 1286 (1966).

W4. Wieselsberger, C. *Phys. Z.* **23**, 219, 224 (1922).

W5. Willmarth, W. W., Hawk, N. E., and Harvey, R. L. *Phys. Fluids* **7**, 197, 208 (1964).

W6. Woo, S. W. Ph.D Thesis, McMaster Univ., Hamilton, Ontario, 1971.

Clift, R., et al., Bubble, Drops, and Particles, New York, NY, 1978

Chapter 7

Ellipsoidal Fluid Particles

I. INTRODUCTION

The conditions under which fluid particles adopt an ellipsoidal shape are outlined in Chapter 2 (see Fig. 2.5). In most systems, bubbles and drops in the intermediate size range (d_e typically between 1 and 15 mm) lie in this regime. However, bubbles and drops in systems of high Morton number are never ellipsoidal. Ellipsoidal fluid particles can often be approximated as oblate spheroids with vertical axes of symmetry, but this approximation is not always reliable. Bubbles and drops in this regime often lack fore-and-aft symmetry, and show shape oscillations.

II. FLUID DYNAMICS

A. AIR-WATER SYSTEMS

Because of their practical importance, water drops in air and air bubbles in water have received more attention than other systems. The properties of water drops and air bubbles illustrate many of the important features of the ellipsoidal regime.

1. Water Drops in Air

Numerous determinations of the terminal velocities of water drops have been reported. The most careful measurements are those by Gunn and Kinzer (G13) and Beard and Pruppacher (B4). Figure 7.1, derived from these results,* shows

*Results for Re < 300 were included in the data used to derive the "standard drag curve" in Chapter 5. Numerical results for spherical raindrops found for Re < 300 are also discussed in Chapter 5.
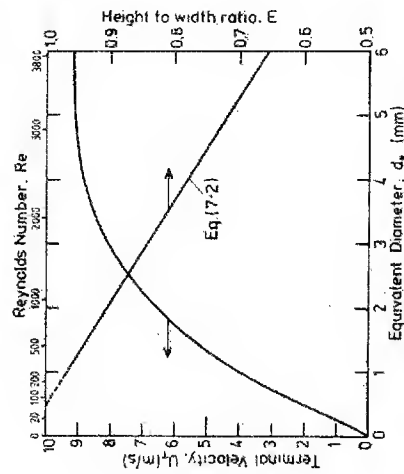
FIG. 7.1   Terminal velocity and aspect ratio of water drops falling freely in air at 20 C and 1 bar (B4, G13, P5).

terminal velocity and corresponding Reynolds number as a function of volume-equivalent diameter for water drops in air. Berry and Pranger (B7) and Beard (B3) give empirical polynomials describing the terminal velocity of drops in air, with Beard's equations covering a wider range of atmospheric conditions than the others. For water drops in air under normal atmospheric conditions at sea level, the simplest fit (B7), accurate within about 3% gives

$$Re = \exp[-3.126 + 1.013 \ln N_D - 0.01912(\ln N_D)^2] \qquad (7\text{-}1)$$
$$(2.4 < N_D < 10^7: 0.1 < Re < 3550)$$

where N_D is defined by Eq. (5-15). For $d_e \lesssim 1$ mm (Re $\lesssim 300$), deviations from a spherical shape and internal circulation are so small that the correlations for rigid spheres in Chapter 5 may be used to predict terminal velocities. For $d_e <$ 20 μm (B3), correction for noncontinuum effects must be made (see Chapter 10). Pitter and Pruppacher (P4) studied the motion of 200 to 350 μm water drops undergoing freezing.

Drops larger than about 1 mm in diameter are significantly nonspherical; the mean height to width ratio is approximated (P5) by:

$$E = 1.030 - 0.062 d_e \qquad (1 < d_e < 9 \text{ mml}). \qquad (7\text{-}2)$$

with d_e in mm. This ratio is plotted in Fig. 7.1. Figure 7.2 shows that deformation increases the drag coefficient above the value for a rigid sphere if C_D and Re are based on the volume-equivalent diameter d_e. The flattening of water drops at the front (lower) surface results from the increased hydrodynamic pressure there, while the rear has a more uniform hydrodynamic pressure and is therefore more rounded (M6). Blanchard (B9) discusses the popular misconception that raindrops fall with a teardrop shape. Figure 2.4(al shows a photograph of a water drop in air. Shapes are discussed in detail in Section D.
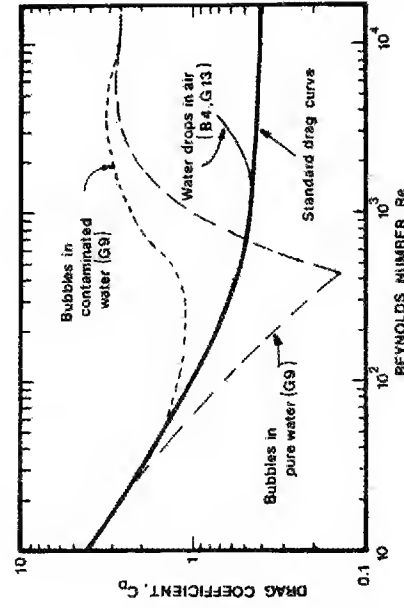
FIG. 7.2   Drag coefficient as function of Reynolds number for water drops in air and air bubbles in water, compared with standard drag curve for rigid spheres.

Water drops become unstable and tend to break up before they reach 1 cm in diameter (see Chapter 12). Drops approaching this size show periodic shape fluctuations of relatively low amplitude (J3, M4).

As for other types of fluid particle, the internal circulation of water drops in air depends on the accumulation of surface-active impurities at the interface (H9). Observed internal velocities are of order 1% of the terminal velocity (G4, P5), too small to affect drag detectably. Ryan (R6) examined the effect of surface tension reduction by surface-active agents on falling water drops.

2. Air Bubbles in Water

Experimental terminal velocities for air bubbles rising in water are presented in Fig. 7.3 for the ellipsoidal regime and adjacent parts of the spherical and spherical-cap regimes. Some of the spread in the data results from experimental scatter, but the greatest cause is surface contamination. For water drops in air, described in the previous section, surfactants have negligible effect on drag since κ is so high that internal circulation is small even in pure systems. For air bubbles in water, κ is so small that there is little viscous resistance to internal circulation, and hence the drag and terminal velocity are sensitive to the presence of surfactants.

The two curves in Fig. 7.3 are based on those given by Gaudin (G9) for distilled water and for water with surfactant added. The curves converge for small (spherical) bubbles, since even distilled water tends to contain sufficient surfactant to prevent circulation in this range (see Chapter 3), and for large (spherical-cap) bubbles, where surface tension forces cease to be important. Surface-active contaminants affect the rise velocity most strongly in the ellipsoidal range. Drag coefficients corresponding to these two curves appear in Fig. 7.2, and show that C_D for bubbles lies below the rigid sphere curve when
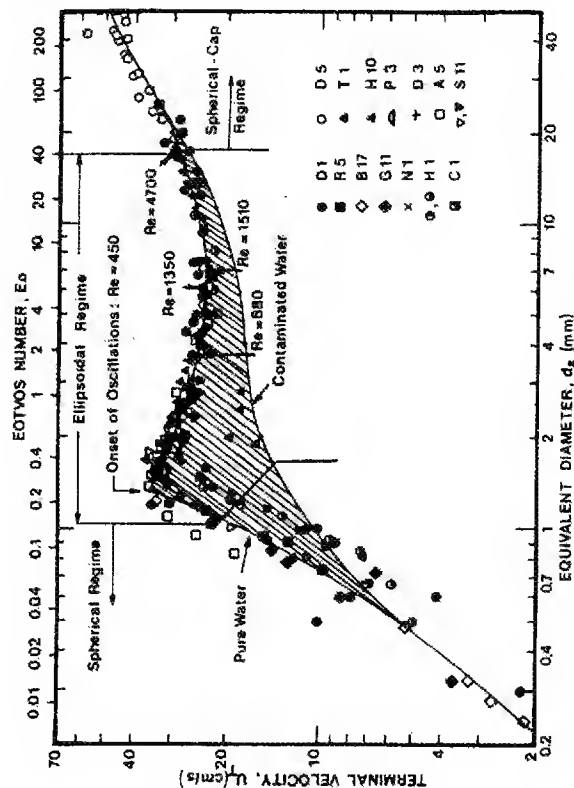
FIG. 7.3 Terminal velocity of air bubbles in water at 20 C.

internal circulation is present, but above it there is no internal circulation and the drag is dominated by deformation. For $d_e > 1.3$ mm, the uppermost (pure system) curve in Fig. 7.3 is approximated closely by

$$U_T = [(2.14\sigma/\rho d_e) + 0.505 g d_e]^{1/2}, \quad (7\text{-}3)$$

which is of the form suggested by a wave analogy (C2, M7).

Aybers and Tapucu (A4, A5) measured trajectories of air bubbles in water. When surface-active agents continue to accumulate during rise, the terminal velocity may never reach steady state (A4, B1) and may pass through a maximum (W4). Five types of motion were observed, listed in Table 7.1 with Re based on the maximum instantaneous velocity. Secondary motion of fluid par-

TABLE 7.1

Motion of Intermediate Size Air Bubbles Through Water at 28.5 C[a]

d_e (mm)	Re	E	Path
<1.3	<565	>0.8	Rectilinear
1.3 to 2.0	565 to 880	0.8 to 0.5	Helical
2.0 to 3.6	880 to 1350	0.5 to 0.36	Plane (zig-zag) then helical
3.6 to 4.2	1350 to 1510	0.36 to 0.28	Plane (zig-zag)
4.2 to 17	1510 to 4700	0.28 to 0.23	Rectilinear but with rocking

ticles, associated with wake phenomena, is discussed in greater detail in Section F. Lindt and De Groot (L8) give values of the Strouhal number for helical vortex shedding behind air bubbles in water.

B. TERMINAL VELOCITIES OF DROPS AND BUBBLES IN LIQUIDS

The generalized graphical correlation presented in Fig. 2.5 gives one method of estimating terminal velocities of drops and bubbles in infinite liquid media. For more accurate predictions, it is useful to have terminal velocities correlated explicitly in terms of system variables. To obtain such a correlation is especially difficult for the ellipsoidal regime where surface-active contaminants are important and where secondary motion can be marked.

1. Effect of Viscosity Ratio κ

It is general practice to ignore the effect of the viscosity of the internal fluid in correlations of terminal velocities. We recall from Chapter 3 that decreasing μ_p, all other factors remaining fixed, can at most cause a 50% change in U_T at low Re, and this change is seldom realized in practice due to the effect of surfactants. Hamielec (H2) showed that varying κ over a tenfold range had a small but noticeable effect for cyclohexanol drops in water with Re up to about 10. Figure 7.4 shows Re (Eo) for eight systems, all having virtually the same Morton

SYMBOL	REF	M×10^10	κ
○	K3	2.2	0.42
●	T4	2.3	1.80
▲	T5	2.3	19.8
□	T4	2.0	1.11
	T5	2.0	1.11
	T4	2.1	10.4
◇	K2	2.1	0.50
◆	K2	2.1	0.35

FIG. 7.4 Reynolds number as a function of Eotvos number for systems with essentially identical

Number (2.0 to 2.3×10^{-10}), but widely different values of κ (0.35 to 20). While the data exhibit some scatter, the observed dimensionless terminal velocities do not vary systematically with κ, but appear to reflect differences in system purity. Thorsen and coworkers (T4, T5) took greater care to purify their systems than the other authors and this is reflected in higher velocities. The internal fluid viscosity can be considered to be of secondary importance for systems in which no particular care has been taken to eliminate surfactants.

2. Effect of Surface-Active Contaminants

We may illustrate the effect of surfactants by comparing terminal velocities measured by different workers using the same system. Results for air bubbles in water have already been shown in Figs. 7.2 and 7.3. Results from six different studies on carbon tetrachloride drops falling through water are plotted in Fig. 7.5. The measured terminal velocities differ widely among different investigators, and one can only attribute these differences to differences in system purity. A number of workers have noted a strong influence of system purity on the drag or terminal velocity of ellipsoidal fluid particles [e.g. (E3, R1, S9, T1, T4, Z1)]. In a very careful study, Edge and Grant (E3) examined the effects of low concentrations of a surfactant, sodium lauryl sulphate, on the motion of dichloroethane drops descending through water. At very low surfaetant concentrations (10^{-5} gm/liter or less) there was no observable effect. As the concentration was increased, a marked decrease in terminal velocity was observed for drops of equivalent diameter between 2 and 6 mm and this was usually accompanied by earlier boundary layer separation and irregular drop

FIG. 7.5   Terminal velocity of carbon tetrachloride drops falling through water, measured by:

oscillations. At relatively high surfactant concentrations (10^{-2} gm/liter or greater) the systems were said to be "grossly contaminated." The drop terminal velocities again became independent of surfactant concentration while the interface remained rigid, and oscillations became more regular.

Very few workers have succeeded in eliminating all surface-active contaminants from their systems. Moreover, the type and concentration of contaminants present have seldom been characterized. Based on the available evidence, one may draw the following conclusions.

(i) Surfactants tend to damp out internal motion by rendering the interface rigid as discussed in Chapter 3. The influence of surfactants is most significant for low values of κ, since at large κ the viscous resistance of the internal fluid limits internal motion even for pure systems.

(ii) Surfactants have the greatest influence on terminal velocity near the point of transition from rectilinear to oscillating motion. This is presumably because internal circulation can drastically alter the wake structure of a fluid particle (see below) leading to delayed boundary layer separation, smaller wakes, and delayed vortex shedding.

(iii) Surfactants play a particularly important role in high σ systems (e.g., air/water) since surface tension reductions are largest for these systems (see Chapter 3).

(iv) Most of the experimental results in the literature are for "grossly contaminated" bubbles and drops. Since it is so difficult to eliminate surface-active contaminants in systems of practical importance, this is not a serious limitation.

3. Correlation for Contaminated Drops and Bubbles

There is a substantial body of data in the literature on the terminal velocities of bubbles and drops. In view of the influence of system purity discussed above, a separation of this data has been made. Cases where there is evidence that considerable care was taken to eliminate surfactants and where a sharp peak in the U_T vs. d_e curve at low M and κ is apparent (as for the pure systems in Figs. 7.3 and 7.5) are discussed in Section 4.

Grace et al. (G12) applied three types of correlation to a large body of experimental data: the form proposed by Klee and Treybal (K3); that proposed by Hu and Kintner (H12) and its extension by Johnson and Braida (J2); and a wave analogy suggested for bubbles by Mendelson (M7) and extended to drops by Marrucci et al. (M5). The second of these forms gave smaller residuals, especially as M is increased. Even so, it was necessary to eliminate high M systems from the resulting correlation. Cases where wall effects were too significant were also eliminated from the data treated. The criteria which the data had to meet were then Eqs. (9-33) or (9-34) and

$$M < 10^{-3}, \qquad Eo < 40, \qquad Re > 0.1. \qquad (7\text{-}4)$$

The indices in the original Johnson and Braida correlation and the point of intersection between the two linear regions were adjusted to improve the agreement with all the data meeting the above criteria. The resulting correlation (G12) is:

$$J = 0.94 H^{0.757} \qquad (2 < H \le 59.3) \tag{7-5}$$

and

$$J = 3.42 H^{0.441} \qquad (H > 59.3), \tag{7-6}$$

where

$$H = \tfrac{4}{3} Eo\, M^{-0.149} (\mu/\mu_w)^{-0.14}, \tag{7-7}$$

$$J = Re\, M^{0.149} + 0.857, \tag{7-8}$$

and μ_w is the viscosity of water in Braida's experiments, which may be taken as 0.0009 kg/ms (0.9 cp).

A plot of every fourth data point and the lines given by Eqs. (7-5) and (7-6) appears in Fig. 7.6. The gradient discontinuity corresponds approximately to the transition between nonoscillating and oscillating bubbles and drops. In the above correlation, the terminal velocity appears only in the dimensionless group J, and may be expressed explicitly as:

$$U_T = \frac{\mu}{\rho d_e} M^{-0.149} (J - 0.857). \tag{7-9}$$

The r.m.s. deviation between measured and predicted terminal velocities is about 15% for the 774 points with $H \le 59.3$ and 11% for the 709 points with $H > 59.3$. This correlation is recommended for calculations of bubble and drop terminal velocities when the criteria outlined above are satisfied and where some surface-active contamination is inevitable. The predictions from this correlation for carbon tetrachloride drops in water are shown on Fig. 7.5.

Many other correlations for calculating the terminal velocity of bubbles and drops are available [e.g. (H12, J2, K3, T1, V1, W2)]. None covers such a broad range of data as Eqs. (7-5) and (7-6). Moreover, a number of the earlier correlations require that values be read from graphs or that iterative procedures be used to determine U_T.

4. Correlation for Pure Systems

In view of the limited data available for pure systems, Grace et al. (G12) modified the correlation given in the previous section rather than proposing an entirely different correlation. A correction of somewhat similar form to that suggested in Chapter 3 for low Re is employed; i.e.,

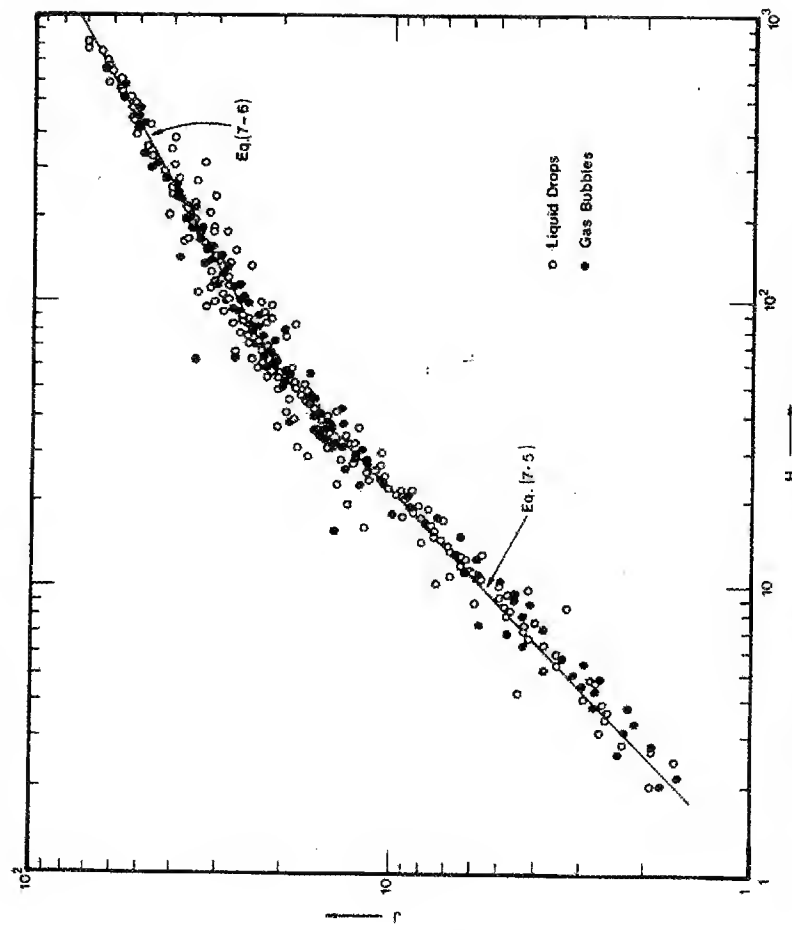$$(U_T)_{pure} = U_T[1 + \Gamma/(1 + \kappa)]. \tag{7-10}$$

FIG. 7.6 Data (showing one point in four) used to obtain general correlation for terminal velocity of drops and bubbles in contaminated liquids, compared with Eqs. (7-5) and (7-6) (B11, B17, D2, E3, E4, G9, G10, G14, H1, H12, J4, K2, K3, K5, L3, L11, P3, T1, W3, Y4).

where Γ is to be obtained experimentally and U_T is predicted using Eqs. (7-5) to (7-9). Since the continuous fluid was water for all the pure systems for which data are available, μ and M cover very restricted ranges. Experimental values of Γ are plotted in Fig. 7.7 as a function of $Eo(1 + 0.15\kappa)/(1 + \kappa)$, where the function of κ was chosen to reduce the spread in the resulting points.

Careful purification of a system has little effect for small and large drops and bubbles. Hence Γ reaches a maximum for a particular value of the abscissa. An envelope has been drawn to provide an estimate of the maximum increase in terminal velocity for bubbles and drops in pure systems over that for contaminated systems. This envelope, together with Eq. (7-10) and the correlation of the previous section, have been used to obtain the upper curve in Fig. 7.5 for carbon tetrachloride drops in water. The curve gives a good representation of the higher velocities observed for carefully purified systems.
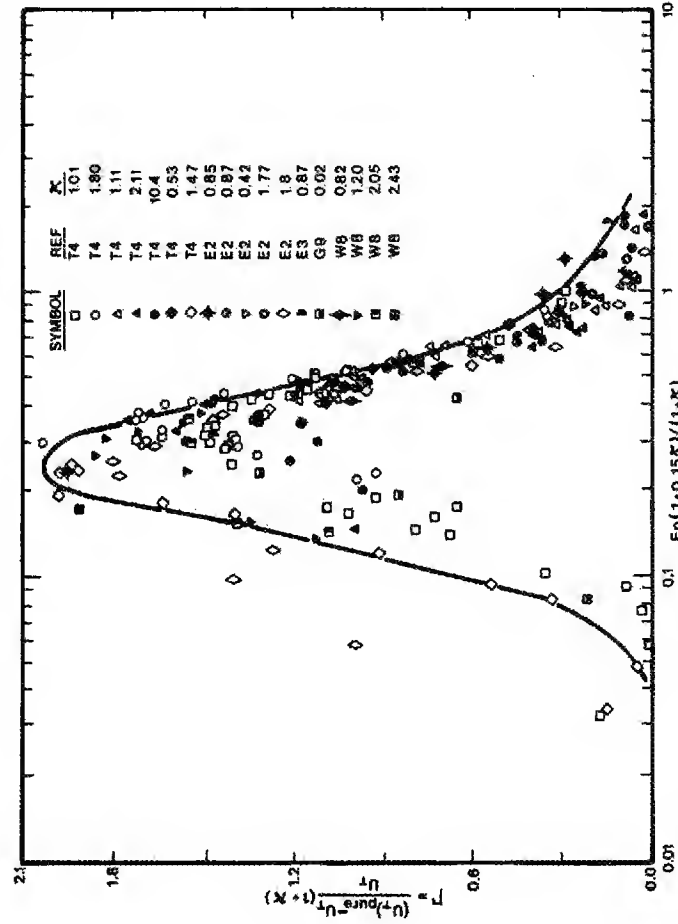
drops, data of Finlay (F1) and Van der Leeden et al. (V2) can be correlated with the best data for water drops in air (B4, G13) by the equations

$$Re = 1.62 \, Eo^{0.755} M^{-0.25} \qquad (0.5 \leq Eo \leq 1.84). \qquad (7\text{-}11)$$

$$Re = 1.83 \, Eo^{0.555} M^{-0.25} \qquad (1.84 \leq Eo \leq 5.0). \qquad (7\text{-}12)$$

$$Re = 2.0 \, Eo^{0.5} M^{-0.25} \qquad (Eo \geq 5.0). \qquad (7\text{-}13)$$

Equation (7-13) predicts that the terminal velocity approaches an upper limit,

$$U_T = 2.0(\Delta\rho \, g\sigma/\rho^2)^{1.4}, \qquad (7\text{-}14)$$

independent of the drop size and the viscosity of the gas.

An alternative correlation given by Garner and Lihou (G5) based on data for different liquids in air may be written:

$$Re = 0.776 \, Eo^{0.66} M^{-0.28} \qquad (Eo \leq 164M^{1.6}), \qquad (7\text{-}15)$$

$$Re = 1.37 \, Eo^{0.55} M^{-0.26} \qquad (Eo > 164M^{1.6}), \qquad (7\text{-}16)$$

This form of correlation was used by Beard (B3) to suggest a correlation for water drops in air under different atmospheric conditions. It should be used with caution for gases with properties widely different from air under atmospheric conditions, but the range of liquid properties covered is broad.

It is an open question whether small quantities of surfactants, too small to influence the gross properties, affect the terminal velocity of liquid drops in air. This appears unlikely in view of the large values of κ, but Buzzard and Nedderman (B18) have claimed such an influence. Acceleration may have contributed to this observation. Quantities of surfactant large enough to lower σ appreciably can lead to significantly increased deformation and hence to an increase in drag and a reduction in terminal velocity (R6).

D. SHAPES OF ELLIPSOIDAL FLUID PARTICLES

1. Theory

General criteria for determining the shape regimes of bubbles and drops are presented in Chapter 2, where it is noted that the boundaries between the different regions are not sharp and that the term "ellipsoidal" covers a variety of shapes, many of which are far from true ellipsoids. Many bubbles and drops in this regime undergo marked shape oscillations, considered in Section F. Where oscillations do occur, we consider a shape averaged over a small number of cycles.

As noted in Chapters 2 and 3, deformation of fluid particles is due to inertia effects. For low Re and small deformations, Taylor and Acrivos (T3) used a matched asymptotic expansion to obtain, to terms of order We^2/Re,

$$\frac{r(\theta)}{a_0} = 1 - \lambda \, We \, P_2(\cos\theta) - \frac{3\lambda(11\kappa + 10)}{70(1 + \kappa)}\frac{We^2}{Re}P_3(\cos\theta). \qquad (7\text{-}17)$$

FIG. 7.7 Correction factor, Γ, relating terminal velocity in pure systems to value in corresponding contaminated systems (E2, E3, G9, T4).

SYMBOL	REF	κ
□	T4	1.01
○	T4	1.80
△	T4	1.11
●	T4	2.11
◆	T4	1.04
◇	T4	0.53
◣	T4	1.47
◢	E2	0.85
▷	E2	0.87
◯	E2	0.42
◻	E2	1.77
◥	E2	1.8
◤	E3	0.87
◆	G9	0.02
■	W8	0.82
◈	W8	1.20
□	W8	2.05
■	W8	2.43

y-axis: $\Gamma = \dfrac{(U_{T,\text{pure}} - U_T)}{U_T}(1 + \kappa)$

x-axis: $Eo(1 - 0.15\kappa)/(1+\kappa)$

The envelope in Fig. 7.5 is for the maximum increase in terminal velocity obtainable by eliminating surface-active contaminants. For systems of intermediate purity, Γ may be assigned a value between zero and that given by the envelope. Since the envelope has been derived solely from experiments for aqueous systems, it should be used with caution for nonaqueous systems.

C. TERMINAL VELOCITIES OF LIQUID DROPS IN AIR

As indicated in Chapter 2, liquid drops falling through gases have such extreme values of γ and κ that they must be treated separately from bubbles and drops in liquids. Few systems have been investigated aside from water drops in air, discussed above, and what data are available for other systems (F1, G5, L5, V2) show wide scatter. Rarely have gases other than air been used, and some data for these cases [e.g. (L5, N2)] cannot be interpreted easily because of evaporation and combustion effects. Results for drops in air at other than room temperature (S8) differ so radically from results of other workers that they cannot be used with confidence.

For Eo ≤ 0.15, drops are closely spherical and terminal velocities may be calculated using correlations given in Chapter 5 for rigid spheres. For larger

where

$$\lambda = \frac{1}{3!2(1+\kappa)^3}\left\{(3 + 10.3\kappa + 11.4\kappa^2 + 4.05\kappa^3) - \frac{(1+\kappa)(\tfrac{2}{\kappa} - 1)}{3}\right\}. \quad (7\text{-}18)$$

P_2 and P_3 are the second- and third-order Legendre polynomials. For small We, the deformed bubble or drop is predicted to be exactly spheroidal. In principle, the spheroid may be either prolate or oblate, but for cases of physical significance oblate shapes are predicted. If $Re_p \gg 1$, droplet shapes are predicted to differ only slightly from the case where both Re and Re_p are small (P1). Brignell (B14) extended the series expansion to terms of order We Re^2. Since deformation at low Re is only observable for high M systems, this approach is of little practical value.

At larger Re and for more marked deformation, theoretical approaches have had limited success. There have been no numerical solutions to the full Navier–Stokes equation for steady flow problems in which the shape, as well as the flow, has been an unknown. Savic (S3) suggested a procedure whereby the shape of a drop is determined by a balance of normal stresses at the interface. This approach has been extended by Pruppacher and Pitter (P6) for water drops falling through air and by Wairegi (W1) for drops and bubbles in liquids. The drop or bubble adopts a shape where surface tension pressure increments, hydrostatic pressures, and hydrodynamic pressures are in balance at every point. Thus

$$\Delta\rho\, g y + \sigma[(1/R_1) + (1/R_2) - (2/R_0)] + p_{HD} - (p_{HD})_p = 0. \quad (7\text{-}19)$$

where y is measured vertically upwards from the lowest point, 0, of the drop: R_1 and R_2 are the principal radii of curvature at a general point on the surface ($R_1 = R_2 = R_0$ at 0); and p_{HD} and $(p_{HD})_p$ are the pressures due to the external and internal fluid motions, respectively, less the stagnation pressures. It is usual practice to assume that $(p_{HD})_p \ll p_{HD}$, although this has been criticized by Foote (F2). With this assumption, drop shapes can be determined if the distribution of p_{HD} is known. Savic assumed that the pressure distribution was the same as that about a rigid sphere at the same value of Re; Pruppacher and Pitter used the same approach, with more recent and reliable pressure data. Deformations were assumed small and the shape represented by a cosine series (P6, S3) or by Legendre polynomials (W1). The general procedure is the reverse of that employed by McDonald (M6) to calculate surface dynamic pressure distributions from observed drop shapes. The predictions become less realistic with increasing particle size and deformation because of increasing error in the assumed pressure distribution.

A reasonable approximation to the observed profile of many drops and bubbles is a combination of two half oblate spheroids with a common major axis and different minor axes (B8, F1). This observation has been used (W1) to propose a model from which bubble and drop shapes can be estimated at

high Re. The pressure distribution over the front surface is assumed to be the potential flow pressure distribution over a complete spheroid of the same eccentricity, while the dynamic pressure over the rear is assumed uniform so that the rear deforms like a sessile drop or bubble of the same size in the same system.† The theory correctly predicts that drops in air deform most at the front, while some systems (e.g., bubbles in water) begin by flattening more at the front, then deforming more at the rear with increasing d_e.

2. Experimental Results for Bubbles and Drops in Liquids

It is possible to prepare a generalized plot of mean aspect ratio $\bar{E}$, where $\bar{E} = $ maximum vertical dimension/maximum horizontal dimension. In the literature, both We and Eo are commonly used as independent variables for correlating shape parameters for fluid particles. The Eotvos number gives a better overall representation (G12). As in Section B, it is necessary to separate data for liquid drops falling through air (see Section 4) and for very pure systems (see Section 3). The generalized graphical correlation for bubbles and drops in contaminated liquid media is given in Fig. 7.8. Wall effects have been eliminated using the same criteria as for terminal velocities, i.e., Eqs. (9-33) and (9-34).
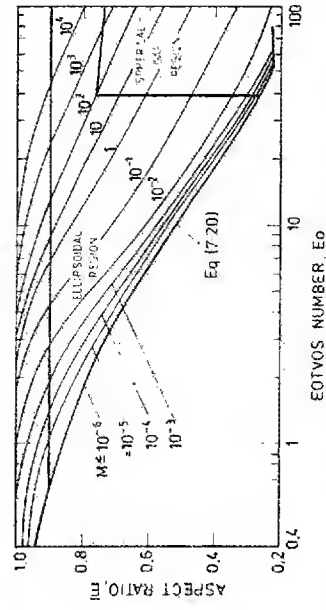

FIG. 7.8   Correlation for mean aspect ratio E of drops and bubbles in contaminated systems (B10, H7, K2, K3, K4, T6, W1, W6, Y4).

From Fig. 7.8 it is clear that deformation depends not only on Eo but also on M, higher M giving rise to less deformation at the same Eo. For low M, it is reasonable to correlate the data by a single line:

$$\bar{E} = 1/(1 + 0.163\,Eo^{0.757}) \quad (Eo < 40, M \le 10^{-6}). \quad (7\text{-}20)$$

given by Wellek et al. (W6). For higher M, Fig. 7.8 can be used to estimate the height-to-width ratio of bubbles and drops in liquids. An alternative correlation

† Previous workers have also made use of potential flow pressure distributions about spheroids, but no allowance was made for lack of fore-and-aft symmetry, while the constant pressure condition was satisfied only near the front stagnation point (S1) or at the equator and poles (H6, M11).

obtained by Tadaki and Maeda (T1) for air bubbles with $M < 10^{-3}$ expresses $d_e/2a = E^{1/3}$ (where $2a$ is the maximum horizontal dimension) as a function of a dimensionless group $Ta = Re\, M^{0.23}$. Vakrushev and Efremov (V1) extended this approach to give:
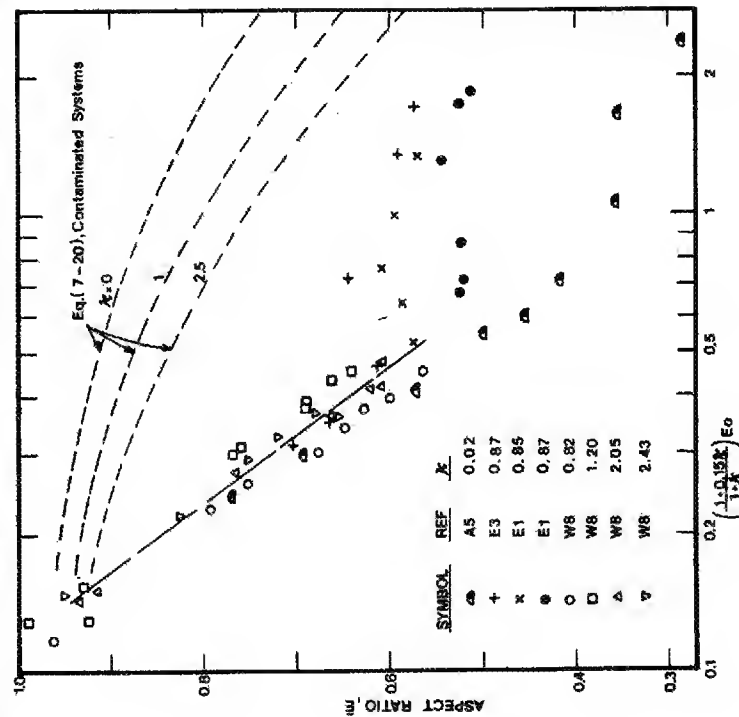
$$\bar{E} = 1 \qquad (Ta \leq 1), \tag{7-21}$$

$$\bar{E} = [0.81 + 0.206\tanh\{2(0.8 - \log_{10} Ta)\}]^3, \quad (1 \leq Ta \leq 39.8), \tag{7-22}$$

$$\bar{E} = 0.24 \qquad (Ta \geq 39.8) \tag{7-23}$$

Equation (7-23) implies a spherical-cap shape with an included angle of about 50° (see Chapter 8).

3. Experimental Results for Pure Systems

Drops and bubbles in highly purified systems are significantly more deformed than corresponding fluid particles in contaminated systems. Increased flattening of fluid particles in pure systems results from increased inertia forces related to the increased terminal velocities discussed above. Some experimental results for drops and bubbles in water (low M systems) are shown in Fig. 7.9. The

SYMBOL	REF	κ
⬭	A5	0.02
+	E3	0.87
×	E1	0.85
●	E1	0.87
○	W8	0.82
□	W8	1.20
△	W8	2.05
▽	W8	2.43

ASPECT RATIO, E

$0.2\left(\frac{1+0.15\kappa}{1+\kappa}\right)Eo$

Eq.(7-20), Contaminated Systems

aspect ratios lie significantly below the predictions of Eq. (7-20). The abscissa used in Fig. 7.7 brings the data together for $[Eo(1 + 0.15\kappa)(1 + \kappa)] < 0.5$, but there is considerable scatter beyond this point. Once again the greatest effect of system purity is in the ellipsoidal regime, small bubbles and drops being spherical ($E = 1$) and large ones approaching $E = 0.24$ no matter how pure the system. In addition, system purity has the greatest effect at low κ.

4. Experimental Results for Drops in Air

The shapes of liquid drops falling through air can be conveniently represented by two oblate semispheroids with a common semimajor axis a and minor semiaxes b_1 and b_2 (B8, F1). Several workers have reported measurements of the aspect ratio, $(b_1 + b_2)/2a$, and these are shown as a function of Eo in Fig. 7.10. The data can be represented by the relationships

$$\frac{b_1 + b_2}{2a} \approx 1.0 \qquad (Eo \leq 0.4), \tag{7-24}$$

$$\frac{b_1 + b_2}{2a} = \frac{1.0}{1.0 + 0.18(Eo - 0.4)^{0.8}} \qquad (0.4 < Eo < 8). \tag{7-25}$$

The shape factor, $b_1/(b_1 + b_2)$, is also plotted in Fig. 7.10 based on data given by Finlay (F1). The relationships

$$\frac{b_1}{b_1 + b_2} = 0.5 \qquad (Eo \leq 0.5), \tag{7-26}$$

$$\frac{b_1}{b_1 + b_2} = \frac{0.5}{1.0 + 0.12(Eo - 0.5)^{0.8}} \qquad (0.5 < Eo < 8) \tag{7-27}$$

give an adequate fit to the data. Equations (7-25) and (7-27) are plotted in Fig. 7.10.

A good approximation to the shape of deformed drops in air may therefore be obtained from knowledge of the system properties and drop size. The ratios $(b_1 + b_2)/2a$ and $b_1/(b_1 + b_2)$ are calculated from Eo using Eqs. (7-25) and (7-27). From geometric considerations

$$d_e/a = 2\left[\frac{b_1 + b_2}{2a}\right]^{1/3}, \tag{7-28}$$

so that the semiminor axes can then be calculated. The surface area may be estimated by again assuming that the drop is composed of two half spheroids, i.e.,

$$A = 2\pi a^2 + \frac{\pi}{2}\left\{\frac{b_1^2}{e_1}\ln\left(\frac{1+e_1}{1-e_1}\right) + \frac{b_2^2}{e_2}\ln\left(\frac{1+e_2}{1-e_2}\right)\right\}. \tag{7-29}$$

where $e_1 = (1 - b_1^2/a^2)^{1/2}$ and $e_2 = (1 - b_2^2/a^2)^{1/2}$ are the eccentricities of the
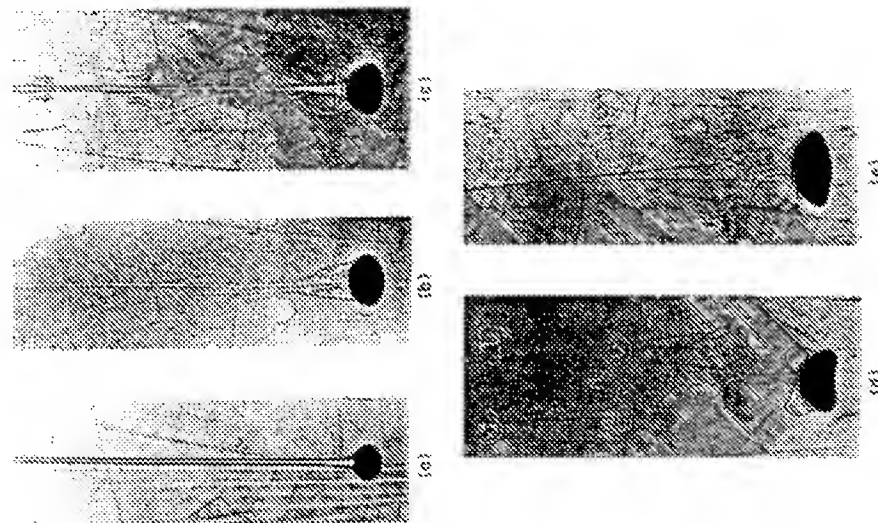
7. Ellipsoidal Fluid Particles

FIG. 7.11 Wake configurations for drops in water (right, purified system), reproduced from Winnikow and Chao (W8) with permission. (a) nonoscillating nitrobenzene drop, $d_e = 0.380$ cm, Re = 515; steady thread-like laminar wake; (b) nonoscillating m-nitrotoluene drop, $d_e = 0.366$ cm, Re = 688; steady thread accompanied by attached toroidal vortex wake; (c) oscillating nitrobenzene drop, $d_e = 0.380$ cm, Re = 656; central thread plus asymmetric outer vortex sheet rolled inward to give inverted bottle shape of wake; (d) oscillating nitrobenzene drop, $d_e = 0.434$ cm, Re = 772, vortex sheet in c has broken down to form vortex rings; (e) oscillating nitrobenzene drop, $d_e = 0.400$ cm, Re = 804, vortex rings in d now shed asymmetrically and the drop exhibits a rocking motion.

therefore occurs at a Reynolds number of about 200 [G8, H6, S9], while for pure systems at relatively low κ, the onset of oscillations is delayed [H6, W8, but seldom beyond Re = 1000. In viscous liquids where Re never reaches 200 over the range of practical interest (see Fig. 2.5), no oscillations occur [K4, T2]. While a critical Weber number has often been suggested for the onset of oscillations in pure, low κ systems, no agreement has been reached on what the

critical value should be [E2, H6, W8], and the value of Re and purity of the system appear to be better indicators of the likelihood of secondary motion. While wake shedding appears to provide the excitation for shape oscillations, the frequency of the two phenomena may differ. For example, Winnikow and Chao (W8) measured oscillation frequencies between about 63 and 80, of wake shedding frequencies for nitrobenzene drops in water, while Edge et al. (E1) found the two frequencies to be identical. To obtain a simple physical understanding of shape oscillations, consider forced vibration of a single-degree-of-freedom damped system [see, e.g., Anderson (A2)]. Suppose that the wake shedding provides a harmonic excitation of frequency f_{SV}, while the natural frequency of the drop is given (1.11) by

$$f_N = \sqrt{\frac{48\sigma}{\pi^3 d_e^3 (3\rho_p + 3\rho)}} \qquad (7.30)$$

If we define

$$\bar{f} = (f_N + f_{SV})/2 \qquad (7.31)$$

and

$$\Delta f = (f_N - f_{SV})/2 \qquad (7.32)$$

and if $\Delta f \ll \bar{f}$, then the motion is approximately

$$E - E_* \propto \frac{\bar{f}}{\Delta f} \sin(2\pi \Delta f t)\cos(2\pi \bar{f} t) \qquad (7.33)$$

As illustrated in Fig. 7.12, the drop then oscillates at frequency $\bar{f}$ with the amplitude modulated at frequency Δf.
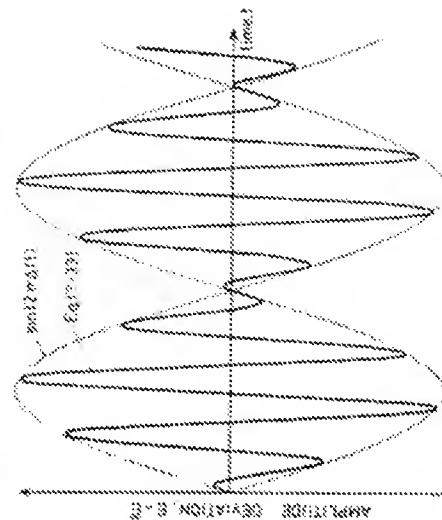

FIG. 7.12 Simple model to show nature of shape oscillations for bubbles and drops in free motion.

$C_D(Re)$ curves for drops and bubbles (B11, E1, E2, T4). The influence of oscillations on heat and mass transfer is discussed in Section III.

G.   INTERNAL CIRCULATION

Surface-active contaminants play an important role in damping out internal circulation in deformed bubbles and drops, as in spherical fluid particles (see Chapters 3 and 5). No systematic visualization of internal motion in ellipsoidal bubbles and drops has been reported. However, there are indications that deformations tend to decrease internal circulation velocities significantly (M12), while shape oscillations tend to disrupt the internal circulation pattern of droplets and promote rapid mixing (R3). No secondary vortex of opposite sense to the prime internal vortex has been observed, even when the external boundary layer was found to separate (S11). "

H.   THEORETICAL SOLUTIONS FOR DEFORMED BUBBLES AND DROPS

Attempts to obtain theoretical solutions for deformed bubbles and drops are limited, while no numerical solutions have been reported. A simplifying assumption adopted is that the bubble or drop is perfectly spheroidal. Saffman (S1) considered flow at the front of a spheroidal bubble in spiral or zig-zag motion. Results are in fair agreement with experiment. Harper (H4) tabulated energy dissipation values for potential flow past a true spheroid. Moore (M11) applied a boundary layer approach to a spheroidal bubble analogous to that for spherical bubbles described in Chapter 5. The interface is again assumed to be completely free of contaminants. The drag is given by

$$C_D = \frac{48}{Re} f_1(E) \left[1 + \frac{f_2(E)}{Re^{1/2}} \right],$$ (7-34)

where the first term results from the viscous energy dissipation for irrotational flow past an oblate spheroid, and the second arises from dissipation in the boundary layer and wake. Harper (H5) tabulated values of $f_1(E)$ and $f_2(E)$ and plotted drag curves for four values of M. The curves show minima and are in qualitative agreement with observed $C_D(Re)$ curves for bubbles. No attempt has been reported to extend this treatment to deformed drops of low κ.

III.   HEAT AND MASS TRANSFER

A.   REGIMES OF MOTION AND TRANSFER

The flow and shape transitions for small and intermediate size bubbles and drops are summarized in Fig. 7.13. In pure systems, bubbles and drops circulate freely, with internal velocity decreasing with increasing κ. With increasing size they deform to ellipsoids, finally oscillating in shape when Re exceeds a value of order 10^3. In contaminated systems spherical and nonoscillating ellipsoidal

In practice, this model is oversimplified since the exciting wake shedding is by no means harmonic and is itself coupled with the shape oscillations and since Eq. (7-30) is strictly valid only for small oscillations and stationary fluid particles. However, this simple model provides a conceptual basis to explain certain features of the oscillatory motion. For example, the period of oscillation, after an initial transient (E1), becomes quite regular while the amplitude is highly irregular (E3, S4, S5). "Beats" have also been observed in drop oscillations (D4). If f_W and f_N are of equal magnitude, one would expect resonance to occur, and this is one proposed mechanism for breakage of drops and bubbles (Chapter 12).

Equation (7-30) gives the natural frequency of the fundamental mode for stationary fluid particles undergoing small oscillations with viscous forces neglected. It has been modified to account for viscous effects (L4, M10, S10). Observed oscillation frequencies are generally less than those given by Eq. (7-30), typically by 10-20% for drops in free motion in impure systems (S4) and by 20-40% for pure systems (E3) and this explains the reduction in frequency.

In general, oscillations may be oblate-prolate (H8, S5), oblate-spherical, or oblate-less oblate (E2, F1, H8, R3, R4, S5). Correlations of the amplitude of fluctuation have been given (R3, S5), but these are at best approximate since the amplitude varies erratically as noted above. For low M systems, secondary motion may become marked, leading to what has been described as "random wobbling" (E2, S4, W1). There appears to have been little systematic work on oscillations of liquid drops in gases. Such oscillations have been observed (F1, M4) and undoubtedly influence drag as noted earlier in this chapter. Measurements (Y3) for 3-6 mm water drops in air show that the amplitude of oscillation increases with d_e, while the frequency is initially close to the Lamb value (Eq. 7-30) but decays with distance of fall.

Oscillating bubbles and drops may travel along zig-zag or spiral (helical) paths. Some authors have observed only one of these modes while others have observed both. There is some evidence that the type of secondary motion is affected by the mode of release (M8). Saffman (S1) performed a careful series of experiments on air bubbles in water. Rectilinear motion was found to become unstable, and gave rise to zig-zag motion which in turn gave way to spiral motion for larger bubbles.' The paths followed by fluid particles undergoing secondary motion are no doubt associated with the type of wake. Details of the paths, orientation, and periods of spiralling and zig-zagging drops and bubbles are presented by Mercier and Rocha (M9) and Tsuge and Hibino (T6).

Secondary motion plays an important role in increasing drag (L7) and in promoting heat and mass transfer from bubbles or drops. The onset of oscillations corresponds approximately to the maximum in $U_T(d_e)$ and minimum in

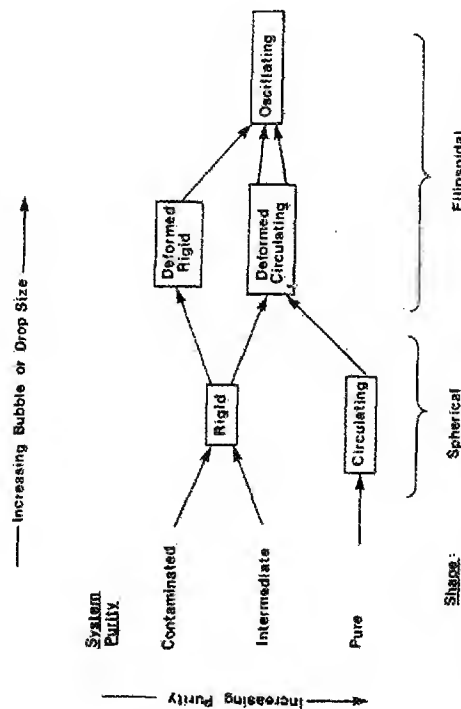' See also Table 7.1.

7. Ellipsoidal Fluid Particles

FIG. 7.13 Flow transitions for bubbles and drops in liquids (schematic).

bubbles and drops are effectively rigid but, for $Re \gtrsim 200$, wake shedding and shape oscillations occur with associated motion of the internal fluid. In systems of intermediate purity, small bubbles and drops are rigid but, with increasing size, they become deformed and partially circulating. Circulation increases with increasing size, and shape oscillations occur at $Re \gtrsim 200$. The Reynolds number marking the transition from rigid to circulating behavior depends on system purity.

These flow transitions lead to a complex dependence of transfer rate on Re and system purity. Deliberate addition of surface-active material to a system with low to moderate κ causes several different transitions. If $Re \lesssim 200$, addition of surfactant slows internal circulation and reduces transfer rates to those for rigid particles, generally a reduction by a factor of 2–4 (S6). If $Re \gtrsim 200$ and the drop is not oscillating, addition of surfactant to a pure system decreases internal circulation and reduces transfer rates. Further additions reduce circulation to such an extent that shape oscillations occur and transfer rates are increased. Addition of yet more surfactant may reduce the amplitude of the oscillation and reduce the transfer rates again. Although these transitions have been observed (G7, S6, T5), additional data on the effect of surface active materials are needed.

The internal resistance is always decreased substantially when a bubble or drop oscillates, but the external resistance may be unaffected if the Reynolds number is high enough. A rough criterion can be obtained from Eq. (11-63) for vibration of a particle in an axial stream. Oscillation has negligible effect on the external resistance if

$$\frac{Re_v}{Re}\left(\frac{2a'}{d}\right)^{-0.45} < 0.2, \quad (7\text{-}35)$$

III. Heat and Mass Transfer

where a' is the amplitude of the oscillation, $Re_v = 4a'fd/v$ is the vibration Reynolds number, and f is the frequency. Rearranging Eq. (7-35) yields:

$$\frac{a'f}{U_T} < 0.05\left(\frac{2a'}{d}\right)^{0.45}. \quad (7\text{-}36)$$

Assuming spherical-oblate oscillations with amplitude $2a' = (1 - E)d_e$, taking $E = 0.5$ as a rough approximation and replacing d by d_e and f by f_N from Eq. (7-30), we find no effect of oscillation on the external resistance if

$$d_e f_N/U_T < 0.15. \quad (7\text{-}37)$$

For liquid drops in gases the terminal velocity is so large that the inequality is obeyed and oscillation has essentially no effect on transfer. For drops and bubbles in liquids, the effect of oscillation on transfer is significant.

B. DEFINITIONS

Mass transfer rates from drops are obtained by measuring the concentration change in either or both of the phases after passage of one or more drops through a reservoir of the continuous phase. This method yields the average transfer rate over the time of drop rise or fall, but not instantaneous values. For measurements of the resistance external to the drop this is no drawback, because this resistance is nearly constant, but the resistance within the drop frequently varies with time. The fractional approach to equilibrium, F, is calculated from the compositions and is then related to the product of the overall mass transfer coefficient and the surface area:

$$(\overline{KA})_p = -(\pi d_e^3/6t)\ln(1 - F), \quad (7\text{-}38)$$

where t is the time of free rise or fall and $(\overline{KA})_p$ is the time-average coefficient-area product based on dispersed phase concentrations. If the resistance in each phase may be added,

$$\frac{1}{(\overline{KA})_p} = \frac{H}{\overline{kA}} + \frac{1}{(\overline{kA})_p}, \quad (7\text{-}39)$$

If the resistance external to the drop is negligible,

$$(\overline{kA})_p = -(\pi d_e^3/6t)\ln(1 - F). \quad (7\text{-}40)$$

Many investigators base mass transfer coefficients upon the area of the volume-equivalent sphere, especially for oscillating drops:

$$(\overline{kA})_p/A_e = -(d_e/6t)\ln(1 - F). \quad (7\text{-}41)$$

The Sherwood number based on this coefficient is

$$Sh_{pe} = [(\overline{kA})_p/A_e]d_e/\mathscr{D}_p. \quad (7\text{-}42)$$

A similar definition is frequently used for the continuous phase Sherwood number

$$Sh_e = [\bar{K}_1/A_s]d_e/\mathscr{D} \qquad (7\text{-}43)$$

In some studies the surface area of the particle is measured and area-free Sherwood numbers are reported

$$Sh_p = K_p d_e/\mathscr{D}_p, \qquad (7\text{-}44)$$

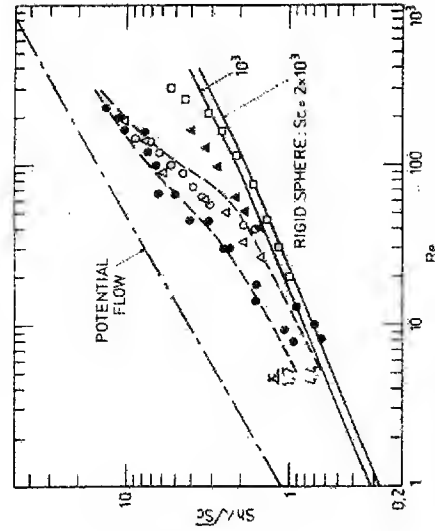$$Sh = Kd_e/\mathscr{D}. \qquad (7\text{-}45)$$

Careful reading of papers is required to determine which definition has been used. Measurements of the continuous phase resistance around bubbles frequently use photographic, volumetric, or pressure change techniques to yield instantaneous rates of mass transfer, and thus kA. Here too, both definitions of the Sherwood number, Eqs. (7-43) and (7-45), have been used.

C. EXTERNAL RESISTANCE

Figure 7.14 gives area-free Sherwood numbers for organic drops in water. In the furfural–water system ($\kappa = 1.7$), the transition from circulation at low Re to circulation at high Re agrees well with the treatment of Chapter 5, i.e., deformation has little effect on the area-free Sherwood number. For this value of κ, however, it is not clear whether the drops were circulating for Re < 10. For the diol–water system ($\kappa = 80$), circulation is so slow that Sh agrees with the result for rigid spheres up to Re $\doteq 200$ where oscillation begins. At this Reynolds number, $d_e f_N/U_T \doteq 0.6$ and oscillations are expected to affect the Sherwood number; see Eq. (7-37). The chlorobenzene/benzene drop system ($\kappa \doteq 0.7$) shows the effect of addition of surfactant. Without surfactant, Sh departs from the line for solids at Re $\doteq 20$ and deviation increases with Re as circulation becomes stronger. The data with added surfactant follow the line for solids up to Re $\doteq 50$ and remain below the pure system values at higher Re. Even the system without surfactant was contaminated, since the data should lie above those for $\kappa \doteq 1.7$. The presence of surface-active materials acts in the same way as an increase in the drop viscosity with respect to terminal velocity. Transition from a stagnant drop to a drop with circulation may occur at any Re below 200. The data for aniline drops ($\kappa = 4.4$) lie between the systems with $\kappa = 1.7$ and 80, and show reasonable agreement with Eq. (5-39). Oscillation in contaminated systems and circulation in less contaminated systems both cause Sh to rise more rapidly than $Re^{1/2}$.

1. Particles without Shape Oscillations

For nonspherical particles the only theoretical treatment available is for potential flow around a spheroid (L10). For an oblate spheroid the area-free

Symbol	κ	$\bar{\gamma}$	Sc	Ref.
□	80	0.95	1660	(G8)
○	4.4	1.02	1100	(H11)
●	1.7	1.16	975	(G8, H11)
△	0.7	1.02	1020	(T5)
▲	same as △ but contaminated with 10^{-3} gm liter sodium oleyl-p-anisidine sulfonate Eq. (5-39)			
---	Rigid sphere. Eq. (5-25), Table 5.4E			
- . .	Sphere in potential flow. Eq. (5-35)			

FIG. 7.14 Area-free mass transfer factors. Sh , Sc. for drops.

Sherwood number is

$$Sh = \frac{2}{\sqrt{\pi}}Pe^{1/2}\left[\frac{8e^3 E^{1/3}}{3(\sin^{-1}e - eE)}\right]^{1/2}\bigg/\left[1 + \frac{E^2}{2e}\ln\left(\frac{1+e}{1-e}\right)\right], \qquad (7\text{-}46)$$

where Pe is based on d_e and

$$e = (1 - E^2)^{1/2}. \qquad (7\text{-}47)$$

Since the area ratio is given by

$$\frac{A}{A_e} = \frac{1}{2E^{2/3}}\left[1 + \frac{E^2}{2E}\ln\left(\frac{1+e}{1-e}\right)\right], \qquad (7\text{-}48)$$

then

$$Sh_e = \frac{2}{\sqrt{\pi}}Pe^{1/2}\left[\frac{2e^3}{3E(\sin^{-1}e - eE)}\right]^{1/2}. \qquad (7\text{-}49)$$

Comparison of these equations shows that the area-free Sherwood number is only slightly affected by eccentricity; e.g. $Sh/Pe^{1/2}$ for a spheroid with $E = 0.4$ is only 8.5% larger than that for the equivalent sphere while the area ratio A/A_e is 17% larger. Therefore, we expect little effect of deformation on the area-free Sherwood number for bubbles and drops at high Re. This is borne out by the agreement of the data in Fig. 7.14 with Eq. (5-39), derived for fluid spheres.
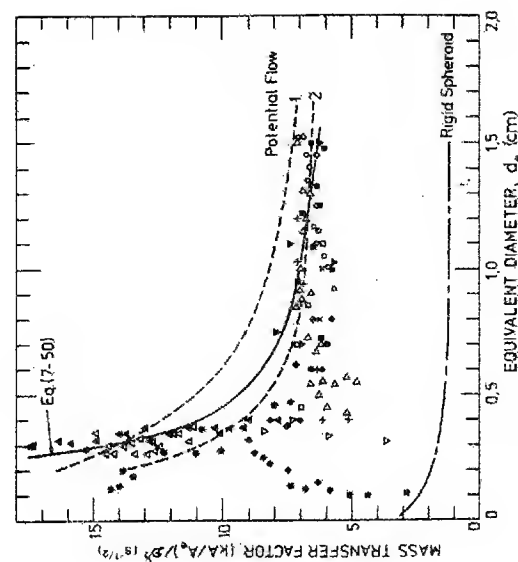
a. *Drops in Gases*   For liquid drops in gases at low pressure the equations for solid particles in Chapter 6 can be used to predict heat and mass transfer rates. Figure 7.10 shows the area ratio α and the ratio L'/d_e as functions of Eo, to facilitate use of Eq. (6-34), while areas may be calculated from Eq. (7-29) or from Eq. (7-48). Surface-active materials should have little effect. For drops in high-pressure gases, oscillations may become important if Re > 200 and the terminal velocity is small enough that $d_e f_N/U_T > 0.1$.

Near the point of drop release, transfer coefficients can be much different from those predicted, due to large amplitude oscillation and internal circulation induced by departure from the nozzle or tip (A1, G4, Y3).

b. *Drops in Liquids*   For drops in pure liquid systems, the area-free Sherwood number may be taken as the larger of the values calculated from the equations for solid spheres in Chapter 5 or Eq. (5-39) for fluid spheres. This provides a transition from the lines for solids in Fig. 7.14 to the potential flow line with increasing Re. For impure systems, surface-active materials may immobilize the drop surface and reduce the coefficients to those for solid particles. The area-free Sherwood number should be equal to or above that for a solid sphere, yet below that for a fluid sphere given by Eq. (5-39). If the system is grossly contaminated, oscillations occur if Re > 200.

c. *Bubbles in Water*   Water is the only continuous fluid for which reliable mass transfer data are available at low M. Figure 7.15 presents the mass transfer factor $(\overline{kA}/A_e)/Q^{1/2}$ for bubbles in water including only data in which wall effects are small $(d_e/D < 0.12)$ and for which the water had been degassed. Dissolved gases can transfer into the bubble and reduce the driving force appreciably (B13, L6, W5). The scatter in the figure is due to different methods of bubble release (Z2), different techniques of measuring the mass transfer rate (G1, W7), and different system purities (R1). Figure 7.15 also shows the mass transfer factor for a rigid spheroid with its aspect ratio given by Eq. (7-20), its velocity by the lower curve in Fig. 7.3, and its Sherwood number calculated from Eqs. (6-16) and (6-17) with Sc = 500. Predictions for potential flow from Eq. (7-46) are also shown, based on the properties of water at 25 C with terminal velocity from the upper curve in Fig. 7.3. Curve 1 corresponds to pure systems. Curve 2 corresponds to the shape in a contaminated system given by Eq. (7-20).

For $d_e > 0.5$ cm, the data agree closely with the potential flow solution with the shape appropriate to a contaminated system. For $d_e < 0.5$ cm, system purity

has a pronounced effect, just as on terminal velocity (see Fig. 7.3). In carefully purified systems [e.g. (Z2)], the mass transfer coefficient increases sharply with decreasing d_e, but contaminated systems do not show such a sharp increase. With 1.2 ppm *n*-nonanol added, the coefficient decreases towards the value for a rigid spheroid. Garner and Hammerton (G3) and Weiner (W4) apparently used systems of intermediate purity. Weiner also found that the mass transfer coefficient and terminal velocity decreased with bubble age due to accumulation of surfactants. The data for pure systems with $d_e < 0.5$ cm are better predicted by the potential flow solution with shape given by Fig. 7.9, but the predicted mass transfer factors increase less rapidly with decreasing bubble size than the data. The failure of the prediction results from zig-zag and helical motion in the range 0.2 cm $< d_e < 0.4$ cm (see Table 7.1).

Figure (plot): axes — MASS TRANSFER FACTOR $(kA_e/A_e)/Q^{1/2}$ $(s^{-1/2})$ versus EQUIVALENT DIAMETER, d_e (cm); curves labelled "Potential Flow", "Eq.(7-50)", "Rigid Spheroid", "1", "2".

FIG. 7.15   Mass transfer factor $(\overline{kA}/A_e)/\overline{Q}$ for gas bubbles in water.

Experimental Data

Symbol	Gas	Ref.	Symbol	Gas	Ref.
+	CO_2	(J1)	△	CO_2	(Z2)
*	CO_2	(W4)	▽	CO_2	(R1)[a]
●	CO_2	(C1)	○	O_2	(V3)
◇	CO_2	(G15)	◆	C_2H_2	(L2)
△	CO_2	(D3)	×	C_2H_4	(J1)
▶	CO_2	(B2)	◆	C_2H_4	(G3)
■	CO_2	(L6)	□	C_4H_8	(J1)

[a] As △, but with 1.2 ppm *n*-nonanol.

A reasonable upper limit on the mass transfer factor from bubbles to well-purified water at room temperature is given by:

$$\frac{\overline{kA}/A_e}{\mathscr{D}^{1/2}} = \frac{0.14}{d_e^3} + \frac{6.94}{d_e^{1/4}}, \tag{7-50}$$

with d_e in cm and the left side in $s^{-1/2}$. For contaminated systems, the data for $d_e > 0.5$ cm are well represented by taking $(\overline{kA}/A_e)/\mathscr{D}^{1/2} = 6.5 \ s^{-1/2}$.

2. Particles with Shape Oscillations

When the shape of a particle oscillates, the surface area changes with time. This situation has been modeled by neglecting the motion adjacent to the surface due to the terminal velocity of the particle, i.e., by considering the particle to be oscillating but stationary, with material transferred by transient molecular diffusion over a time equal to the period of oscillation. For $Sc \gg 1$ the thin concentration boundary layer assumptions are invoked (see Chapter 1).

Two alternative assumptions have been made for the manner in which the area variation occurs. The more realistic postulates that all elements of the surface remain in the surface throughout an oscillation cycle. Increasing surface area stretches the surface (A3, B5) and causes a velocity normal to the surface which increases the diffusion rate. For a surface of area A_0 suddenly exposed at $t = 0$, the mass transfer product averaged over time is given by

$$\frac{\overline{kA}}{A_0} = 2\sqrt{\frac{\mathscr{D}}{\pi t}}\left[\frac{1}{t}\int_0^t \left(\frac{A}{A_0}\right)^2 dt'\right]^{1/2}, \tag{7-51}$$

where the bracketed term represents the effect of the area variation. The value of $\overline{kA}$ is proportional to the r.m.s. interfacial area, so that the transfer rate is larger when the area oscillates.

The alternate assumption is that new elements are brought to the surface as the area increases, and the oldest elements are removed from the surface when the area decreases (B16). For a surface of area A_0 exposed at $t = 0$, the time-averaged mass transfer product is then

$$\frac{\overline{kA}}{A_0} = 2\sqrt{\frac{\mathscr{D}}{\pi t}} + \sqrt{\frac{\mathscr{D}}{\pi}}\frac{1}{t}\int_0^t\left[\int_0^T \frac{1}{\sqrt{T-t'}}\frac{d(A/A_0)}{dt'}dt'\right]dT. \tag{7-52}$$

The first term on the right-hand side represents transfer to the elements of surface present over the entire time period t, while the second represents transfer to appearing or disappearing elements. The fresh surface model, Eq. (7-52), predicts larger coefficients than the surface stretch model, Eq. (7-51).

Given the time variation of the area of a fluid particle, the $\overline{kA}$ product is easily calculated. For oscillating droplets, Angelo et al. (A3) showed that the time variation of area is given closely by:

$$A/A_0 = 1 + \varepsilon \sin^2(\pi ft), \tag{7-53}$$

where $1 + \varepsilon$ is the ratio of maximum area to minimum area, A_0. Assuming that the averaging time is the period of oscillation, f^{-1}, and that the oscillation is spherical-oblate, we obtain from Eqs. (7-51) and (7-53) for the surface stretch model:

$$Sh_e = \frac{2}{\sqrt{\pi}}\sqrt{\frac{d_e^2 f}{\mathscr{D}}}\sqrt{1 + \varepsilon + \frac{3\varepsilon^2}{8}}, \tag{7-54}$$

while from Eqs. (7-52) and (7-53) the fresh surface model yields

$$Sh_e = \frac{2}{\sqrt{\pi}}\sqrt{\frac{d_e^2 f}{\mathscr{D}}}(1 + 0.687\varepsilon). \tag{7-55}$$

These results are remarkably close to each other; e.g., for an extreme value of $\varepsilon = 0.5$ the fresh surface prediction is only 6% larger than the surface stretch prediction. The amplitude of the area oscillation, ε, has a relatively small effect since $\varepsilon = 0.3$ in many systems (R3, Y1).

Mass transfer data for oscillating liquid drops have been obtained in several studies in liquids (G2, G8, Y2) and a single study in gases (L5). Comparison with Eqs. (7-54) and (7-55) is difficult due to uncertainty in predicting the frequency f, and the lack of data on the amplitude factor ε. As noted earlier, the frequency of oscillation is generally less than the natural frequency given by Eq. (7-30). The following empirical equation applies to the liquid–liquid data with an average deviation of 6%:

$$Sh_e = 1.2\sqrt{d_e^2 f_N \mathscr{D}} \quad \text{or} \quad \overline{kA}/A_e = 1.2\sqrt{f_N \mathscr{D}}. \tag{7-56}$$

Data for drops in gases show an average deviation of about 30% from Eq. (7-56).
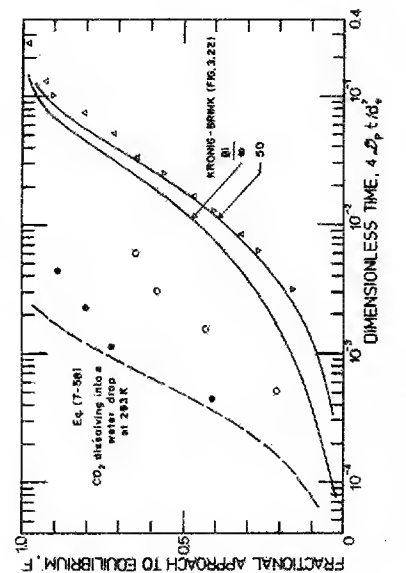
D. INTERNAL RESISTANCE

For circulating fluid particles without shape oscillations the internal resistance varies with time in a way similar to that discussed in Chapter 5 for fluid spheres. The occurrence of oscillation, with associated internal circulation, always has a strong effect on the internal resistance. If the oscillations are sufficiently strong to promote vigorous internal mixing, the resistance within the particle becomes constant.

1. Particles without Shape Oscillations

Although there are no solutions for circulating ellipsoidal fluid particles similar to the Kronig–Brink model for spheres, Fig. 3.22, which includes the external resistance, should be a good approximation with $d = d_e$ and k taken to be the area-free external mass transfer coefficient. This procedure is supported by the work on freely suspended drops in gases by Garner and Lane (G4), who found that the Kronig–Brink model applied up to $Re \doteq 3000$ after decay of strong initial circulation, caused during drop formation. Some of their

data are shown in Fig. 7.16. The ethylene glycol and monoethanolamine drops did not oscillate. The data from these experiments, in which there was a small external resistance, agree well with the curve for Bi = 50 from Fig. 3.22. Similar agreement with the Kronig–Brink model has been found for drops in liquids (B15, K1) as noted in Chapter 5. Although their data for nonoscillating drops in liquids were in fair agreement with the Kronig—Brink model. Skelland and Wellek (S7) proposed an empirical equation which is widely used. In impure systems, where surface-active materials make the particle effectively rigid, the drop may approach equilibrium at rates given by Fig. 3.21.

Fig. 7.16 Fractional approach to equilibrium for circulating and oscillating drops in gases. Data of Garner and Lane (G4).

Symbol	d_e, cm	Drop	Controlling resistance	Re
●	0.58	water	internal	3500
○	0.46	dekalin	internal	3000
△	0.29	glycol	external	1500
▽	0.53	ethanolamine	external	3500

2. Particles with Shape Oscillations

If a fluid particle oscillates violently enough to mix its contents in each oscillation cycle, the average internal resistance is constant if the driving force is based upon the mixed mean concentration within the drop. The fractional approach to equilibrium is then given by Eq. (7-40) or (7-41).

A model of transfer within an oscillating droplet was proposed by Handlos and Baron (H3). They assumed that transfer within the drop was entirely by turbulent motion, random radial movement, superimposed upon toroidal circulation streamlines. No allowance was made for the variation of shape or

surface area. The results of the model are expressed in terms of a series solution for the fractional approach to equilibrium. For long times, only the first term is required, yielding a constant internal resistance:

$$\overline{k}_p = 0.00375 U_T/(1 + \kappa). \qquad (7\text{-}57)$$

Calculations valid for short times and including external resistance are available (P2). Equation (7-57) gives a rough estimate of $(kA)_p/A_e$ for organic-water systems.

The assumption of transfer by a purely turbulent mechanism in the Handlos–Baron model leads to the prediction that the internal resistance is independent of molecular diffusivity. However, such independence has not been found experimentally, even for transfer in well-stirred cells or submerged turbulent jets (D4). In view of this fact and the neglect of shape and area oscillations, models based upon the surface stretch or fresh surface mechanism appear more realistic. For rapid oscillations in systems with Sc $\gg$ 1, mass transfer rates are described by identical equations on either side of the drop surface, so that the mass transfer results embodied in Eqs. (7-54) and (7-55) are valid for the internal resistance if $\mathcal{D}$ is replaced by $\mathcal{D}_p$. Measurements of the internal resistance of oscillating drops show that the surface stretch model predicts the internal resistance with an average error of about 20% (B16, Y1). Agreement of the data for drops in liquids with Eq. (7-56) considerably improves if the constant is increased to 1.4, i.e.,

$$(\overline{kA})_p/A_e = 1.4\sqrt{f_N \mathcal{D}_p}. \qquad (7\text{-}58)$$

Figure 7.16 shows the fractional approach to equilibrium of an oscillating 5.8 mm water drop in a CO_2–air mixture, predicted from Eqs. (7-41) and (7-58). The large decrease in internal resistance with shape oscillation is readily apparent by comparison with the Kronig–Brink lines. The prediction is a good approximation of the rapid approach to equilibrium found by Garner and Lane (G4) for oscillating water droplets with negligible external resistance. Their data for dekalin are intermediate between the oscillating droplet prediction and the Kronig–Brink model, possibly because oscillation was not vigorous enough to mix the contents of the drop fully. Brunson and Wellek (B16) review other models for oscillating drops.

REFERENCES

A1. Ahmadzadeh, J. and Harker, J. H., Trans. Inst. Chem. Eng. 52, 108–111 (1974).
A2. Anderson, R. A., "Fundamentals of Vibrations." Macmillan, New York, 1967.
A3. Angelo, J. B., Lightfoot, E. N. and Howard, D. W., AIChE J. 12, 751–760 (1966).
A4. Aybers, N. M., and Tapucu, A., Wärme-Stoffübertrag. 2, 118–128 (1969).
A5. Aybers, N. M., and Tapucu, A., Wärme-Stoffübertrag. 2, 171–177 (1969).
B1. Bachhuber, C. and Sanford, C., J. Appl. Phys. 45, 2567–2569 (1974).
B2. Baird, M. H. I., and Davidson, J. F., Chem. Eng. Sci. 17, 87–93 (1962).

References

B3. Beard, K. V., J. Atmos. Sci. 33, 851–864 (1976).
B4. Beard, K. V., and Pruppacher, H. R., J. Atmos. Sci. 26, 1066–1072 (1969).
B5. Beek, W. J., and Kramers, H., Chem. Eng. Sci. 17, 909–921 (1962).
B6. Berghmans, J., Chem. Eng. Sci. 28, 2005–2011 (1973).
B7. Berry, E. X., and Pranger, M. R., J. Appl. Meteorol. 13, 108–113 (1974).
B8. Best, A. C., Meteorol. Res. Pap. No. 277 (1946); No. 330 (1947).
B9. Blanchard, D. C., "From Raindrops to Volcanoes." Doubleday, Garden City, New York. 1967.
B10. Bonato, L. M., Termotec. Ric. 20, 11–18 (1971).
B11. Braida, L., M.A.Sc. Thesis, Univ. of Toronto, 1956.
B12. Brian, P. L. T., and Hales, H. B., AIChE J. 15, 419–425 (1969).
B13. Bridgwater, J., and McNab, G. S., Chem. Eng. Sci. 27, 837–840 (1972).
B14. Brignell, A. S., Q. J. Mech. Appl. Math. 26, 99–107 (1973).
B15. Brounshtein, B. I., Zheleznyak, A. S., and Fishbein, G. A., Int. J. Heat Mass Transfer 13, 963–973 (1970).
B16. Brunson, R. J., and Wellek, R. M., Can. J. Chem. Eng. 48, 267–274 (1970).
B17. Bryn, T., David Taylor Model Basin Transl. No. 132 (1949).
B18. Buzzard, J. F., and Nedderman, R. M., Chem. Eng. Sci. 22, 1577–1586 (1967).
C1. Calderbank, P. H., Johnson, D. S. L., and Loudon, J., Chem. Eng. Sci. 25, 235–256 (1970).
C2. Comolet, R., C. R. Acad. Sci., Ser. A 272, 1213–1216 (1971).
D1. Datta, R. L., Napier, D. H., and Newitt, D. M., Trans. Inst. Chem. Eng. 28, 14–26 (1950).
D2. Davenport, W. G., Ph.D. Thesis, Imperial College, London. 1964.
D3. Davenport, W. G., Richardson, F. D., and Bradshaw, A. V., Chem. Eng. Sci. 22, 1221–1235 (1967).
D4. Davies, J. T., "Turbulence Phenomena." Academic Press, New York, 1972.
D5. Davies, R. M., and Taylor, Sir G. I., Proc. Roy. Soc., Ser. A 200, 375–390 (1950).
E1. Edge, R. M., Flatman, A. T., Grant, C. D. and Kalafatoglu, I. E., Symp. Multiphase Flow Syst., Inst. Chem. Eng., London Pap. C3 (1974).
E2. Edge, R. M., and Grant, C. D., Chem. Eng. Sci. 26, 1001–1012 (1971).
E3. Edge, R. M., and Grant, C. D., Chem. Eng. Sci. 27, 1709–1721 (1972).
E4. Elzinga, E. R., and Banchero, J. T., AIChE J. 7, 394–399 (1961).
F1. Finlay, B. A., Ph.D. Thesis, Univ. of Birmingham, 1957.
F2. Foote, G. B., J. Atmos. Sci. 26, 179–181 (1969).
G1. Garbarini, G. R., and Tien, C., Can. J. Chem. Eng. 47, 35–41 (1969).
G2. Garner, F. H., Foord, A., and Tayeban, M., J. Appl. Chem. 9, 315–323 (1959).
G3. Garner, F. H., and Hammerton, D., Trans. Inst. Chem. Eng. 32, 518–524 (1954).
G4. Garner, F. H., and Lane, J. J., Trans. Inst. Chem. Eng. 37, 162–172 (1959).
G5. Garner, F. H., and Lihou, D. A., DECHEMA-Monogr. 55, 155–178 (1965).
G6. Garner, F. H., and Skelland, A. H. P., Chem. Eng. Sci. 4, 149–158 (1955).
G7. Garner, F. H., and Skelland, A. H. P., Ind. Eng. Chem. 48, 51–58 (1956).
G8. Garner, F. H., and Tayeban, M., An. Fis. Quim. LVI-B 479–498 (1960).
G9. Gaudin, A. M., "Flotation," 2nd ed. McGraw-Hill, New York, 1957.
G10. Gibbons, J. H., Houghton, G., and Coull, J., AIChE J. 8, 274–276 (1962).
G11. Gorodetskaya, A., Zh. Fiz. Khim. 23, 71–77 (1949).
G12. Grace, J. R., Wairegi, T., and Nguyen, T. H., Trans. Inst. Chem. Eng. 54, 167–173 (1976).
G13. Gunn, R., and Kinzer, G. D., J. Meteorol. 6, 243–248 (1949).
G14. Guthrie, R. I. L., Ph.D. Thesis, Imperial College, London. 1967.
G15. Guthrie, R. I. L., and Bradshaw, A. V., Chem. Eng. Sci. 28, 191–203 (1973).
H1. Haberman, W. L., and Morton, R. K., David Taylor Model Basin Rep. No. 802 (1953).
H2. Hamielec, A. E., Ph.D. Thesis, Univ. of Toronto, 1961.
H3. Handlos, A. E., and Baron, T., AIChE J. 3, 127–136 (1957).
H4. Harper, J. F., Chem. Eng. Sci. 25, 342–343 (1970).

H5. Harper, J. F., Adv. Appl. Mech. 12, 59–129 (1972).
H6. Hartunian, R. A., and Sears, W. R., J. Fluid Mech. 3, 27–47 (1957).
H7. Hayashi, S., and Matunobu, Y., J. Phys. Soc. Jpn. 22, 905–910 (1967).
H8. Hendrix, C. D., Dave, S. B., and Johnson, H. F., AIChE J. 13, 1072–1077 (1967).
H9. Horton, T. J., Fritsch, T. R., and Kintner, R. C., Can J. Chem. Eng. 43, 143–146 (1965).
H10. Houghton, G., Ritchie, P. D., and Thomson, J. A., Chem. Eng. Sci. 7, 111–112 (1957).
H11. Hozawa, M., Tadaki, T., and Maeda, T., Kagaku Kogaku 34, 315–320 (1970).
H12. Hu, S., and Kintner, R. C., AIChE J. 1, 42–50 (1955).
J1. Johnson, A. I., Besik, F., and Hamielec, A. E., Can. J. Chem. Eng. 47, 559–564 (1969).
J2. Johnson, A. I., and Braida, L., Can. J. Chem. Eng. 35, 165–172 (1957).
J3. Jones, D. M., J. Meteorol. 16, 504–510 (1959).
J4. Jones, D. R. M., Ph.D. Thesis. Cambridge Univ., 1965.
K1. Kadenskaya, N. I., Zheleznyak, A. S. and Brounshtein, B. I., Zh. Prikl. Khim. (Leningrad) 38, 1156–1159 (1965).
K2. Keith, F. W., and Hixson, A. N., Ind. Eng. Chem. 47, 258–267 (1955).
K3. Klee, A. J., and Treybal, R. E., AIChE J. 2, 444–447 (1956).
K4. Kojima, E., Akehata, T., and Shirai, T., J. Chem. Eng. Jpn. 1, 45–50 (1968).
K5. Krishna, P. M., Venkateswarlu, D., and Narasimhamurty, G. S. R., J. Chem. Eng. Data 4, 336–343 (1959).
L1. Lamb, H., "Hydrodynamics," 6th ed. Cambridge Univ. Press. London. 1932.
L2. Lessard, R. R., and Zieminski, S. A., Ind. Eng. Chem. Fundam. 10, 260–269 (1971).
L3. Licht, W., and Narasimhamurty, G. S. R., AIChE J. 1, 366–373 (1955).
L4. Lihou, D. A., Trans. Inst. Chem. Eng. 50, 392–393 (1972).
L5. Lihou, D. A., Lowe, W. D., and Hattangady, K. S., Trans. Inst. Chem. Eng. 50, 217–223 (1972).
L6. Lindt, J. T., Dissertation, Technische Hogeschool, Delft. (Bronder—Offset N. V., Rotterdam, 1971.)
L7. Lindt, J. T., Chem. Eng. Sci. 27, 1775–1781 (1972).
L8. Lindt, J. T., and De Groot, R. G., Chem. Eng. Sci. 29, 957–962 (1974).
L9. List, R., and Hand, M. J., Phys. Fluids 14, 1648–1655 (1971).
L10. Lochiel, A. C., and Calderbank. P. H., Chem. Eng. Sci. 19, 471–484 (1964).
L11. Loutay, R., and Vignes, A., Chem. Eng. Sci. 25, 201–217 (1970).
M1. Magarvey, R. H. and Bishop, R. L., Phys. Fluids 4, 800–805 (1961).
M2. Magarvey, R. H., and Bishop, R. L., Can. J. Phys. 39, 1418–1422 (1961).
M3. Magarvey, R. H., and Blackford, B. L., Can. J. Phys. 40, 1036–1040 (1962).
M4. Magono, C., J. Meteorol. 11, 77–79 (1954).
M5. Marrucci, G., Apuzzo, G., and Astarita, G., AIChE J. 16, 538–541 (1970).
M6. McDonald, J. E., J. Meteorol. 11, 478–494 (1954).
M7. Mendelson, H. D., AIChE J. 13, 250–252 (1967).
M8. Mercier, J., and Anciaes, W., Houille Blanche No. 5, 421–425 (1972).
M9. Mercier, J., and Rocha, A., Chem. Eng. Sci. 24, 1179–1183 (1969).
M10. Miller, C. A., and Scriven, L. E., J. Fluid Mech. 32, 417–435 (1968).
M11. Moore, D. W., J. Fluid Mech. 23, 749–766 (1965).
M12. Moore, F. K., NASA Contract. Rep. NASA CR-1368 (1972).
N1. Napier, D. H., Newitt, D. M. and Datta, R. L., Trans. Inst. Chem. Eng. 28, 14–31 (1950).
N2. Naturajan, R., Combust. Flame 20, 199–209 (1973).
P1. Patel, F. Y., and Acrivos, A., Ind. Eng. Chem., Fundam. 7, 227–232 (1968).
P2. Patel, J. M., and Wellek, R. M., AIChE J. 13, 384–386 (1967).
P3. Peebles, F. N., and Garber, H. J., Chem. Eng. Prog. 49(2), 88–97 (1953).
P4. Pitter, R. L., and Pruppacher, H. R., Q. J. R. Meteorol. Soc. 99, 540–550 (1973).
P5. Pruppacher, H. R., and Beard, K. V., Q. J. R. Meteorol. Soc. 96, 247–256 (1970).

R1. Raymond, D. R., and Zieminski, S. A., *AIChE J.* **17**, 57–65 (1971).
R2. Reinhart, A., *Chem.-Ing.-Tech.* **36**, 740–745 (1964).
R3. Rose, P. M., Ph.D. Thesis, Illinois Inst. of Technol., Chicago, 1965.
R4. Rose, P. M., and Kintner, R. C., *AIChE J.* **12**, 530–534 (1966).
R5. Rosenberg, B., *David Taylor Model Basin Rep.* No. 727 (1950).
R6. Ryan, R. T., *J. Appl. Meteorol.* **15**, 157–165 (1976).
S1. Saffman, P. G., *J. Fluid Mech.* **1**, 249–275 (1956).
S2. Satapathy, R., and Smith, W., *J. Fluid Mech.* **10**, 561–570 (1961).
S3. Savic, P., *Natl. Res. Counc. Can. Rep.* No. MT-22 (1953).
S4. Schroeder, R. R., Ph.D. Thesis, Illinois Inst. of Technol., Chicago, 1964.
S5. Schroeder, R. R., and Kintner, R. C., *AIChE J.* **11**, 5–8 (1965).
S6. Skelland, A. H. P., and Caenepeel, C. L., *AIChE J.* **18**, 1154–1163 (1972).
S7. Skelland, A. H. P., and Wellek, R. M., *AIChE J.* **10**, 491–496 (1964).
S8. Srikrishna, M., and Narasimhamurty, G. S. R., *Indian Chem. Eng.* **13**, 4–11 (1971).
S9. Stuke, B., *Naturwissenschaften* **39**, 325–326 (1952).
S10. Subramanyam, S. V., *J. Fluid Mech.* **37**, 715–725 (1969).
S11. Sumner, B. S., and Moore, F. K., *NASA Contract. Rep.* NASA CR-1669 (1970).
T1. Tadaki, T., and Maeda, S., *Kagaku Kogaku* **25**, 254–264 (1961).
T2. Tapucu, A., Document IGN-87, Ecole Polytechnique, Montreal, 1974.
T3. Taylor, J. D., and Acrivos, A. J., *J. Fluid Mech.* **18**, 466–476 (1964).
T4. Thorsen, G., Stordalen, R. M., and Terjesen, S. G., *Chem. Eng. Sci.* **23**, 413–426 (1968).
T5. Thorsen, G., and Terjesen, S. G., *Chem. Eng. Sci.* **17**, 137–148 (1962).
T6. Tsuge, H., and Hibino, S., *Kagaku Kogaku* **35**, 65–71 (1971).
V1. Vakhrushev, I. A., and Efremov, G. I., *Chem. Technol. Fuels Oils (USSR)* **5,6**, 376–379 (1970).
V2. Van der Leeden, P., Nio, L. D., and Suratman, P. C., *Appl. Sci. Res. Sect. A* **5**, 338–348 (1956).
V3. Vogtländer, J. G., and Meijboom, F. W., *Chem. Eng. Sci.* **29**, 799–803 (1974).
W1. Wairegi, T., Ph.D. Thesis, McGill Univ., Montreal, 1974.
W2. Wallis, G. B., *Int. J. Multiphase Flow* **1**, 491–511 (1974).
W3. Warshay, M., Bogusz, E., Johnson, M., and Kintner, R. C., *Can. J. Chem. Eng.* **37**, 29–36 (1959).
W4. Weiner, A., Ph.D. Thesis, Univ. of Pennsylvania, Philadelphia, 1974.
W5. Wellek, R. M., Andoe, W. V., and Brunson, R. J., *Can. J. Chem. Eng.* **48**, 645–655 (1970).
W6. Wellek, R. M., Agrawal, A. K., and Skelland, A. H. P., *AIChE J.* **12**, 854–862 (1966).
W7. Weller, K. R., *Can. J. Chem. Eng.* **50**, 49–58 (1972).
W8. Winnikow, S., and Chao, B. T., *Phys. Fluids* **9**, 50–61 (1966).
Y1. Yamaguchi, M., Fujimoto, T., and Katayama, T., *J. Chem. Eng. Jpn.* **8**, 361–366 (1975).
Y2. Yamaguchi, M., Watanabe, S., and Katayama, T., *J. Chem. Eng. Jpn.* **8**, 415–417 (1975).
Y3. Yao, S.-C., and Schrock, V. E., *J. Heat Transfer* **98**, 120–125 (1976).
Y4. Yeheskel, J., and Kehat, E., *Chem. Eng. Sci.* **26**, 1223–1233 (1971).
Z1. Zabel, T., Hanson, C., and Ingham, J., *Trans. Inst. Chem. Eng.* **51**, 162–164 (1973).
Z2. Zieminski, S. A., and Raymond, D. R., *Chem. Eng. Sci.* **23**, 17–28 (1968).

Chapter 8

Deformed Fluid Particles of Large Size

I. INTRODUCTION

This chapter is devoted to bubbles and drops with $Eo > 40$ and $Re > 1.2$ (see Chapter 2). These inequalities are generally satisfied by bubbles and drops with volumes greater than about 3 cm^3 (i.e., $d_e > 1.8 \text{ cm}$). Considerable work has been carried out for large gas bubbles, primarily in connection with underwater explosions, fluidized beds, and processing of liquid metals, and reviews have been prepared by Wegener and Parlange (W5) and Harper (H2). Relatively little attention has been devoted to large drops. Drops falling in gases almost always break up before an Eotvos number of 40 is reached (see Chapter 12) so that the present chapter is restricted to cases where the continuous phase is a liquid.

In the present chapter, we neglect wall effects and unsteady motion including splitting. These factors are considered in Chapters 9, 11, and 12, respectively. The fluid mechanics of large bubbles and drops are discussed before turning to mass transfer.

II. FLUID MECHANICS

A. SHAPE

Over most of the range covered by this chapter, the shape of bubbles and drops can be closely approximated as a segment of a sphere (see Fig. 2.4). Hence, most of the fluid particles under discussion are said to be "spherical-caps." For $Re \gtrsim 150$, the rear or base is quite flat, though sometimes irregular, and the wake angle very nearly $50°$. At lower Re, the wake angle is larger (G4), as shown in Fig. 8.1. For $Re < 40$, the leading edge tends to be oblate ellipsoidal